UNIVERSITÀ DEGLI STUDI DI PADOVA
Dipartimento di Scienze chimiche
Dipartimento di Fisica e Astronomia "Galileo Galilei"
Master degree in Materials Science

Final Dissertation

Investigation of Germanium Hyperdoping by Pulsed Laser Melting

Thesis supervisor: *Prof. Enrico Napolitani*
Co-supervisors: *Dr. Enrico Di Russo*
Dr. Giulia Maria Spataro
Counter supervisor: *Prof. Giulio Monaco*

Candidate
Moreno Patanè

Academic Year 2023/2024

Table of contents

Chapter 1

Introduction

In recent years the interest of both scientific community and industry in germanium (Ge) has seen a spike, after decades of neglect. As the industry of nanoelectronics develops, the necessity to improve the performance of electronic devices is pushing the limits of silicon-based technology. Germanium, with its better electric properties, mainly a higher carrier mobility and low resistivity, is already being integrated in modern devices thanks to its good compatibility with silicon (Si) production processes. But the advantages of germanium are not limited to electronics applications. Germanium exhibits specific optical properties that make it a prime candidate for the use in optical devices, such as material for infrared (IR) lenses thanks to its transparency in this spectral range, and in fibre optics thanks to the oxide's high reflective index. Germanium is also being studied for more advanced applications in IR photonics and laser production, as well as quantum computing.

Most of these advanced applications require a high doping of germanium in order to tune its electrical and optical properties. However, most of the major dopants in germanium show a low solid solubility limit and even lower active concentrations at thermal equilibrium, that is even more true for n-type dopants. To overcome these issues, the–UV nanosecond laser processing stands out as a valid methodology for the achievement of highly doped germanium. The nanosecond laser annealing process is characterized by a fast melting and re-crystallization of the materials' surface layer. Considering that the entire process occurs in a timescale of hundreds of nanoseconds this technique is able to induce a strong out-of-equilibrium incorporation of dopants atoms inside the lattice matrix, as the atoms are kinetically hindered from reaching their thermal equilibrium distribution. The objective of the thesis is to obtain phosphorous-doped Germanium layers with an active dopant concentration higher than the solid solubility limit at thermal equilibrium, this condition is defined as hyperdoping.

Different samples consisting on "in-situ" phosphorous doped epilayers of Ge (Ge:P) and $Si_{15}Ge_{85}$ alloy (SiGe:P) grown on Si substrates have been considered. They have P active concentrations around or below $2x10^{19}cm^{-3}$, i.e. below the equilibrium maximum active P concentration reported in literature ($6x10^{19}cm^{-3}$), and well below the chemical P concentrations present in the samples, that are in the range 1-4x10^{20}cm^{-3}. In order to improve the P electrical activation, the samples were processed by Pulsed Laser Melting (PLM) and have been characterized to evaluate the effect of the laser processing on their morphological, structural and electrical properties. The samples have been obtained by performing the laser anneal process on 4 wafers provided by the collaboration with the L-NESS research group in Como (Physics Department of Politecnico di Milano), where the doped layers are grown on silicon wafers by Low Energy Plasma Enhanced Chemical Vapour Deposition (LEPECVD). Among the four wafers, three are made up of Ge:P layers grown on silicon, each characterized by different properties. The samples differ in chemical dopant concentration, grown layer thickness and surface quality.

The aim of the work is to produce stable, hyperdoped Ge:P and SiGe:P layers as a base for the subsequent growth of Ge or Si:Ge multiwell quantum structures for the production of IR photonic devices, where the hyperdoped layers behave as IR reflectors.

The samples have been processed thanks to a 248 nm wavelength laser with 22 ns pulses at varying energy densities, from 0.3 to 0.9 J/cm^2. The quality of the samples' surface after the laser process has been evaluated thanks to Atomic Force Microscopy (AFM), that showed a good surface quality after liquid phase epitaxial regrowth induced by PLM. This shows an interesting property of the PLM process, namely the possibility of preserving the surface features on the processed sample, as observed by the presence of the same surface ripples before and after the laser process.

Micro-Raman measurements have been utilized to assess the strain properties of the samples before and after the laser process. While the samples before the process are almost relaxed thanks to the equilibrium conditions of the CVD growth, some of the processed samples have shown a certain level of tensile strain produced by the thermal gradient and related thermal expansion induced by the PLM process.

SIMS experiments were performed to study the chemical composition of the samples and the dopant's depth distribution profile. The phosphorous concentration profile in the processed samples has been observed to be flat for the exception of a pile-up at the interface between the maximum melted and un-melted region (maximum melt depth – MMD), a common characteristic of PLM.

In order to evaluate the effects of the laser process on the effective electrical activation of the samples, Van der Pauw-Hall (VDP-H) measurements have been performed. Thanks to this characterization the active dopant concentration, the carrier mobility and the resistivity of the processed layers have been obtained by mean of a bi-layer model that allowed us to separate the electrical contribution of the layers processed by PLM and the underlying layer, unaffected by the laser process.

All the samples have shown an improvement of the electrical activation after PLM, up to a maximum activation of 74% for the highest doped wafer. The energy density for the laser process doesn't seem to affect the activation level, as a correlation between the two properties has not been observed.
Finally, keeping in mind the final application of the samples, a thermal stability study has been conducted on the samples to assess their suitability for the subsequent growth processes they could be subjected to, which happens in a temperature range between 250 and 500 °C. The thermal tests have been performed by applying isochronal Rapid Thermal Annealing (RTA) processes on the samples with 25 °C temperature increments. A good stability has been observed for the samples up to 300 °C, with a major difference for the highest doped sample, whose deactivation starts at 150 °C. This occurrence seems to be well described by a phenomenological model that accounts for the clustering phenomenon of dopants, that describes the kinetics of the process as being directly dependant on dopant concentration and exhibiting a decreasing activation energy with respect to the active dopant fraction.

While SIMS measurements can give access to the chemical depth profile of the dopant, we have no detailed information on the active dopant concentration as a function of the depth, as the VdP-Hall technique has no direct depth sensitivity.
A reliable electric measurement able to extract an active dopant profile from a sample is difficult to obtain. Differential Van Der Pauw-Hall measurements are usually time consuming, and a reliable calculation of the etching rate is necessary to identify the correct investigated depth for every etching step. Speeding Profile Resistance (SPR) can be an alternative, but the measurements rely on the assumption of a resistivity vs concentration curve.
During the thesis period an initial study to set-up another electrical characterization technique has been conducted. Scanning Microwave Microscopy (SMM) is an electrical probe technique that can be used to extract qualitative and quantitative electrical information from both conducting and non-conductive materials, thanks to the interaction between microwaves and matter. The technique is still immature, as an easy and reliable calibration procedure has yet to be identified. The first experiments have been performed on a doped silicon standard and a calibration curve has been obtained, after that a bevelled germanium sample has been investigated, and an interpretation of the results is provided. An investigation on a bevelled sample was also conducted to evaluate the feasibility of the bevelling procedure, coupled with SMM measurements, to extract an active dopant profile with respect to the sample's depth. The SMM measurement results are placed in the final appendix, as this study is still in the explorative stage.

Chapter 2

Germanium background and properties

2.1 History of germanium and its applications

The existence of Germanium was first hypothesized by I.D Mendeleev in 1871 and discovered by Clemens Alexander Winkler in 1886. In 1942 Karl Lark-Horovitz, head of Physics Department at Purdue University decided to investigate Germanium for its use in high frequency rectifiers for radar receivers. In just five years the first transistor, based on Germanium, was made by Bell laboratories' scientists, J. Bardeen and W.H. Brattain, thanks to a polycrystalline Germanium slab provided by Purdue University[1]. This scientific milestone opened the way to the semiconductors electronics as we know it today.

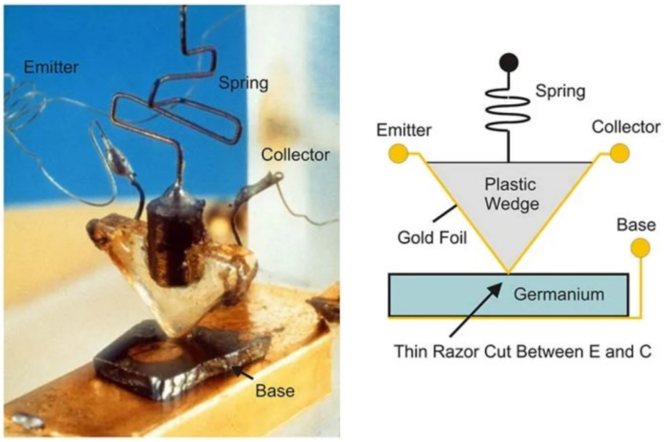

Figure 2.1: First Germanium transistor developed by Bell Laboratories introduced December 23, 1947.

But Germanium was quickly discarded in favour of silicon; in less than 10 years Bell labs created the first prototype of a Si based transistor (1954). The choice was justified by the specific necessities of micro- and nano-electronics, where the better heath resistance of silicon and its lower free electron density at room temperature made it an obvious choice over germanium, along with the better gate oxide stability. But as the nanoelectronics field reaches higher level of performance and sophistication the limits of silicon are being underlined, and the addition of germanium to modern transistor is able to improve the performance of such devices thanks to its higher mobility and ease of integration into silicon processes[2]. Moreover, the concurrent development of high-k materials will be an enabling factor for Ge integration, by solving one of its major downsides, that is the poor quality of its native oxide.

While germanium has been neglected by the electronics industry, it still finds its uses in several fields thanks to its optical properties related to its bandgap modulation through doping and strain, and its high refractive index exploited in optic fibres.

As shown by many surveys, there is no shortage of applications for Ge at the industrial level. The main uses of germanium for modern technology include fibre optics, IR optics, solar applications and Polyethylene terephthalate (PET) catalysis [3]. A zoom on Europe's end uses shows the prevalence of the first three applications, while germanium as catalyst for PET synthesis is mainly used in Japan and electronics applications are mainly developed in USA and Asia[4].

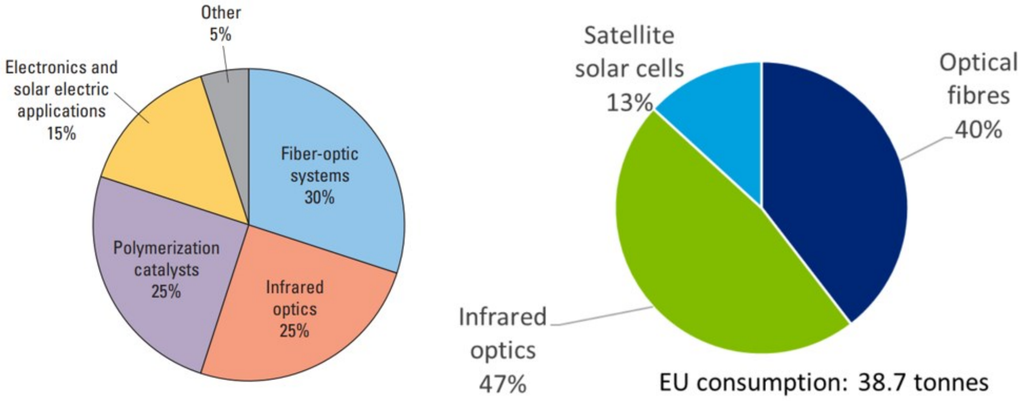

Figure 2.2: Global Germanium ned uses in 2012, left [3]. EU Germanium end uses in 2016, right [4].

Novel applications for germanium are being proposed in recent years, most of them requiring high levels of doping.

For instance, the use of heavily doped Ge is a promising alternative to noble metals (more costly and difficult to integrate in silicon foundries) for the mid-IR sensing of the fingerprint region for molecules recognition, thanks to its plasmonic behaviour at this spectral range in comparison to the that of noble metals. Indeed, the use of noble metals for mid-IR sensing requires the production of metallic nanoparticles-based devices, while Ge-based devices could be produced by simpler means thanks to its compatibility with Si production processes, and with simpler geometries [5]. While metal nanostructures, mostly based on gold and silver, have a good plasmonic response thanks to surface plasmon resonance in the visible range, to push their resonance into the near-IR and mid-IR range the size and shape of the nanostructures has to be carefully controlled. Moreover, metals are characterized by high free electron density that lowers the sensitivity in the mid-IR region by electric losses. On the other hand, by controlling their doping level of semiconductor materials, the free carrier density can be tuned, which in turn affects wavelength of the plasmonic resonance.

Another application for heavily doped Ge aims to combine the effects related to n-type doping and tensile strain to produce a Ge diode laser that can be monolithically integrated on CMOS devices, enabling the production of Photonics-Integrated Circuits (PIC). An electrically pumped laser device has been proposed, where an active concentration of $4x10^{19}$ cm^{-3} of phosphorus dopants can achieve a sufficient gain to overcome the electrical losses produced by the combination of contact losses and free carrier recombination inside the poly-silicon layer[6]. Following studies have also proposed the feasibility of n-doped Ge waveguides to produce optically pumped Si monolithic lasers. In this case the maximum doping level obtained was $2x10^{19}$ cm^{-3} with a 0.1% tensile strain[7].

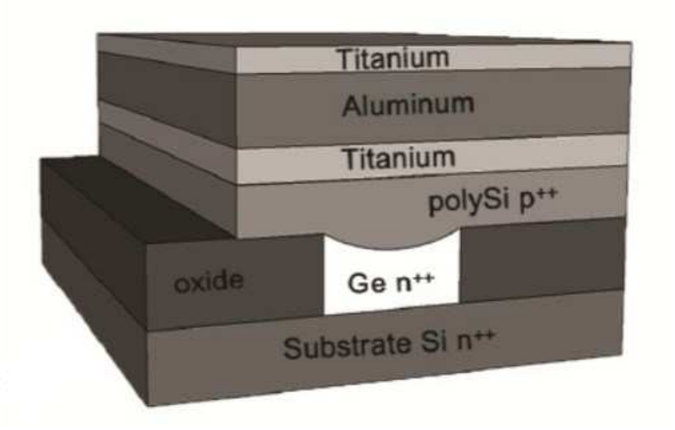

Figure 2.3: Representation of a prototype of an electrically pumped Germanium laser produced for testing at MIT [6].

Obtaining highly n-doped, thermally stable germanium layers is not an easy task, as it will be discussed in more detail in the next chapter: the activation of such material is still one of the biggest challenges for the integration of Ge on mass scale production of advanced optical and electronic devices.

2.2 Germanium doping, diffusion and carrier activation

The following sections will cover some of the specific characteristics of germanium in terms of doping to better frame the issues that need to be overcome for the development of Ge-based devices.

2.2.1 Doping

The process of doping a semiconductor refers to the application of various techniques to introduce specific impurity dopant atoms into the lattice of a semiconducting material. It wouldn't be an overstatement to say that the ability to introduce impurities into silicon and other semiconductors in a controlled manner is what allowed this family of elements to move from the "physics of dirt" to becoming one of the most history defining materials of the human venture. Most of the semiconductor's properties that are leveraged for technical purposes, are specifically given by the doping of said materials, form their electric properties to the optical behaviour.

The process of silicon doping and its effect on the material are widely characterized considering that silicon has been at the base of most electronic devices since 1960. But now that silicon technologies are reaching a plateau, it's necessary to evaluate other materials and processes. Going back to germanium it's easy to understand why the doping processes and the theory behind it stems from the experience gained form silicon research.

Different doping methodologies offer different advantages and disadvantages, and the specific doping technique is selected case by case depending on the necessities.

Currently, the leading doping method for electronics is the ion implantation. The latter offers the advantage of a well-defined spatial control in both depth profile and shape of the activated region (of fundamental importance in Integrated Circuit, IC, industry). Generally, the ion implantation process is followed by an annealing step aimed at the reduction of implantation damage and further activation of the implanted dopants, alternatively the implantation process is carried out at a specific temperature; both hot and cold implantation techniques have been proposed[8][9]. Even though the physical phenomena occurring on the microscopic scale are difficult to characterize and foresee, ion implantation stands as one of the most reproducible doping methods currently applied in IC industry. This is thanks to the tremendous effort that both scientific and industrial research have put into characterizing this doping method, pushed by the ever-growing electronics and optics market demand, and today several software are available for the simulation of ion implantation process (a collection of ion beam simulation software can be found at "https://www.ionbeamcenters.eu/resources/ion-beam-software/").

But as the shrinkage of nano-electronics devices proceeds, and new geometries are proposed to overcome the intrinsic limitation of planar CMOS devices (mainly the high tunnelling leakage currents through the insulator gate layer), the classic ion implantation technique would not be able to follow the new geometries required for the production of FinFETs and the future Gate-All-Around Transistors. New proposals are currently examined in order to bring the ion implantation technology into the “Angstrom age” of semiconductors. The implantation at an angle can help control the lateral and depth doping in comparison to normal incidence ion implantation, for instance for the implantation of thin finFETs regions[10]. Even considering some novel approaches to the ion beam doping we also have to take into account the limits imposed by the material under study, more specifically it has been proved that germanium suffers from an enhanced defectivity induced by ion implantation in comparison to silicon that is not recovered even after post anneal [11], [12]. The flexibility of ion implantation is limited, and new doping techniques must be integrated into production lines.

Another approach to obtain doped semiconductors is the so called “in-situ” doping. As the name suggest the characteristic of this methodology is the possibility of obtaining a doped layer of semiconductor while the layer itself is being grown on a suitable substrate. The in-situ doping techniques are widely used for the fabrication of doped wafers that find applications both as starting substrates for industrial applications and specifically grown for scientific research.

Among the in-situ techniques we find several growth methods, the most used are Chemical Vapour Deposition (CVD) and its variants, Molecular Beam Epitaxy (MBE), and Physical Vapour Deposition (PVD). These techniques offer the opportunity to control the thickness of the deposited layers and their doping, to a varying degree, by tuning the process parameters like precursors flow/concentration and temperature. It is also possible to introduce a specific strain effect, by growing layers of semiconductors with different lattice parameters. The ability to engineer the strain of a semiconductor during growth allows for the tuning of the bandgap and to achieve the absorption or emission characteristics required by optoelectronic devices[13], [14]. Other advantaged of in situ doping techniques are the possibility of directly obtaining layers of alloys, like the widely used SiGe, and the ability to obtain good crystallographic homogeneity. By growing subsequent layers it’s possible to obtain layered structures and buried layers with a control that is not achieved by classic ion implantation methodologies with post anneal. While CVD and MBE offer good control on the layer’s thickness and crystallinity, they are generally slow and less suited for industrial integration. Moreover, while in-situ doping techniques are able to produce layers with a high chemical concentration of dopants (total incorporated impurities, both substitutional and in other bound forms), they usually exhibit a lower concentration of active dopant (substitutional impurity atoms that contribute to electrical and optical properties) and some form of anneal may still be necessary.

There is no doping technique without downsides and for modern devices manufacturing a mixture of ion implantation, in situ doping, and lithographic steps are involved to produce transistors and optical devices like LEDs, IR sensors and laser sources where different layers are produced with the best suited technique for the desired property.

ion implantation produces large defects into the material that must be recovered by thermal annealing, and in situ growth usually involves some form of heating of the substrate. The thermal anneal step is not something that should be taken lightly. Indeed, as devices become more complex and multi-layered, incorporating several active regions with specific uses and properties, the thermal budget that can be allocated for a single process has to be carefully accounted for. During device fabrications, several steps of lithography, growth and annealing are alternated to make the finished product. A thermal anneal step or a growth process may be required at a specific point in the production of the device, but the thermal energy introduced for the process may damage some already produced layer. From this observation come the necessity to identify a way to produce stable doped layers where the thermal budget can be carefully delivered selectively onto the surface layer.

Regardless of the doping techniques utilized, it’s important to understand how the impurities incorporation happens and the specific issues of n-type dopants in germanium.

In order to evaluate the effective incorporation of the impurities into the Germanium crystal matrix and understand why different dopants behave in different ways inside the matrix, we need to identify a parameter to describe the incorporation of said impurities. This parameter is the *solid solubility limit*. For a given impurity, the dopant solid solubility limit is defined as the maximum concentration of the impurity atom in the solid matrix at thermal equilibrium with the matrix liquid phase. The parameter that describes the equilibrium between the solid phase and the liquid phase is the segregation coefficient k:

$$\mathrm{k} = \frac{C_S}{C_L} \qquad 2.1$$

with C_s and C_L being the impurity concentrations in the solid and in the liquid phase of the matrix. The segregation coefficient is a function of the temperature and it’s less than 1 for most of the common dopants (except for boron, B, that exhibits a $k > 1$), indicating that most of the dopants are more soluble in the liquid phase than in the solid matrix. This last observation is the leading motivation that has brought the scientific community to purse activation methodologies by melting the solid matrix and incorporating the impurities thanks to a fast recrystallization, effectively hindering the deactivation that would occur through reorganization of the matrix at thermal equilibrium. The following figure gives an overview of the solid solubilities, and the maximum activations reached by applying various annealing methods for the common dopants in germanium.

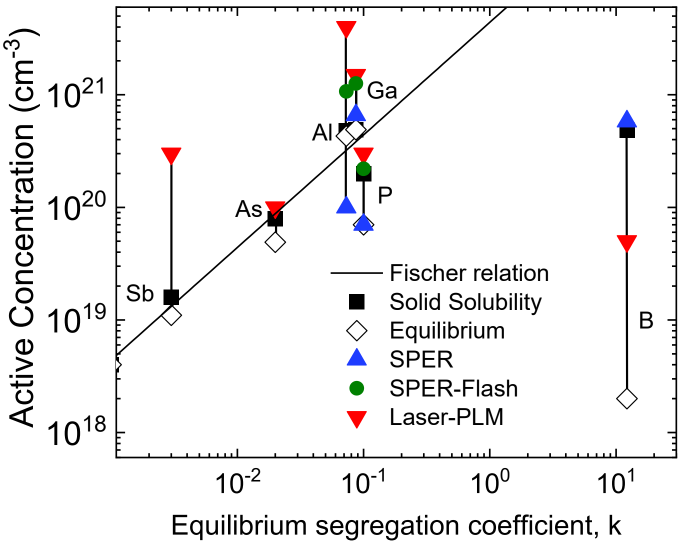

Figure 2.4: Maximum active concentration vs equilibrium distribution coefficient, compared with maximum equilibrium solid solubilities (solid squares), for Group III and V (squared labels) impurities in Ge, obtained with different processing methods: equilibrium processes (diamonds), solid-phase epitaxy regrowth (SPER) (up triangles), SPER followed by flash lamp annealing (circles) and pulsed laser melting (down triangles). Fischler curve is also reported for comparison [15]. All the equilibrium data from the reviews by Olesinski et al.[16], [17], [18] and Trumborec [19]. SPER data are from Impellizzeri et al.[20], [21], [22] and Posselt et al.[23], Flash lamp annealing data are from Prucnal et al.[24], [25], PLM data from Impellizzeri et al.[26], Mazzocchi et al.[27], Milazzo et al.[28], [29], Carraro et al[30]. Re-adapted from [31]

Figure 2.4 underlines one of the major issues that germanium poses to its application in devices integration.

P-type dopants (Ga, Al) have high solid solubility limits and their activation at thermal equilibrium is high, even without the use of out of equilibrium techniques. Boron is an exception because, while its solid solubility limit is quite high, its activation at thermal equilibrium is low; this occurrence is explained by the interaction of boron with interstitial vacancies and subsequent deactivation by clustering. The laser annealing for boron is not the best activation method as it produces an oxygen-boron (O-B) interaction in the molten phase that hinders the full boron activation during the rapid recrystallization. O-B complexes are formed at the surface of the sample by in-diffusion of oxygen, while at the interface between the molten region and the un-melted one B-B complexes further deactivate the material[32]. Aluminium is also affected by oxygen interaction as indicated by Milazzo et al.[29].

N-type dopants exhibit lower solid solubility limits in germanium in comparison to the p-type ones and, even more problematic, their activation at thermal equilibrium is systematically lower than the chemical concentration. Indeed, a full activation for n-type dopants in germanium is very difficult to achieve under equilibrium conditions and this is the main reason why the research on n-doping of Germanium has been steadily gaining momentum in recent years. The use of n-type Ge would prove useful in the IC industry thanks to the high electron mobility of germanium in comparison to silicon, that could improve the performance of high frequency switching devices, as the maximum working frequency of a logic gate is directly dependent on carrier mobility. To understand the reason why n-type dopants are less activated than p-type ones and have a general understanding of the processes that lead to the activation and deactivation of an impurity atom, we need to introduce the diffusion properties of dopant atoms.

2.2.2 Diffusion of impurities in germanium and deactivation issues

With the term diffusion we broadly describe all those phenomena that lead to the homogenization of a gradient inside a system, we can have diffusion of energies (like thermal or electric energy) or physical entities like atoms, ions and other particles. In this section we will focus on solid state atomic diffusion, namely the phenomenon that allows for the reorganization of the impurity atoms inside the solid matrix of semiconductor material.

The diffusion phenomenon is mathematically described by Fick's First Law:

$$J(x) = -D(x)\frac{\partial C(x)}{\partial x} \qquad 2.2$$

which states that the flux of impurity atoms has a dependence on the local gradient of concentration ($\frac{\partial C(x)}{\partial x}$) and the diffusivity, also called diffusion coefficient, D. The minus sign in the formula describes the physical observation that the flux of matter naturally happens in opposition to the gradient, from a region at higher concentration to a region of lower concentration. The formula here reported is the mono-dimensional description of the diffusion process; the full 3-dimensional description is obtained by substituting the scalar diffusion coefficient to its tensor notation and the partial derivative of the concentration to the gradient in the three directions. For materials with a high symmetry like germanium and other crystals with a diamond structure, the diffusion coefficient can be simplified into a scalar and we can use the formula 2.2.

Fick's first law describes the magnitude of the flux of matter depending on the difference in concentration between two regions, but is not able to describe how a concentration profile changes over time. Indeed, Fick's first law is commonly called steady-state law and is useful to describe systems in which the concentration generating the gradient doesn't change over time (infinite source), this description of the system is not representative of a real case scenario. In semiconductors physics we usually study the evolution of the dopant concentration over time at a process temperature. As the process of diffusion goes on in each region of space, the concentrations will change according to the difference in concentration with the surrounding regions.

We need to introduce the time dependence for the local concentrations with Fick's second law:

$$\frac{\partial C(x,t)}{\partial t} = D(x)\frac{\partial^2 C(x,t)}{\partial x^2} \quad 2.3$$

where the diffusivity is considered independent on time.

It’s important to underline that, being a thermically activated process, diffusion has a dependence on temperature, even if the temperature parameter is not explicitly shown on the general Fick’s laws. The temperature dependence of the flux of matter is accounted for in the diffusion coefficient, that has an Arrhenius law dependence on T:

$$D = D_0 \exp\left(-\frac{E_a}{k_b T}\right) \quad 2.4$$

with D_0 and E_a being respectively the maximum diffusion coefficient (at infinite temperature) and the activation energy. This simple formula contains some important information: first the dependence on D_0, which is a parameter that is specific for each impurity in a certain matrix and can vary depending on size, electronegativity and the type of interaction that is promoting the diffusion, and second the activation energy E_a, that can be considered the activation energy necessary to promote a specific “jump” from a state to another one.

It is now necessary to define how an atom can move inside a solid matrix in order to diffuse. Generally, in a crystal matrix both impurities and host atoms can diffuse by jumping form a position to another. Not all processes are the same and some might require higher energies to occur in comparison to others.

We can identify several diffusion mechanisms that affect both impurities and the host atoms (self-diffusion). The simplest mechanism that we can imagine for the diffusion of an atom inside a crystal matrix is a “jump” from a lattice position to another by exchanging its place with different atom, or by simply moving through the lattice. If an atom finds itself in an interstitial position the most probable mechanism is the *direct interstitial diffusion mechanism*, where the atom can simply move through the lattice and end up in a different interstitial site. This process has a low activation energy, since no bond is being broken and it’s the preferred diffusion process for small atoms, like hydrogen and lithium. As the radius of the atom increases, this diffusion mechanism gets hindered by the resistance of the lattice to be stretched, so the interstitial atom needs to find another mechanism to diffuse. A substitutional atom has also access to a direct diffusion pathway, the *direct substitutional mechanism*, that occurs by an exchange in positions between two bonded atoms. This process is thermodynamically expansive because it requires the net breakage of 6 bonds (considering Ge and Si crystal structures); while theoretically possible it rarely occurs considering the high activation energy. A ring diffusion mechanism is also theorized, but has little experimental support and it’s weight on the total diffusion of species is still debated.

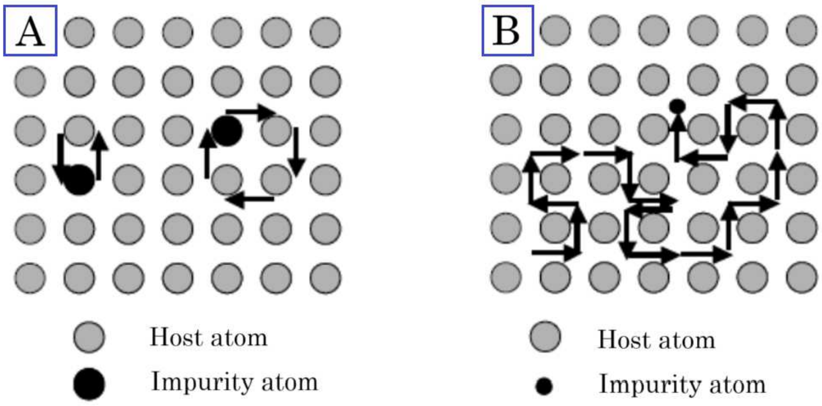

Figure 2.5: Direct diffusion mechanism for substitutional atoms (A), and interstitial atoms (B).

The main diffusion mechanism for dopants in Germanium are part of another category of phenomena. The defect-mediated mechanisms. The mechanisms so far described only take into account the diffusion of atoms inside a perfectly ordered crystal, where an atom can only move by interacting with host atoms in their substitutional site or by moving in between these sites. But in a real case scenario the lattice exhibits many defects, like an interstitial host atom (self-interstitial), or a vacancy (lack of atom in a lattice site) or even more complex defects like clusters. This kind of defects are called point-defects and the interaction of impurity atoms with this kind of defects account for the majority of the diffusion phenomena that happen inside the lattice. The model used to describe them is called *pair-diffusion mechanism* and it aims to describe the diffusion as a chemical reaction between two species, the diffusing atom and another species that usually promotes the diffusion functioning as a vehicle[33].

A dopant substitutional atom can interact with both vacancies and interstitial defects as described by the following equations to form atom-defect mobile pairs:

$$V + A_S \rightleftharpoons VA \qquad 2.5$$

$$I + A_S \rightleftharpoons IA \qquad 2.6$$

with A_S substitutional atom, V and I respectively a vacancy and interstitial defect. At thermal equilibrium germanium exhibits a much higher concentration of vacancies in comparison to interstitial defects, this has been known for a long time[34]. Recent calculations offer better data in terms of formation energies. Formation enthalpies are estimated to be 2.35 ± 0.1 eV for vacancies and 3.13 ± 0.12 eV for self-interstitial[35], [36]. This characteristic of germanium has an important effect on the diffusion properties of the dopants inside the matrix and also on their activation at thermal equilibrium. Indeed, most of the usual dopants diffuse by vacancy-mediated mechanism and their diffusion coefficient is quite high.

As figure 2.6 summarises, n-type dopants in Ge exhibit the highest diffusivities, while p-type ones closely follow the self-diffusion of germanium (also vacancy mediated[34]). Boron is an exception. As already anticipated in chapter 2.2.1, boron has a strong interaction with interstitial defects, and their population is quite low in equilibrium conditions. The effects on diffusivity can be interpreted by the fact that the diffusion coefficient has a dependence on the "effective rate" of successful interactions between the atom and the vehicle species that promotes the atom's diffusion. Being the population of interstitial defects low, the rate is also low, and the diffusivity decreases.

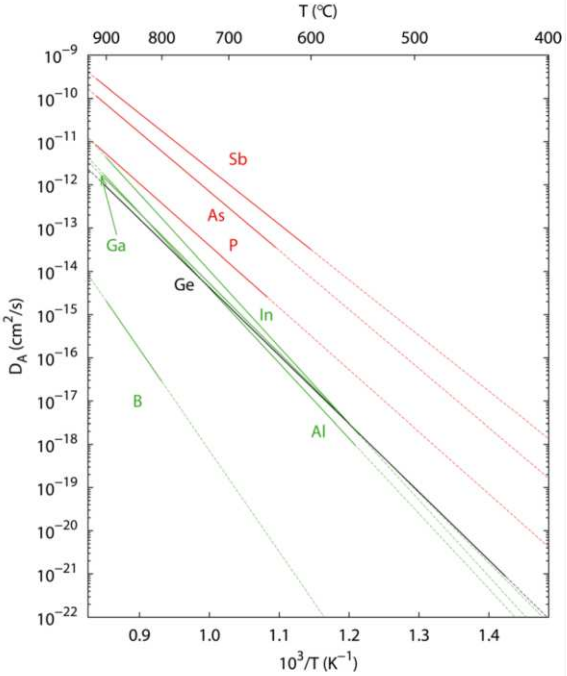

Figure 2.6: Equilibrium diffusion coefficients of the n-(red lines) and p-type dopants (green lines) in Ge compared the self-diffusion (black line) as function of temperature. Dashed lines correspond to extrapolations to higher and lower temperatures[37]

Even among the other dopants, that diffuse by vacancy mediated mechanisms we observe different behaviour between donors and acceptors. This difference can be explained by the charge state of vacancies and impurity atoms inside the lattice. Indeed, point defects, both interstitial and vacancies can assume charge states different than the simple neutral one. When introducing the pair-defect mechanism, the possible charge states of the point-defects has been ignored for clarity's sake. Now we can introduce the dependence of the diffusion on the charge state of the defects.

The charge state of defects depends on the fermi level of germanium, which is affected by the presence of the dopant atoms. It has been shown that Ge self-diffusion is dependent on the doping level[38]. Since self-diffusion in Ge is vacancy-mediated, this suggests that vacancies are affected by doping of the material itself. It has been proposed that vacancies have two energy levels inside germanium's bandgap that can be occupied by electrons depending on the doping level. Indeed, under n-type doping vacancies are doubly negatively charged (V^{2-}), while under p-type one the most stable vacancy is the neutral one (V^{0}). We can now rewrite the pair-diffusion equations to account for the two doping cases.

For n-type doping equation 2.5 becomes:

$$V^{2-} + A_S^{+} \rightleftharpoons AV^{-} \tag{2.7}$$

And for the case p-type doping:

$$V^{0} + A_S^{-} \rightleftharpoons AV^{-} \tag{2.8}$$

Its intuitive to understand that a donor atom, positively ionized, has a better interaction with the negative vacancy when compared to the interaction of a negatively ionized acceptor with a neutral vacancy. The mobile pair produced under n-doping conditions is bound by the electrostatic attraction between the two charged species, this lowers the activation energy for the reaction and grants a higher stability of the mobile pair that can effectively diffuse through the matrix. On the opposite side, under p-type doping we see a majority of neutral vacancies at equilibrium, and no Coulombian interaction occurs with the negative donor atom, while the interaction with the minority of negatively charged vacancies is a repulsive one.

The dependence of the donor's diffusivity with doping level can be formalized mathematically by the following equation proposed by Brotzmann and Bracht[38]:

$$D(n) = D(n_i)\left(\frac{n}{n_i}\right)^2 \tag{2.9}$$

This formula states that the diffusivity has a square dependence on the free carrier concentration, with n_i being the intrinsic carrier concentration of germanium and $D(n_i)$ the diffusivity under intrinsic condition.

At high n-type doping conditions, the vacancy mechanism so far described is unable to properly explain experimental doping profiles. More specifically we see a notable difference between the chemical doping profile and the active concentration profiles. This evidence can be explained by a deactivation mechanism driven by the neutralization of the charged donor-vacancy pairs by formation of higher order complexes[39].

Indeed, the charged pair produced by the reaction 2.7, can still interact with other ionized donors by electrostatic interaction, and create inactive clusters as follows:

$$VA^{-} + A_S^{+} \rightleftharpoons VA^{0} \tag{2.10}$$

These clusters, in contrast to the mobile pair, are immobile and effectively decrease the diffusion of donors at high concentrations and lower the maximum active concentration obtainable at thermal equilibrium.

The clustering is today considered the main mechanism that leads to the deactivation of donors at high concentrations in germanium, and several methods are being proposed for the inhibition of this process.

Many co-doping methodologies have been proposed in order to inhibit the interaction of donors with the vacancies. Strategies involving isovalent atoms or double donor doping have been considered. Co-doping with carbon has been proposed, but it has been demonstrated that this methodology is not a viable method to inhibit the deactivation. While the formation of Atom-Vacancy-Carbon clusters (AVC) delays the diffusion, thanks to the higher activation energies for the diffusion of this species, it doesn't solve the deactivation issue as a considerable portion of donors are trapped and deactivated by the clusters[39], [40].

Alloying with tin has been recently proposed. GeSn epitaxial samples have been grown with different phosphorus doping concentrations up to $10^{20} cm^{-3}$. Experimental findings have been supported by theoretical calculations, showing that Sn-V and Sn-P-V clusters are less stable than the equivalent clusters with only phosphorous atoms, as such the trapping of vacancy by Sn atoms is not efficient in inhibiting the deactivation of P[41].

In summary, the co-doping with isovalent atoms so far proposed can delay the diffusion of donors but do little in the way of improving their maximum active concentration.

For what concerns double donor doping, different strategies have been proposed.

Co-doping of arsenic-phosphorous experiments have shown an inhibition of As diffusion, but no effect on P diffusion, while activation was not enhanced[42], [43].

Phosphorus-nitrogen co-doping has been investigated, but the nitrogen addition lowers the activation of phosphorus through the formation of N-P complexes[44]. As of now, co-doping strategies lead to similar result to the isovalent doping case.

The diffusion properties so far introduced demonstrate why the production of shallow regions of highly concentrated n-doped Ge layers is almost impossible by conventional annealing methods. The duration of a thermal anneal process at equilibrium is too long in comparison to the diffusivities of n-type dopants, leading to a massive diffusion of atoms and loss of depth control on the doped layer. At the same time, we have illustrated the issue of clustering for the activation of n-type dopants. A solution to both the issues could be found in ultra-fast, out of equilibrium, processes. The most effective means of activating of n-type dopants are summarized in figure 2.4 that show the achievement of high activation of donors by use of Solid-Phase Epitaxial Regrowth (SPER) and Laser Anneal methods. In this thesis we focus on the Laser Anneal process to obtain high activation of germanium and concurrently inhibiting macroscopic diffusion.

2.3 Laser Anneal Process for Semiconductors

A prime candidate to overcome the above issues so far described is the Laser Thermal Anneal (LTA). This annealing technique is characterized by the fast irradiation of the target material with laser pulses, in order to promote the absorption of the radiation's energy and its conversion to a localized thermal gradient at the material's surface. The LTA process and its effects on the irradiated material are largely dependent on the specific light-matter interaction triggered during the process. The absorption processes depend on the energy of the laser radiation and the specific electronic structure of the target material.

The absorption of laser radiation by metals, where the Fermi level is inside the conduction band, is dominated by intra-band transitions. In this case radiation is absorbed at the first few nanometres of the surface by the electrons in the conduction band and relaxed by electron-electron (e-e) scattering and phonon-electron (p-e) scattering, within characteristic times of $\sim 10^{-14} - 10^{-12}s$ for the e-e scattering, and $\sim 10^{-12} - 10^{-10}s$ for the p-e one. The fast absorption and relaxation times induce highly localized modifications on the surface of metallic layers.

Considering semiconductor's electronic structure, we see that the absorption is governed by interband transitions which have longer characteristic times, and also defect states inside the band gap, making the absorption and relaxation phenomena less straightforward in comparison to the metal case. Indeed, the laser anneal for semiconductor materials is usually split into two different regimes, the UV nanosecond irradiation and the IR millisecond anneal.

In the case of the UV wavelength radiation, the photon energy is higher than the bandgap of the materials, as such the radiation is absorbed by means of interband transitions and consequent generation of electron-hole pairs. The high absorption coefficients of Si and Ge allows for the use of nanosecond laser pulses that are absorbed at the surface of the material (some nanometres) and immediately converted into heat. The hot surface region becomes the source of thermal energy for the system and the diffusion of said energy happens as 1-directional heat front moving towards the inner region.

At IR wavelength the absorption can't happen through interband transitions, since the photon energy is lower than the gap, and the absorption is mainly due to the free carriers, and in a minor part by the phonons. Under IR irradiation the absorption coefficient is largely dependent on wavelength, temperature and doping level. At high doping ($> 10^{17} cm^{-3}$), the carrier-carrier interactions dominate over the interaction between carriers and lattice, and the carriers behave collectively as a plasma pushing the electrons higher into the conduction band and the holes lower in the valence band during the absorption[31]. At low doping the main absorption phenomenon is the phonon excitation and the intrinsic free carriers that get excited reach thermal equilibrium with the lattice, while at high doping we see a temperature distribution of the carriers that needs to relax before reaching the thermal equilibrium. The absorption phenomena for the IR wavelength have longer characteristic times in comparison to the UV case and this explains why the laser pulse is generally longer, in the order of the milliseconds. During a millisecond laser anneal the surface is not the only heated region and the heath distribution is more complex to describe and simulate in comparison to the UV case, as the heat diffusion during the laser pulse is not negligible. The diffusion length of the heath during the pulse can reach the cm depth, comparable to the thickness of a wafer. The large volume of the heated region during the millisecond IR laser anneal is the main reason why nanosecond UV annealing is more appealing as a possible solution to obtain high activation on shallow regions, considering the lower and more localized thermal budget of the process.

2.3.1 Pulsed Laser Melting

When the UV laser anneal transfers enough heath on the material to promote the superficial melting of the target, the annealing process is usually referred to as Pulsed Laser Melting (PLM).

This laser annealing process triggers the melting of the surface layer of the material, where the energy is first absorbed, and subsequently the melted layer moves deeper into the target driven by the heath front. The melting front eventually stops at a certain depth (depending on the laser pulse intensity, wavelength, duration and the specific properties of the material) called *Maximum Melt Depth* (MMD). As described in the previous paragraph, for Si and Ge samples the UV radiation is rapidly absorbed and transformed into heath thanks to intraband transitions that allows the electronic system to relax by transferring the energy to lattice vibrations. The absorption of the laser energy at the surface is just the starting point of the annealing process. While the absorption of the laser energy happens during the laser pulse itself, most of the thermal effect happens after the laser pulse is already ended. The absorption of the laser energy by the electronic system happens in the femtoseconds timescale and the consequent relaxation through phonon-electron scattering happens in the picoseconds regime, both shorter than the pulse duration.

In order for the material to absorb enough energy during the pulse and activate the subsequent solid-liquid transition, the energy delivered by the laser pulse has to overcome the energetic threshold for the initial lattice fusion. This threshold depends mainly on the material properties like lattice energy and on the laser properties itself, like wavelength and intensity. The parameters that affect the energy transferred to the material are the pulse duration τ, the number of pulses, the wavelength and the energy density (ED, J/cm^{-2}). These parameters set the total energy carried by the laser pulse, even if they need to be adjusted considering the absorption coefficient of the specific target material, which sets the effective absorption efficiency and the absorption depth. In most cases wavelength and pulse duration cannot be changed at will, and the laser parameters that can be modified are the energy density and the number of pulses. Considering Si and Ge as target material and the wavelengths of commonly used laser sources (248 nm KrF excimer laser, 308 nm XeCl excimer laser, or 355 nm third harmonic Nd:YAG laser), the melting is triggered with energies in the order of the few hundreds of mJ/cm^{-2}.

The specific energy density required for the melting of the surface may change depending on the phase of the target material, an amorphous semiconductor layer exhibits a lower melting point in comparison to the crystalline counterpart. The doping level of the material can also influence absorption and reflectivity of the surface, by modifying the bandgap and the absorption depth. The surface quality of the target may also influence the absorption efficiency due to an enhanced or reduced reflection.

After the energy is absorbed on the surface, the melted front propagation and consequent recrystallization happen on a longer timescale in comparison to the absorption time, usually in the order of the hundreds of nanoseconds. Simple heath flow calculations for the front propagation had already been developed by the ‘80s[45], [46]. After the absorption of the laser energy and the subsequent conversion into heath, the diffusion of said heath front through the first nanometres of the surface also happens within the laser pulse timeframe. This observation allows for an easier description of the diffusion of the heath into the material, because the first nanometres of the surface can be modelled as a localized heath source and the evolution of the melted layer thickness is analysed with respect to time as the heath flows into the material. The melting layer propagation and subsequent solidification usually occur within hundreds of nanoseconds.

The maximum melt depth and solidification velocity depend on the laser energy density. While the maximum melt depth increases with increasing ED, the solidification velocity has an inverse dependence on the ED. This can be explained by the fact that at higher ED the heath front travels through a thicker layer over time and, by the time the melted layer reaches the maximum depth, most of the heath has dissipated and the temperature gradient between the melted layer and solid one is lower, slowing down the re-solidification[46]. Apart from being able to simulate the melting process through simple heath calculations, these first studies were also able to underline an important characteristic of the PLM process: if the liquid-solid interface stops in contact with a crystalline layer the solidification produces a crystalline regrowth, with the potential to obtain an epitaxial layer.

By comparing the solidification times, hundreds of nanoseconds, and the maximum melt depth, hundreds of nanometres, it’s easy to understand that the re-solidification speeds are on the order of the metres/second. This high solidification speed is the reason why the PLM technique has been proposed to obtain highly doped materials. The solidification speed is much higher than the diffusivity of the dopants, allowing for the impurity atoms to be trapped in substitutional positions at higher concentrations than equilibrium conditions and have a higher control on the dopant depth distribution.

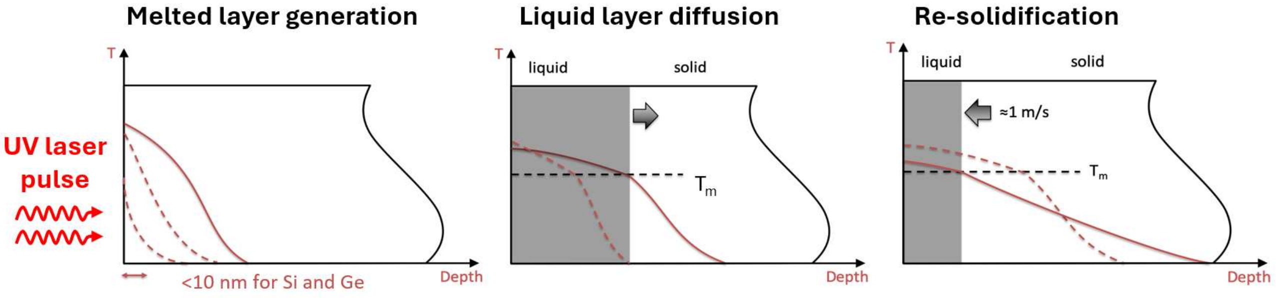

Figure 2.7: A scheme of the PLM process is represented. The laser energy is locally absorbed on the surface of the material, where the heath generates a liquid layer. As the heath front propagates, the liquid layer diffuses until the thermal gradient dissipates enough to trigger the liquid-solid transition. Then, a fast re-solidification occurs with a solid-liquid front travelling at the m/s speed until the surface is reached.

The unique features of the PLM process can be shortly summarized in three main characteristics:

- The fast irradiation and heath conversion produce an extremely high thermal gradient on the liquid-solid interface (around $10^8\ °C/cm$), which in turns promotes a fast solidification (m/s interface speed). This time span is short enough to induce strong out-of-equilibrium conditions, where the speed of the interface is much faster than the characteristic times for atom diffusions so that the impurities are trapped inside the matrix at a higher concentration in comparison to the thermal equilibrium concentrations. The phenomenon is usually described though the effective segregation coefficient k_{eff}[47]:

$$k_{eff} = \frac{k_0}{k_0 + (1 - k_0)\exp\left(-v\frac{\delta}{D_l}\right)} \tag{2.11}$$

  Where k_0 is the equilibrium segregation coefficient as defined in eq. 2.1, δ is related to the maximum melt depth, D_l is the diffusivity in the liquid phase and v is the solid-liquid interface velocity.

- The huge difference in diffusivity of the impurity atoms in the solid matrix and the liquid one allows for the control of the dopant profile, which follows the shape of the solid-liquid interface. Considering that the solid-state diffusivity of the common impurity atoms is around 10^{-20} - 10^{-10} cm^2/s (depending on dopant and temperature, see figure 2.6) and the liquid-state diffusivity is in the order of 10^{-4} - 10^{-5} cm^2/s, it's possible to consider the solid interface as a diffusion wall, and the diffusion into the solid matrix can be neglected[47]. This allows for the creation of box-like dopant profiles, as long as the solid-liquid interface is a homogeneous and flat.

- When the liquid-solid interface starts re-solidifying in contact with a crystalline layer the subsequent solid phase will grow through Liquid-phase Epitaxial Regrowth (LPER). LPER allows the growing layer to replicate the grain structure of the substrate. By tuning the energy density of the laser source it’s possible to modify the maximum melt depth, in order to select a specific depth from which the LPER starts; this permits the engineering of the strain on the regrown layer if the substrate shows a different cell parameter in comparison to the melted layer.

Chapter 3

Sample preparation, processing and characterization techniques

This chapter focuses on the description of the procedures followed for samples preparation, and the characterization techniques used to investigate their properties. The wafers from which the samples were prepared were obtained by Low Energy Plasma Enhanced Chemical Vapour Deposition (LEPECVD), so a brief theoretical insight into sample synthesis technique is provided, along the specifics of the wafers. Then, the specifics of the Laser system utilized for the PLM process are presented (for theoretical background refer to chapter 2). Lastly, both the theoretical background on the characterization techniques and the specifics of the used instruments are given. The thesis work has followed a double approach, part of the thesis was focused on the samples' processing and characterization through common morphological and electrical techniques, while another investigation route has been followed in an attempt to set-up a methodology of investigation through a novel electric scanning probe technique: Scanning Microwave Microscopy (SMM).

3.1 Chemical Vapour Deposition

The wafers from which the samples were processed and characterized, were provided by L-NESS in Como (part of the Physics Department of Politecnico di Milano), thanks to a collaboration between the research groups.

The samples wafers provided by L-NESS consist of:

- Three intrinsic Si (100) wafers, 500 μm thick, with an epitaxial layer of phosprous-doped germanium (Ge:P) grown on top, all characterized by different dopant concentration and thickness of the grown layer

- One intrinsic Si (100) wafer, 500 µm thick, with an epitaxial layer of phosprous-doped silicon-germanuim alloy (SiGe:P) grown on top

In the following scheme a visualization of the four wafers is presented, the wafers are identified by a specific number. A more detailed insight on their characteristics will be provided in chapter 4

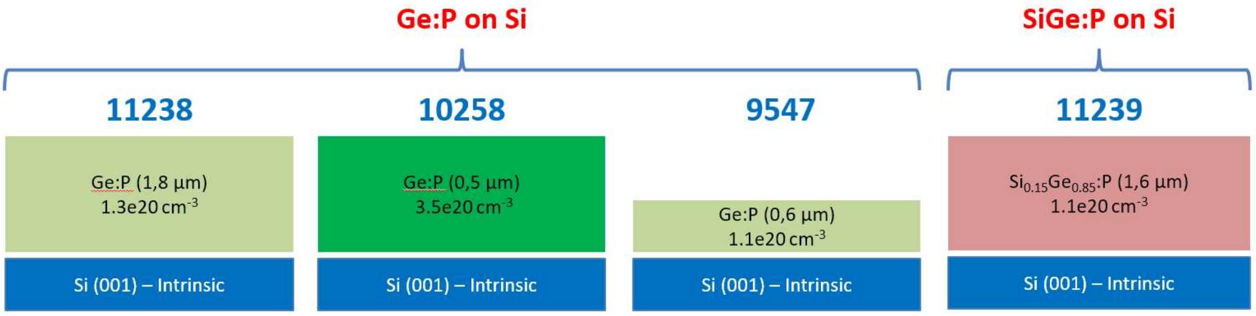

Figure 3.1: Visual representation of the four provided wafer from which the PLM processed samples where produced. The thickness of the grown layer and the chemical dopant concentration (estimated through SIMS measurement) are shown inside the coloured boxes. The visual thickness of the grown layer is enhanced in comparison to the wafer's (500 µm), for ease of view.

All the doped layers were produced by Low Energy Plasma Enhanced Chemical Vapour Deposition (LEPECVD), a variation of Chemical vapour deposition (CVD) better suited for low temperature growth of epilayers.

The CVD is a process aimed at depositing a thin film of material onto a substrate by chemical reaction in a gas phase or on the surface of the subrstrate. In CVD, the substrate is placed in a reaction chamber that is successively filled with a gas mixture containing the precursor chemicals. The so called "precursors" are chemical species selected specifically to perform chemical reactions, or undergo a dissociation, in order to grow a solid product onto the substrate's surface. The reaction/decomposition of the precursors can happen either in the gas phase or directly on the surface of the substrate, in the first case we refer to it as *homogeneous nucleation*, and in the latter as *heterogeneous nucleation*. The energy required to promote the chemical reactions for the layer's growth is usually provided by heating, both the substrate and the walls of the reaction chambers can be heated

- The homogeneous nucleation is usually achieved in the hot wall configuration, where both the substrate and the walls of the reactor are heated. Under these conditions the gaseous precursors introduced in gas phase are provided the energy for the dissociation or reaction with other species before interacting with the substrate surface, while still in the gaseous phase. The reaction in gas phase yields a solid molecule/powder grain and gaseous by-products. The reaction is considered homogeneous because the reactions to produce the final occur in the gas phase. The solid species than is adsorbed on the surface.

- The heterogeneous reaction is usually carried out in a cold wall configuration. In this case, the energy for the reaction is provided mainly by the substate and the reactions occur directly on the surface of the substrate. The gaseous precursors reach the surface, where the formation of the product happens at the gas-solid interface.

The homogenous nucleation usually yields lower quality films with worse adhesion in comparison to the heterogeneous one. For the epitaxial growth of semiconductors layer the heterogeneous nucleation is preferred.

Apart from the classic CVD technique, also called thermal CVD, different variations for specific needs have been developed and the chemical and physicals phenomena that characterize the CVD deposition can slightly vary depending on the specific precursor utilized or by using some variation of the deposition method.

Regardless of the configuration utilized some steps can be considered as the common deposition route for a CVD process:

1) Production of gaseous reactants/precursors via evaporation or sublimation from solid target or liquid solutions.
2) Introduction of the gaseous reactants into the reactor.
3) Reaction of the precursors.
    a) Homogeneous reaction between gaseous reactants (hot wall).
    b) Heterogeneous reaction between the gas phase reactants at the gas-solid interface (cold wall).
4) Absorption of the products on the surface of the substrate in the case of homogeneous nucleation (in the other case the product is already on the surface).
5) Diffusion of the deposits on the substrate's surface where they form nucleation centres and can grow by aggregation and ripening forming homogenous layers or 3D islands.
6) Removal of the gaseous by-products from the surface.
7) Elimination of the by-products and remaining fragments of the unreacted species away from the reaction zone by purging steps.

It's important to note that the physical and chemical reaction that take place during a CVD growth are rarely as straightforward and simple as depicted in the previous scheme and that homogeneous and heterogeneous nucleation may happen during the same process, with one being the statistically favoured one. In the same way the correlation between the hot wall/cold method and homogeneous/heterogeneous nucleation pathway may not always hold, and the chemistry of the precursor has to be thoroughly characterized to control the deposition process.

CVD technique offers several useful characteristics to produce high-quality materials in the semiconductors industry. The first important characteristics is the high uniformity of the deposition process. The average thickness of the layer, as well as the mechanical and chemical properties are tuned by controlling the atmosphere of the reactor, both in terms of pressure and gas flows, and temperature of the process. The control of the gas flows and relative concentration of the reactants can be leveraged to obtain alloys or in-situ doped materials, and by modifying the working temperature the activation of the doped materials can be increased or decreased. It still important to point out that this technique works at thermodynamic equilibrium and as such, the incorporation of the dopants is limited to the maximum solid solubility and the full activation is hindered by the problems introduced in chapter 2.

The simple nature of the precursors allows for the deposition of several categories of materials: amorphous or crystalline Silicon, transition metals, oxides and nitrides. CVD deposition and its variants are among the most common techniques utilized in the semiconductor industry, most notably for the formation of the gate oxide on modern transistor, the formation of metal contacts in electronic devices and the packaging of the finished products with nitride or oxide layers. Moreover, they find ample applications in the optical field for the production of fibres and solar cells. Another advantage of chemical vapour deposition is its industrial scaling. In modern IC fabs, CVD reactors with multiple wafer holder are utilized and introduced into automated production lines. Chamber conditions, such as temperature and gas flows, are continuously checked and automated process of heating, gas insertion and purging are implemented to speed up the production of multilayer devices.

CVD doesn’t come without drawbacks. The precursors can be highly toxic for both the environment and humans, and they usually require great care with handling and storage, as well as the introduction of security measures during several steps of the automated processes. Some of the precursors may also be flammable or explosive. Moreover, the risk of contamination inside the reaction chambers is higher in comparison to other deposition methodologies and the residual byproducts of previous processes may lead to formation of defects on a newly grown layer. The required technologies to accurately control the reaction chambers conditions (gas control systems, homogeneity of the atmosphere and temperature of large volume reactors), their maintenance and the storage of the precursor, make this technology difficult to implement by small manufacturers.

Another drawback is constituted by thermal budget. As devices become more complex and the thermal budget for each process decreases, to avoid deactivation of the doped regions in inner layers, the use of thermal CVD deposition in the production of complex devices has been increasingly challenging. While complex 3D architectures require the growth/coating of complex structures (for instance formation and coating of fins in FinFETs), the heating of the already processed layers on a wafer could be fatal to the final devices. For instance, an excessive heating of a wafer can produce a loss of contact quality between active parts and metal contacts, this may lead to premature failure in electronic devices. This specific drawback of thermal CVD processes can be overcome by implementing a variation that allows for the use of lower growth temperatures and better control over thickness and conformality of a grown layer, the Plasma Enhanced Chemical Vapour Deposition (PECVD).

More specifically the research group at L-NESS uses a Low Energy-PECVD in order to reduce the radiation damage produced by the high-energy ions created by the plasma. The advantage of using low energy plasma stems from the possibility of growing good crystalline quality film of Germanium or Silicon-Germanium alloys at higher deposition rates (10 nm/min) in comparison to classic CVD and at lower temperatures (< 600 °C).

The plasma is generated by first heating a Tantalum filament thanks to high currents. Electrons are released by thermionic emission and argon gas moves through the plasma source, where it is ionized, and reaches the reaction chamber. A current arc discharge can now be triggered and sustained between the chamber and the filament of the plasma source. To stabilize the arc discharge, and the plasma itself, an anode ring is present in reaction chamber, placed between the plasma source and the wafer holder. The substrate is heated from behind thanks to a graphite heater. The energy of the ions (<10 ev) is low enough to avoid damage of the surface and reduce the defectivity of the growing layer.

phosphorus-doped germanium layers are grown by using a combination of germanium precursor (GeH_4), and a phosphorus precursor (PH_3). For the doped SiGe alloy, silane (SiH_4) is added to the mixture. The growth rate is mainly controlled by modifying the concentration of the gas mixture and the current for the plasma discharge, which in turn modifies the plasma density coupled with the control of the magnetic fields. The variation of the relative concentrations of the precursor also tunes the composition of the layer. The temperature has little effect on the growth speed, and it has been demonstrated that lowering the substrate temperature can reduce the threading dislocations concentrations on the growing layer by creating a buffer layer (virtual layer) beneath the layer of interest[48].

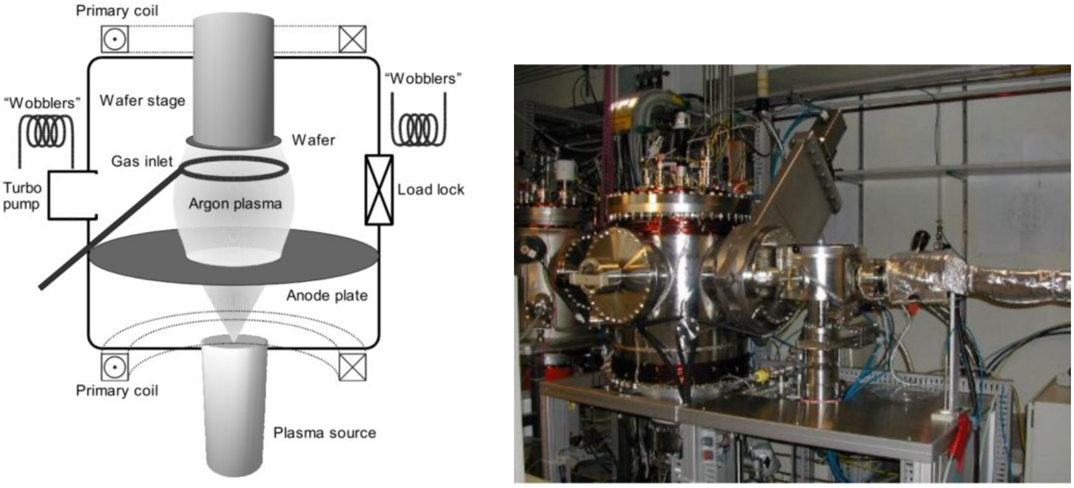

Figure 3.2: Simplified scheme and photo of the LEPECVD instrument used by L-NESS research group

3.2 Pulsed Laser Melting

The first experimental procedure of the thesis work is the laser anneal of the wafers, in order to promote the activation of the dopant in the Ge:P and SiGe:P layers beyond the activation obtained during the CVD growth.
The first laser processes were carried out on the 11238 Ge:P wafer and the 11239 SiGe:P wafer. After the first characterizations, new samples from the other two Ge:P wafers (10258 and 9547) were laser annealed in order to get more data for comparisons and validation.
Some wafers were covered on the surface by a polymer protective layer, that had to be removed before the laser anneal. The cleaning was done through the following procedure with increasing solvent polarity

- HPLC grade 99% Acetone (Sigma-Aldrich) bath to remove the polymer
- Milli-Q water bath
- Iso-Propyl Alcohol bath to remove the last organic residues that may still be present on the surface

The samples were kept in each bath for one minute, at room temperature. After each bath the samples was recovered and the remaining solvent was quickly removed by spraying a bit of the next solution in line directly with a pipette, before putting them in the subsequent bath. This was done to reduce contamination between the baths and avoid staining of the surface by solvent evaporation. The Iso-Propyl Alcohol is removed by compressed air.

The natural oxide is stripped from the samples surface just before conducting the laser process. A light HF etching is applied to remove the oxide. The sample are submerged in 10% HF aqueous solution for 1 minute at room temperature, and subsequently cleaned with pure water, through various washing cycles, to dilute the acid wastes.

After the cleaning step, the wafer pieces were put into the laser chamber and the process was controlled by a software interface that allows for the control of laser energy density and the position of the laser spots on the samples. Different laser spots can be annealed at different energy densities, allowing for more flexibility in a single process run.

The instrument used for the laser anneal, a Coherent COMPex 201 KrF excimer laser, is placed in the Laser Processing laboratory in the Department of Physics and Astronomy at the University of Padova (DFA). The laser is produced by electrically pumping an active gas mixture of Kr, F_2 and Ne buffer, thanks to high voltage discharges. The gas mixture is constantly mixed thanks to a fan, during the laser activity, in order to obtain a more stable laser emission by avoiding separation of the gas components.

The instrument emits an UV laser radiation at $\lambda = 248$ nm, with pulse duration $\tau \sim 22$ ns. The laser beam is then redirected along the optical path, thanks to 90° reflective optics. Inside the beamline the laser is directed towards the sample stage though a system of multiple lenses. The optical components inside the beamline have multiple functions, a first set of lenses has the function to correct the initial shape of the laser, a collimating lens ensures a good parallelization of the incident light on the sample, a focusing lens is used to set the focus of the laser on the sample's surface. The instrument also allows for utilization of metal masks to control both the shape and dimension of the laser. The entire optical path is sealed and continuously kept under N_2 atmosphere in order to reduce the wear of the optical components and increase the system's lifetime. The sample holder is constituted by a mechanized stage where both the z-height and x-y plane can be monitored and set, the stage allows for the production of successive patterns onto the sample during a single process run. A custom interface, developed by the research group, grants an easy control of several parameters of the laser system: laser energy, repetition rate (1-10 Hz), calibration of the stage positioning and the ability to produce excel recipes with the desired laser spots pattern on the sample. The laser source is able to produce pulses with energies in the range of 300-750 mJ with a new gas mixture. This energy range is dependent on the refill state of the gas mixture and the range can get as low as 50-250 mJ when the mixture is nearly exhausted. Depending on the energies required for a process, a refill may be necessary. The energy density (ED) effectively delivered on the sample surface can be tuned not only by controlling the laser emission energy but also thanks to a doble mirror motorized attenuator that is able to tune the energy of the laser after its emission. The laser energy densities that can be delivered on the sample are in the range of 40-1200 mJ/cm^2. It's not possible to cover the full range of energy densities within a single process run because the maximum laser energy is set before the process and then the attenuator comes into play to deliver the selected energy for a spot. The attenuator has an optimal working range of 8-98% attenuation, so the highest attenuation limit sets the lowest energy density allowed for a process run while the lowest attenuation sets the maximum energy density. The energy density that reaches the sample can be monitored thanks to an in-line diode that records the energy for each pulse delivered. A variance between the set energy and the delivered one is usually observed up to a 5%.

The widest ED range covered during the processing of the sample is 300-900 mJ/cm^2, wich could be achieved during a single process run. A 5x5 mm mask was used to produce spots of the same size. A scheme of the instrument is provided in figure 3.3

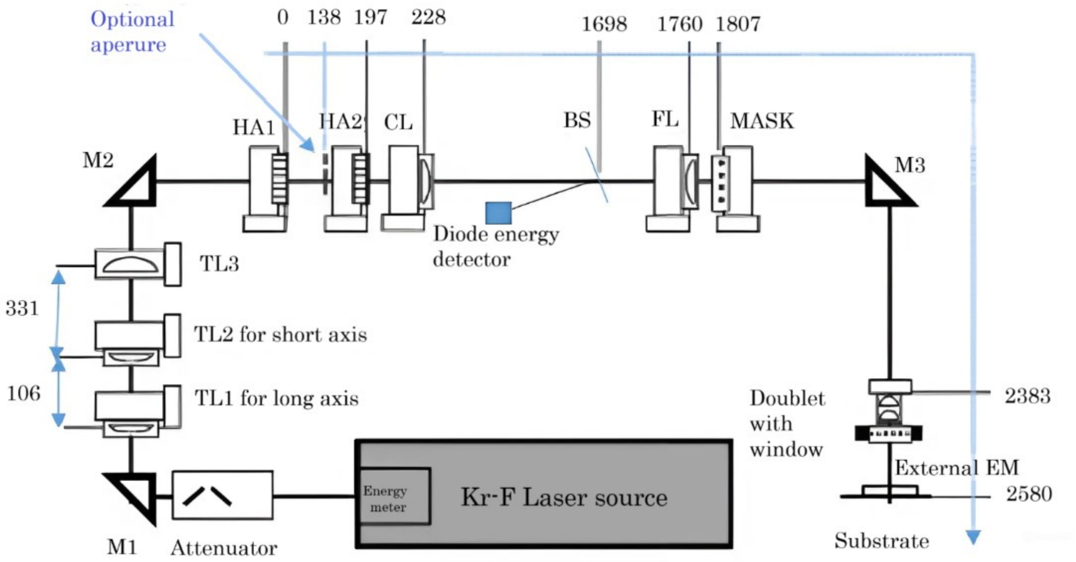

Figure 3.3: Scheme of the Compex 201 Kr-F laser and optical path used for the PLM processing of samples. The highlighted components are the mirror and lenses that homogenize, collimate and focus the laser beam onto the sample.

3.3 Characterization techniques

3.3.1 SIMS

Secondary Ion Mass Spectrometry (SIMS) is a highly sensitive analytical technique used to extract information about concentration and depth distribution of impurities and matrix atoms for solid materials. Thanks to this technique it’s possible to detect atoms concentrations inside a solid matrix with concentrations down to the part per million (ppm) or even part per billion (ppb). During a SIMS analysis the sample surface is bombarded with an accelerated ion beam, referred to as primary beam. The primary beam is focused through a set of electrostatic lenses and directed toward the sample. While the impinging ions impact the surface, they also damage it and remove atoms during the analysis. This effect is usually referred to as a process of sputtering and the extraction of surface atoms is leveraged to get composition information form the sample. While the majority of the extracted atoms are neutral, a small portion is ionized by the interaction with the charged primary ions and can be accelerated thanks to an electric field and analysed inside a mass spectrometer. When the sputtering process reaches a good stability, the ionized extracted atoms that are accelerated to constitute the so-called secondary beam. The ionization of the sputtered atom is a necessity since the mass spectrometer detects the mass of the ions thanks to a mass/charge ratio (m/z). In a mass spectrometer the calculation of this ratio can be achieved thanks to different analysers like magnetic sectors, time of flight detectors, quadrupoles or orbitraps, to name a few. Regardless of the detector used, the basic idea of selecting the ions thanks to the interaction with an electromagnetic field is at the base of the mass identification. The secondary beam intensity is finally measured with Faraday cups or electron multipliers, depending on the signal's magnitude. The overall mass resolution is very high and allows to discern elements with $\Delta m/m$ up to the order of 10^{-4}. In order to achieve such high sensitivity, the whole setup, and the sample chamber in particular, needs to be kept under ultra-high vacuum conditions, usually 10^{-9}~10^{-10} mbar. The vacuum is necessary to achieve the best possible conditions for both the sputtering process and detection process of the secondary beam. The ions of the primary beam must reach the surface of the sample without interaction with the atmospheric atoms and molecules that reduce their mean free path and can de-ionize them, leading to a decrease in the sputtering effect. At the same time, the vacuum also improves the detection of the secondary beam and reduces the probability of contamination in the chamber.

The SIMS analysis performed on the samples during the thesis had the objective of not only giving an estimate of the chemical composition of the samples (both dopant and matrix atoms, Si and Ge) but also acquiring a depth dependant profile in order to evaluate the effects of the laser processing on the redistribution of the species. In order to achieve this objective, dynamic SIMS were performed. During dynamic SIMS measurement it is possible to correlate the detected atoms mass, and concentration, to the depth from which the secondary ions are being released, in order to produce a concentration profile with respect to the depth. By raster scanning the sample with the primary ion beam it's also possible to acquire 3D ion images of the sample, although the process requires a long time. It is noteworthy to report that a SIMS measurement can also provide information on the isotopic composition of the target material.

The instrument used to acquire the SIMS profile is a Cameca IMS 4f, located at the DFA. A scheme of the instrument is provided in image 3.4.

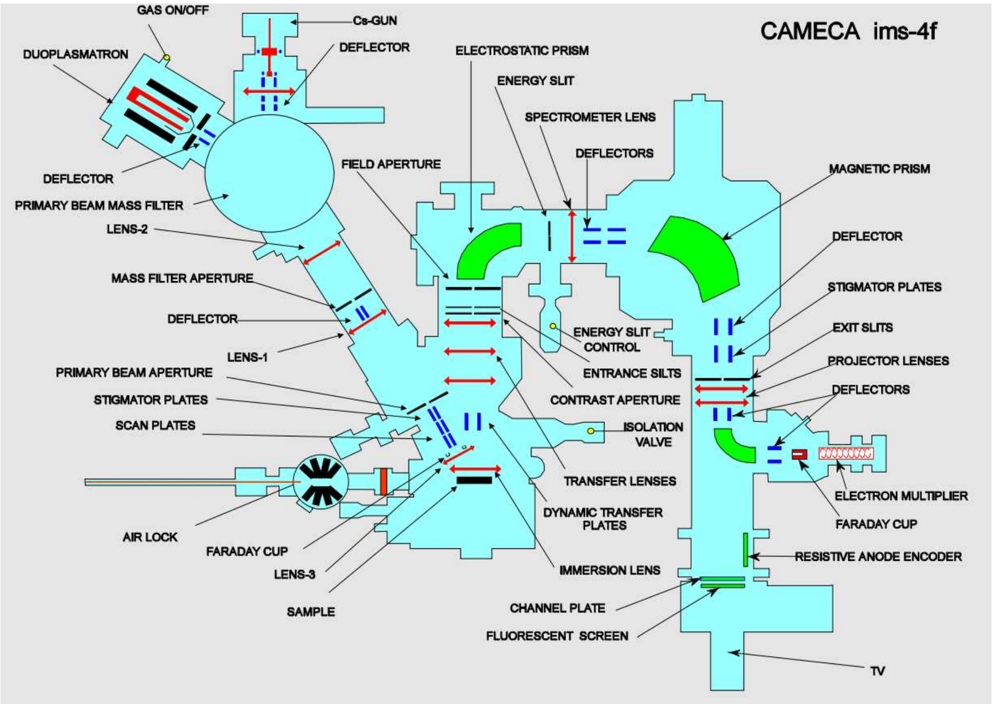

Figure 3.4: Schematics of the Cameca ims-4f at the DFA. The source oxygen ion source is a duoplasmatron capable of generation both positive and negative oxygen ions. The Cs source only produces positive ions. The mass detection is entrusted to a magnetic sector spectrometer preceded by and electrostatic sector. Four different detectors are available, depending on ion energy and secondary beam intensity. The resistive anode detector is used for ion imaging.

The instrument is equipped with two different ion sources for the primary beam: an O_2^+ ion source and a Cs$^+$ source. The specific source used for a measurement is selected depending on the ionic species to be detected.

The oxygen ion source is mainly used for the detection of metallic elements, that being electropositive, have a higher tendency of being ejected as positive ions when an oxygen ion hits the surface of the sample and attracts electrons to itself.

On the other hand, the Caesium source is used for electronegative ions that have a higher chance of being released as negative ions, this is explained by the fact that Cs ion bombardment lowers the work function of the surface atoms allowing their electrons to transition to an excited state and enhance their dissociation as negative ions.

The element of interest for the samples under study are the matrix elements Ge, and also Si for the alloy, and the P dopant. For this specific application, the Cs$^+$ source have been selected, and the CsP$^+$, CsGe$^+$ and CsSi$^+$ secondary ions were collected during sputtering. This measurement protocol is known to guarantee better linearity of the ion yields as a function of the element concentrations [49]

The dynamic SIMS analysis is a time dependent experiment where the concentration of the elements is calculated as the sputter process digs into the sample, and in order to convert the time unit into a depth unit its necessary to know the speed at which the ion beam is excavating, this parameter is called *sputtering rate*. A simple way to estimate the sputtering rate is to identify the total depth of the crater at the end of the sputter process and divide its value by the total process time.

In the case of our measurements the depth of the crater is obtained thanks to a Tencor P17 stylus profilometer.

Once the sputtering rate has been obtained, the concentration profile of the samples can be obtained by converting the mass spectroscopy counts into atomic concentrations. To do so it's necessary to use a reference material of known composition. The reference material should be as similar as possible to the sample under study.

The first step to calculate the concentration of an element inside the sample is to first obtain the *relative sensitivity factor (RSF)* for that element inside the matrix of a reference sample:

$$RSF = \frac{I_{MR}}{I_{ER}} D_{ER} \tag{3.1}$$

The RSF for an element is given by the intensity of the signal of the matrix element (counts per second, cps) divided by the intensity of the signal for the impurity element inside the matrix, multiplied by the known concentration of said element (at./cm^{-3}).

Once the RSF for an element is calculated form the reference sample it's possible to convert the signal of the element of interest from the unknown sample into a concentration with the simple formula:

$$N_E = RSF \frac{I_E}{I_M} \tag{3.2}$$

For the Ge:P samples under study the concentrations have been calculated by using a reference sample of Phosphorous in a Germanium matrix to ensure an optimal estimate. For the SiGe:P sample a similar sample was not available and the same RSF as in Ge:P was assumed. As a consequence, the estimation of the chemical concentrations might be affected by a slight error produced by a variation of the RSF by the Si atoms in the matrix.

An important characteristic of the SIMS measurement is that it's a destructive method and should be only performed on the samples after the all the other non-destructive techniques have been utilized. As such the SIMS measurement on the samples have been performed as the last steps of the characterization after the electrical and morphological investigations.

3.3.2 Raman Spectroscopy

Raman spectroscopy is a non-destructive optical technique that has gained popularity in semiconductor characterization thanks to its ability to identify various properties like strain state, doping activation and crystalline quality.

When light impinges upon condensed matter it undergoes a process of elastic scattering by interacting with its constituents (atoms, molecules and macroscopic defects like dislocations). The elastic interaction is usually referred to as *Rayleigh scattering* and the reflected light has the same characteristic of the incident light (wavelength and frequency) apart form a different direction of propagation. A certain fraction of the incident photons can also undergo a series of inelastic interactions that can be grouped under the broad definition of *Raman scattering*. The portion of photons that interact with matter by Raman scattering depends on both the wavelength and the electronic structure of the material, the fraction of Raman scattered photons over the Rayleigh one is in the magnitude of one in 10^6.

The inelastic scattering con occur through interaction with various means, light can interact with phonons, plasmons, electronic excitations and other quasiparticles. In this brief description of the Raman spectroscopy, we will focus on the inelastic interaction between light and the free vibrational modes of the semiconductor crystal that can give us an insight into some useful properties of the material.

The simplest inelastic interaction that can occur between a photon and a phonon is a first order process where an incident photon of energy $E_i = h\nu_i$, with ν_i being its frequency, and wave vector k_i, can interact with a phonon of the crystal with energy $E_q = \hbar\omega_q$, with q being the phonon wave vector. The interaction occurs while obeying the conservation of both energy and momentum, so the energy and momentum of the scattered photon follow the relations:

$$E_s = \hbar\nu_i \pm \hbar\omega_q \qquad 3.3$$

$$\hbar k_s = \hbar k_i \pm \hbar q \qquad 3.4$$

The ± sign takes into account that the interaction can happen both with absorption of a phonon energy to produce a higher energy photon or the opposite, where a photon excites a low energy phonon and is scattered at an energy equal to the incident one minus the energy required to excite the phonon. The same can happen for the momentum. When the interaction occus with the absorption of a phonon and production of higher energy photon, we refer to it as *anti-stokes shift*. The loss of photon energy to excite a phonon is called *stokes shift*. The anti-stokes shift is usually less likely to occur, at room temperature, than the stokes one considering that the phonon population is low and the probability of interaction with a photon is low. On the other hand, the excitation of a vibrational mode is favoured because there are many unoccupied energy states than can be populated.

We can show a generic Raman scattering process with the classic representation of a first order interaction, fig 3.5:

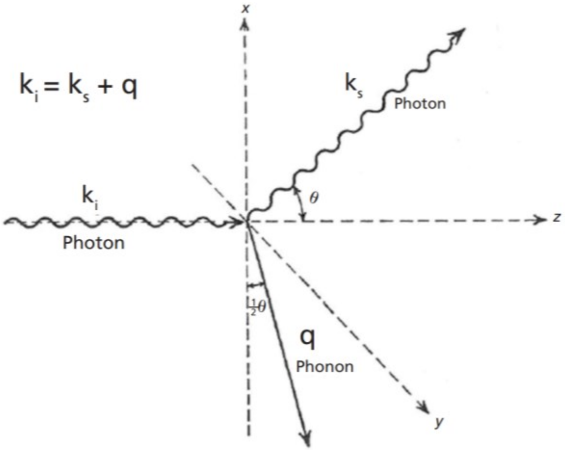

Figure 3.5: Diagram of a first-order photon-phonon interaction. The scattered photon energy must obey the energy conservation principle, the propagation direction is altered to respect the conservation of momentum.

In a standard Raman configuration, a laser light source is used. As introduced before, the inelastic scattering is a low probability process and as such a high photon density is required to obtain a detectable signal. The laser source allows to have a highly intense and monochromatic incident light beam that can also be focused to small size, opening to the possibility of obtaining information form specific regions of a sample (important for devices characterization, where adjacent features may have different structure or doping levels).

The scattered radiation is collected and represented on a spectrum, where the intensity is shown with respect to its wavelength. More specifically, in Raman experiments, the intensity is represented with respect to the "Raman-Shift", which is the difference between the incident wavelength (laser source wavelength) and the scattered one, expressed in wavenumber (cm^{-1}). The choice of this representation stems from the simple observation that the Raman shift is directly correlated to the energy of the vibrational mode that has been excited or absorbed. This allows the identification of the characteristic vibrational modes for a specific material and to monitor their variation in energy with respect to a modification of the lattice (strain, doping, alloying...). Usually, the stokes shift are monitored, given the higher scattering probability, hence a more intense signal. The ratio between the intensity of the stokes and anti-stokes signals can be used to estimate the temperature of the sample[50].

The energy and wave vector conservation for a periodic, crystalline structure imposes some restrictions on the vibrational modes that can be effectively excited through Raman spectroscopy. For semiconductors material we know that a good representation of the periodic structure of the material is the restriction to the 1st Brillouin zone that contains all the possible wave vectors allowed by the crystal.

By referring to the diagram in figure 3.5 we can translate the equation of the momentum into a vectorial relation for q:

$$q^2 = k_i^2 + k_s^2 - 2k_i k_s \cos(\theta) \tag{3.5}$$

Considering an incident photon wavenumber of 15000 cm^{-1} (visible green light), a phonon with a wavenumber of some hundreds (as observed for Si-Si and Ge-Ge raman modes) and a scattered photon with a similar energy to the incident one, we can approximate $k_i \cong k_s$.

For a backscattered photon ($\theta = 180°$), equation 3.3 gives a $q \cong 2k_i$

By substituting the relation between k and λ in q we get:

$$q = 2k_i = 2\frac{2\pi}{\lambda} = \frac{4\pi\nu}{c} = 4\pi\tilde{\nu} \tag{3.6}$$

Where the frequency, ν, over the speed of light, c, gives us the wave number $\tilde{\nu}$. The wave vector q of the phonon can be calculated by substituting in the previous equation the wavenumber of the incident light:

$$q = 4\pi\tilde{\nu} = 4\pi(15000\ cm^{-1}) \cong 1.9\ x\ 10^5\ cm^{-1} \tag{3.7}$$

We can calculate the value of the wave vector at the edge of the Brillouin Zone (BZE), considering that the lattice parameter is in the order of the angstrom, we can use the Germanium parameter of 5.545 Å from[51]:

$$k_{BZE} = \frac{\pi}{a} = \frac{\pi}{5.545\ x\ 10^{-8}\ cm} \cong 5.7\ x\ 10^7\ cm^{-1} \tag{3.8}$$

There is a difference of almost three orders of magnitude between the wave vector of a phonon at the edge of the Brillouin Zone and the phonon that can be activated with the wavelength of the Laser light. This implies that only the Raman scattering from phonons of a very long wavelength, and small k value, near the Brillouin zone centre and up to 2.5×10^5 cm^{-1} will be excited, because of the conservation of energy and wave vector. Moreover, considering that in the vicinity of the centre of the Brillouin zone the dispersion relation curve has a slope of almost zero, the frequency of the phonon in this region has little variation. These considerations justify the presence of few Raman peaks in a crystalline semiconductor, and their narrow shape.

To classify and recognize the Raman peaks observed for a crystalline semiconductor sample its necessary to refer to the group theory. Silicon, Germanium and the SiGe alloy, adopt the diamond cubic structure (O_h point group). For this structure the most relevant first order Raman active mode is the Transverse optical mode (TO) belonging to the F_{2g} irreducible representation. For pure, crystalline, semiconductors with a cubic structure this optical mode appears as a sharp peak in the Raman spectrum.

For Silicon the TO mode appears at 520 cm^{-1} while for Germanium it's at 300 cm^{-1}, for the alloy the Ge-Ge TO mode and Si-Si TO modes are shifted depending on the composition of the alloy[52].

Alterations to the structure of the material, like doping, alloying and introduction of strain can modify the shape and position of the peak. For instance, a partial amorphization of the crystal structure leads to lower intensity peaks with a broader shape. The introduction of a certain degree of amorphous phase relaxes the selection rules and the TO peak becomes broader, as the material has access to a wider distribution of phonons around the centre of the Brillouin zone.

The Raman instrument used during the thesis is a Horiba XploraPlus micro-Raman located at the Department of physics and Astronomy at Padua University (DFA). The system is characterized by high flexibility thanks to the possibility of using three different laser sources (532, 638, and 785 nm) and three diffraction gratings (2400, 1800 and 1200 gr/mm). The best grating for a specific investigation is selected to achieve the best compromise between spatial resolution and spectral range. The laser beam is focused onto the sample thanks to four interchangeable objectives (5x, 10x, 50x and 100x).

Figure 3.6 allows us to briefly describe the specific working of the instrument.

- The laser source generates the beam.
- The beam meets the first lenses used to focus the beam.
- The beam power can be filtered before reaching the sample (0.1, 1, 10, 20 or 50% reduction) in order to select the best intensity for the sample. This allows to find a good compromise between the scattered light intensity and heating of the sample, which can also be reduced by choosing a less energetic wavelength for the laser source, reducing the thermal effect on the Raman peaks.
- The laser beam is focused on the sample thanks to various objectives with different zooms and optical apertures.
- The scattered beam is collected by the same focusing lens and then travels along the optical path.

- The Rayleigh filter cuts parts of the scattered radiation in order to eliminate the contribution from elastic scattering of the laser. In our instrument, for each laser source, an edge filter is provided. The edge filters cut the radiation at lower wavelength than the laser line, meaning that the Rayleigh and anti-stokes signals cannot be measured. The lowest stokes Raman shift that can be measured is 50 cm^{-1}.
- The stokes radiation is focused on a pinhole that prevents the out-of-focus radiation to reach the spectrograph.
- The signal is focused on a slit at the entrance of the spectrograph where it's collimated by a curved mirror, onto a motorized grating.
- The grating disperses the different wavelengths of the incoming signal.
- The instrument is equipped with an asymmetrical Czerny-Turner spectrograph. The position sensitive CCD counts the photons that reach each region of the active surface and reconstructs the spectrum by attributing a wavenumber to each detected photon, based on its position on the CCD area.

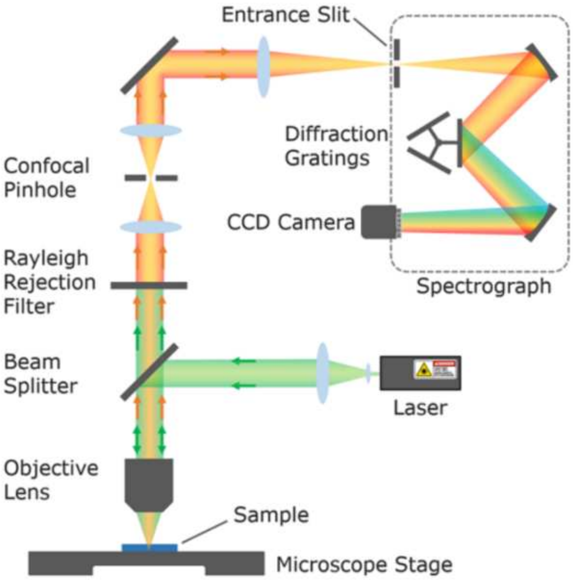

Figure 3.6: Schematic representation of the Horiba XploraPlus micro-Raman at the DFA

The Raman spectra for all the samples have been acquired by working with the 638 nm laser source and the 1800 gr/mm grating. The penetration depth of the laser radiation for Germanium at this wavelength is around 60 nm [53], allowing the Raman spectroscopy to characterize the effects of the LPER regrowth on the surface of the samples without any contribution form the bulk. The main investigated property for the sample is the strain, induced by the PLM process. The thermal gradient generated in the regrown layer and the fast recrystallization accentuates the difference between the thermal expansion coefficient between the different atoms in the matrix, mainly germanium and silicon[54].

3.3.3 Atomic Force Microscopy

Atomic Force Microscopy (AFM) is a high-resolution scanning probe microscopy technique used to map the surface topography of materials at the atomic or nanometer scale. It is widely used in research field thanks to its versatility and relative ease of use. AFM can acquire images with a nanometric, or even angstrom, resolution of a wide range of materials. It's possible to investigate both conductive and non-conductive materials as well as liquid samples and soft matter.

It belongs to the family of the Scanning Probe Microscopy (SPM) techniques. SPM are characterized by the interaction of a probe, usually a sharp tip, with the surface of the sample thanks to specific physical interactions, like Van deer Wall, electrical or magnetic forces, and even other phenomena like electron tunnelling between tip and sample. By leveraging these interactions, a probe microscopy is able to map a property of the sample with high resolution. In order to achieve the best stability and resolution for the system, a feedback loop is usually employed in order to rapidly respond to small variation of the followed property on the sample.

During an AFM scan, the probe is lowered onto the sample at a close distance, in the range of the nanometres or even angstrom, where the interaction is dominated by the Wan-Der Walls forces and Coulombian interactions. In this regime, depending on the tip-sample distance and the specific properties of the sample, a repulsive or attractive force is generated. The establishment of the force acts on the tip that is mounted on a cantilever, producing a deflection that is measured and converted into a topographical information. The interaction between tip and sample is always kept in check by a feedback loop that is able to regulate this interaction in order to better follow the variations in height (or force) during the scan, this allows to both protect the tip from damage and achieve a better sensitivity of the system. The specific parameter that is adjusted depends on the mode of operation as will be explained next.

AFM measurements can be done though three different modes depending on the specific interaction regime between the tip and the sample.

- **Contact mode**: in this configuration the tip is placed in strong contact with the sample, where the interatomic repulsive forces are at play (0.2-0.3 nm of distance). In this mode the tip-sample interaction is relatively strong (the force can reach the hundreds of nN) and its better suited for hard samples or very flat ones. In this mode the image can be acquired by working in constant height mode or constant force. In constant height the fixed parameter is the height of the cantilever-tip system, and the topography is reconstructed by converting the deflection of the cantilever in a height coordinate. In constant force, on the other hand, the fixed parameter is the deflection of the cantilever that is first converted into a force parameter and then kept as constant by constantly adjusting the height of the cantilever holder (usually through a piezoelectric actuator) in order to keep the same deflection. This mode allows for a better control of the interaction strength and to characterize softer materials by setting a lower deflection parameter

- **Semi-contact mode**: in this configuration (also referred to as tapping mode) the cantilever is put under oscillation at its resonant frequency, or slightly below, and the mean distance between the tip and the sample is the region where attractive and repulsive forces are both at work depending on the slight variations of height. The tip is periodically lowered down on the sample, where it goes into repulsive contact, and the stronger interaction with the sample limits the amplitude of the cantilever vibration. The amplitude of the vibration is used as the feedback parameter and the height of the cantilever is modified in response the variation of amplitude. The advantage of this mode is that it allows for the scan of both hard and soft materials while also preserving the tip in comparison to contact mode, since the contact regime is only achieved for short durations
- **Non-contact mode**: Similarly to tapping mode in this mode the cantilever is put into oscillation around the resonant frequency for the cantilever, but in this case the tip-sample interaction is purely attractive since the tip is always kept at a distance to the sample. This mode usually offers a lower resolution in comparison to the other two modes because of the lower intensity of the attraction forces to the repulsive one but and its usually used when dealing with extremely soft and fragile samples

The AFM instrument used for the surface characterization of the samples during the thesis is a Flex-AFM by Nanosurf, available at the DFA, placed on an active air suspension table to reduce external vibrations. The instrument follows a classic atomic force microscope principle with the notable difference of having an electromagnetic flex scanner for the X-Y plane and a piezoelectric actuator for the Z coordinate. The use of the electromagnetic scanner for the X-Y plane is justified by the high linearity of this type of scanners and the absence of creep effect that usually affect the piezoelectric devices. This scanner grants a fast and precise movement over the surface of the samples while also enabling the scan of large areas up to 100x100 μm. The Z coordinate is controlled by a classic piezoelectric device that ensures the highest precision in a narrow range of motion (max ± 5 μm). The deflection of the cantilever is revealed by a laser deflection system. A red laser is pointed at the tip of the cantilever and reflected towards a 4-quadrant position sensitive photodiode detector that translates the voltage in the photodiode into a calculated deflection. The instrument is highly versatile and permits the use of the three classic AFM modes described above and an entire suite of other microscopies. The instrument is equipped with external modules that allow for the use of electric microscopy techniques and mechanical properties like stiffness and adhesion of organic and biological samples.

All the morphological images have been acquired in semi-contact mode with a PPP-NCHR tip. This tip has a nominal apex of 7 nm and is made of highly doped silicon to dissipate static charges.

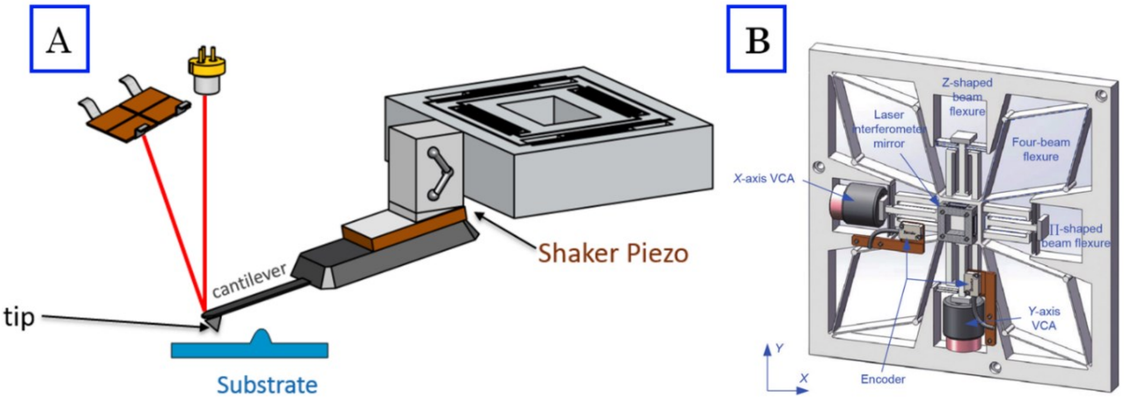

Figure 3.7: Representation of the cantilever-tip system (A). The Z-axis piezo for height control is also coupled with a shaker piezo that allows for the use of the dynamic modes, where the cantilever is put into oscillation. A close-up on the electromagnetic scanner shows the two electromagnetic voice coils actuators (VCA) used to produce the movement on the x-y axis by acting on the flexible beams stage, where the cantilever is mounted (B).

3.3.4 Van der Pauw-Hall method

The Van der Pauw characterization is one of the most widely used methodologies used to extract relevant electrical properties in a quantitative way for semiconductor materials. Thanks to this characterization it's possible to obtain the sheet resistance (R_S) from a sample, from which the resistivity (ρ) can be calculated. The Hall effect is exploited to calculate the carrier dose, from which mobility (μ) and carrier concentration can be obtained. In order to achieve quantitative measurements, it's necessary to know the depth of the active layer inside the sample. The method is also called four-point method as the experiment is performed by contacting the perimeter of the sample with four metallic tips.

This characterization technique was first introduced by physicist Leo J. van der Pauw in its original study from 1958[55]. He demonstrated the ability of this technique to characterize electric properties of flat samples of arbitrary shape as long as some prerequisites are satisfied.

The conditions are the following:

- The contacts should be placed at the edges of the sample.
- The size of the contacts should be negligible in comparison to the sample surface. It's also necessary to satisfy the condition that the size of the contact should be much smaller than the distance between them.
- The sample has a homogeneous thickness.
- The surface of the sample is singly connected, meaning that no isolated hole should be present on the surface.

While the technique works for an arbitrary shape, a square geometry with the four probes placed at its edges proves quite practical in terms of sample handling and positioning. The contacts are usually identified by progressive numbers in a clockwise or counterclockwise order, from 1 to 4.

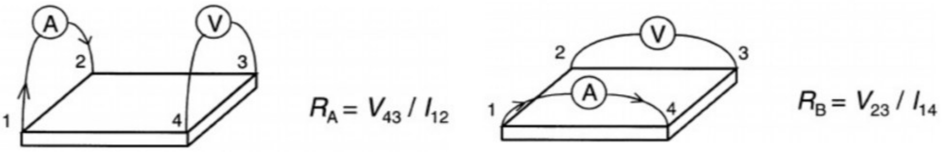

Figure 3.8: Common van der Pauw configuration for a square sample. A current is injected between two contacts and the potential produced is measured between the other two contacts. The basic experiment requires at least two measurements.

In this configuration, the resistance $R_A = R_{12,34}$ is defined as the ratio between the potential difference between contacts 3 and 4 (V_{34}), and the current applied between the contacts 1 and 2 (I_{12}). By switching the direction of the current and voltage by 90 degrees it is also possible to obtain another value of the resistance, $R_B = R_{23,41}$. From these resistance values it is possible to identify sheet resistance R_S thanks to the relation:

$$e^{-\pi R_A/R_S} + e^{-\pi R_A/R_S} = 1 \qquad 3.9$$

To achieve a higher accuracy, it's possible to also acquire the reciprocal values of the resistances R_A and R_B. Considering the theorem of reciprocity that states that $R_{12,34}=R_{34,12}$, making a repetition of the measurement by switching the position of the contacts where the current is supplied with the ones where the potential is checked we can make get an average of the R_A and R_B values. Finally, by also inverting the direction of the applied current and voltmeter polarization, a better estimate of the average sheet resistance is achieved.

$$R_A = \frac{R_{12,34} + R_{34,12} + R_{21,43} + R_{43,21}}{4} \qquad 3.10$$

$$R_B = \frac{R_{23,41} + R_{41,23} + R_{32,14} + R_{14,32}}{4} \tag{3.11}$$

Once the R_s has been calculated, the resistivity of the sample can be obtained by accounting for its thickness:

$$\rho = R_S \cdot d \tag{3.12}$$

In order to evaluate the active carrier concentration and their mobility, the Hall effect can be exploited. The Hall effect is the production of a voltage difference (the Hall voltage, V_H) across a current carrying conductor in the presence of a magnetic field perpendicular to the current. The resulting Hall voltage is perpendicular to both the current and the magnetic field with a magnitude given by:

$$V_H = \frac{IB}{qnd} \tag{3.13}$$

With I being the input current, B the magnetic field, d sample thickness, q the elementary charge (1.602×10^{-19} C) and n the carrier's bulk density. In some cases, as that of a thin homogeneously doped layer, it is convenient to use sheet dose $n_s = nd$ instead of bulk density.

The Van der Pauw-Hall technique makes use of this phenomenon by applying a constant magnetic field perpendicularly to the sample and injecting an input current between two opposite contacts, for instance 2 and 4, and detecting the Hall voltage between the remaining two (1 and 3 in this case).

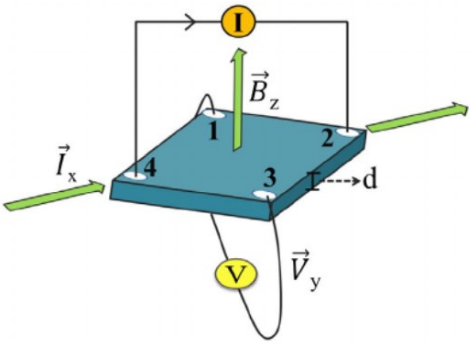

Figure 3.9: Representation of a Hall experiment. The input current is applied in the x direction and the magnetic field is applied perpendicular to the sample, on the z axis. The Hall voltage is generated perpendicularly to the magnetic and electric vector, the y direction, where it's detected.

For this configuration it's possible to average the experimental results by inverting the direction of the magnetic field and by applying a permutation of the contact roles.

The Hall characterization yields the Hall coefficient, RH_S, defined as:

$$RH_S = \frac{V_H}{IB} \tag{3.14}$$

From this value both the Hall mobility and the sheet dose (that will be called *Hall dose* from hereon) can be extracted:

$$n_{s,H} = \frac{IB}{qV_H} = \frac{1}{qRH_S} \tag{3.15}$$

$$\mu_H = \frac{1}{qn_SR_S} = \frac{RH_S}{R_S} \tag{3.16}$$

The Hall coefficient can be corrected to account for the variation between the normal scattering conditions of the carriers subjected to an electric field and the scattering provoked by the inevitable application of the magnetic field necessary for the Hall measurement, that can introduce magneto-resistive scattering. This factor is called Hall scattering factor, r_H, and it is defined as the ratio between the Hall mobility and drift mobility:

$$r_H = \frac{\mu_H}{\mu_d} \tag{3.17}$$

In most cases this value is put equal to unity, ignoring the effect of the magnetic field on carriers' mobility.

However, considering the high doping of the samples studied during the thesis, a value of $r_H = 0.87$ has been used a correction factor, valid for highly n-doped germanium[56].

By accounting for the Hall scattering factor, the Hall dose can be converted into the drift dose, $n_{s,D}$, and then drift carrier concentration, n. The Hall mobility is also converted into its drift counterpart, μ_D:

$$n_{s,D} = \frac{r_H}{qRH_S} \tag{3.18}$$

$$n = \frac{n_{s,D}}{d} \tag{3.19}$$

$$\mu_D = \frac{RH_S}{r_HR_S} \tag{3.20}$$

The van der Pauw-Hall theory introduced up until now refers to flat samples with homogeneous doping profiles throughout the entire depth of the active region. But the laser annealing process, necessary to obtain high doping out of equilibrium, is characterized by a maximum melt depth, as already discussed. The maximum melt depth can be seen as the threshold depth up to which most of the out-of-equilibrium activation process occurs, considering that melting stops in this region. Accounting for the characteristics of the laser anneal process a double layer model has been applied to extract the electrical information of the laser processed samples.

In the case of van der Pauw-Hall measurements, the samples can be considered as being composed of two layers with different electrical properties and thicknesses placed in parallel.

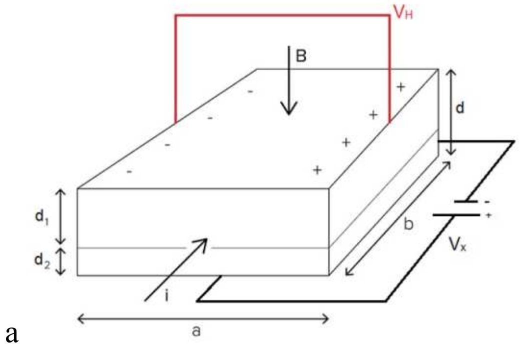

Figure 3.10: Representation of the bilayer model adopted for the interpretation of the Van der Pauw-Hall measurements on the laser annealed samples. The layer on top represents the region affected by the laser process, while the deeper region can be considered as a non-processed layer in terms of electrical properties, by considering its thickness.

For a bilayer sample, by adapting the models proposed by Peritz[57] and Baron[58] we obtain a relation for RH_s and R_s that depend on the properties of the two layers:

$$RH_s = \frac{RH_{s,1}/R_{s,1}^2 + RH_{s,2}/R_{s,2}^2}{\left(1/R_{s,1} + 1/R_{s,2}\right)^2} \quad 3.21$$

$$\frac{1}{R_s} = \frac{1}{R_{s,1}} + \frac{1}{R_{s,2}} \quad 3.22$$

By performing a van der Pauw-Hall measurement on a non-laser processed sample (as-grown sample) we obtain its $RH_{s,a.g.}$ and $R_{s,a.g.}$ values.

The processed sample is divided into two layers. The upper layer, layer 1, has unknown electrical properties arising from the laser process, and a thickness defined as the maximum melt depth, obtained through SIMS measurements. The layer underneath, layer 2, is considered equivalent to the non-processed sample in terms of electrical properties, with its thickness corrected by subtracting the maximum melt depth from the as grown layer thickness.

We can thus obtain the values of the $R_{s,2}$ and $RH_{s,2}$ from the non-processed sample:

$$RH_{s,2} = RH_{s,a.g.}\frac{d}{d_2} \quad 3.23$$

$$R_{s,2} = R_{s,a.g.} \frac{d}{d2} \qquad 3.24$$

By applying the bilayer model on the RH_s and R_s values obtained for a processed sample we can extract the $RH_{s,1}$ and $R_{s,1}$:

$$RH_{s,1} = \frac{\frac{RH_s}{{R_s}^2} - \frac{RH_{s,2}}{{R_{s,2}}^2}}{\left(\frac{1}{R_s} - \frac{1}{R_{s,2}}\right)^2} \qquad 3.25$$

$$R_{s,1} = \frac{1}{\left(\frac{1}{R_s} - \frac{1}{R_{s,2}}\right)} \qquad 3.26$$

The model allows to separate the electrical contributions for the two layers. Thanks to the sheet resistance and Hall coefficient for the first layer we can calculate the resistivity, active carrier concentration and mobility of the annealed region thanks to the formulas introduced previously. An assumption that the active dopant profile is the same throughout the entire 1st layer is made, so that the properties of this layer are the fixed inside the MMD thickness.

The experimental setup used for the electrical characterization is a four-points probe device with spring-loaded golden tips that are aligned on the corners of the samples. In order to perform the Hall measurements, the device is put inside a permanent magnet, with a field B = 0.625T. RH_s and R_s are given as response by the instrument thanks to a custom-made program that not only allows for visualization of the results but also permits to control the experimental parameters. The input current can be set in a broad range of values (10^{-5} to 10^{-2}A), and the maximum detected potential saturates at 20V. Highly doped samples should produce ohmic contacts, as such the I-V curve should be as linear as possible and high potentials are not produced. Usually, a high potential on some terminal indicates a bad contact and a new landing must be done. On the other hand, obtaining an ohmic contact with lowly doped samples is usually more difficult as they tend to be non-ohmic. A short burst of current can be applied on the surface of the sample to break the natural oxide which acts as a dielectric and is a hindrance to the formation of a good electrical contact with the tips. The program also allows the utilization of a geometrical correction factor that can be used to account for the finite size of the tips and the fact that, depending on the sample size and shape, the tips could be placed at some distance from the perimeter of the sample[59].

The instrument comes with various sets of tips. The set used for the characterization of the samples is made of four golden tips with a square configuration in a ~4x4 mm^2 size.

The samples were cut through a dicing machine by aligning the edge of the blade with the borders of the laser spots, to match size and shape of the laser processed regions. The blade is used to electrically separate the processed spots by making 150 µm deep cuts. The single spots were then separated manually when needed.

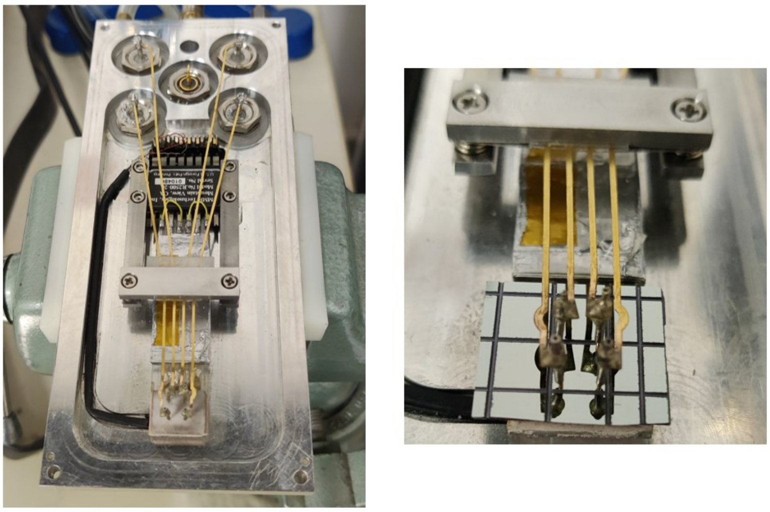

Figure 3.11: Instrument used for the Van der Pauw-Hall measurements. A close up on the four tips placed on a sample is provided on the right.

3.3.5 Scanning Microwave microscopy

Among the electric AFM modes allowed by the Flex-AFM instrument, the Scanning Microwave Microscopy (SMM) is a novel probe technique that is able to probe the electric properties of the samples and yield a contrast depending on properties such as resistivity and capacitance. The technique is able to detect variations in electric properties across a sample and is mainly used in failure analysis in the semiconductor industry, where it allows for a fast identification of specific regions of a device (like p-n junctions, metal contacts and the gate region).

The working principle of the technique is based on the interaction between EM waves and matter in the microwave regime. A microwave signal is generated by an RF generator and sent through a transmission line down to the metallic tip of an AFM or STM tip. Here the electromagnetic wave interacts with the sample, where its partly reflected and partly absorbed. The reflected wave travels back into the transmission line and is compared to the reference signal, to calculate their ratio as the output of the measurement.

Modern SMM systems work in the small antenna, near-field regime. To achieve the small antenna regime it's necessary that that the antenna that releases the microwave onto the sample (the AFM tip in our case) is much smaller than the wavelength of the electromagnetic wave. To work in the near-field regime the distance between the source of the electromagnetic wave, AFM tip, and receiver of the wave, the sample, should be much shorter than the wavelength of the wave. These conditions are easily met in the case of the microwaves released by an AFM tip, considering the apex of the tip to be 50nm or less and the distance with the sample to be usually in the order of the nanometres or smaller. More specifically, the technique works in the evanescent wave regime where the electromagnetic wave has a static behaviour in the proximity of the antenna and has an exponential decay depending on the distance while maintaining its characteristic time dependent oscillation. The electromagnetic wave possesses an imaginary wavenumber in this regime and can store reactive energy in the vicinity of the tip, thanks to its static behaviour. The interaction with a sample modifies the magnitude of this energy and the variation is detected by the electronics of the instrument.

The interaction between the sample and the tip is usually described thanks to the lumped element model[60].

Since the microwave has an evanescent behaviour around the antenna, and the tip is visualized as a reactance by the detection system. Both the tip and the sample can have a lossy component, and a resistive part is added to the net impedance. The general formula of the impedance at the tip is given by:

$$Z_t = R_t + iX_t \tag{3.27}$$

Impedance is the alternated current/potential equivalent of the resistance, and it's made up of a resistive contribution (real part, R_t) and the reactance contribution (imaginary part, X_t). The tip impedance is influenced by both the electrodynamic properties of the sample and the tip properties, the distance between tip and sample also plays a role on the as the intensity of the wave decreases exponentially with distance. While the reactance contribution is always present, as it arises from the effect of the alternating voltage from the microwave oscillation (and every material has some extent of reaction to it), the resistance contribution is present only in lossy materials (ie. Loss for joule effect, absorbative dissipation of electric and magnetic field, and could be ignored for non-lossy materials like dielectric ones).

The complex Poynting theorem yields the following expression for the reactance of the near-field tip:

$$X_t = \frac{4\omega}{|I_i|^2}\int_V (w_m w_e)\, d^3x \tag{3.28}$$

where I_i is the harmonic input current at the tip terminals, $w_m = B \cdot H^*/4$ and $w_e = E \cdot D^*/4$ are the magnetic and electric energy densities, respectively. The volume considered inside the integral is usually the probing volume of the technique, that depends on the tip size and skin-depth of the microwave inside the sample.

Depending on the dominant type of reactive energy stored in this field the tip can act as an electrical or magnetic entity. For the materials of interest, mostly semiconductors and dielectrics, and considering the near-filed approximation, the interaction is mostly electrical in nature and the magnetic contribution can be ignored.

For what concerns the real part of the tip impedance R_t, this is given by:

$$R_t = \frac{\omega}{|I_i|^2} \int_V (\frac{\sigma}{\omega}|E|^2 + \varepsilon_0 \varepsilon''|E|^2 + \mu_0 \mu''|H|^2)\, d^3x \qquad 3.29$$

As introduced before, the resistive part of the impedance can be given several dissipation processes like Joule heating and dissipation of electric and magnetic energy by excitation of dipoles or magnetic interactions.

The impedance Z_t of an electric tip can be represented as a network of the tip-to-sample coupling capacitance $1/C_c = 1/C_{c,1} + 1/C_{c,2}$, the sample "near-field" impedance Z_s, and the tip stray capacitance C_{str}

$$(Z_t)^{-1} = \left(\frac{1}{i\omega C_c} + Z_s\right) + i\omega C_{str} \qquad 3.30$$

With C_c being the coupled capacity of tip and sample, and C_{str} is a general term that accounts for the so-called stray capacities. The stray capacity is produced by the fact that a real tip can't be described by a perfectly sharp apex and, while the microwave is released mainly the apex, thanks to gauss theorem, the reflected signal can interact with the sides of the tip and cantilever, adding other capacity contributions to the total measured impedance.

The total reflection coefficient, Γ, is given by the following relation:

$$\Gamma = |\Gamma| e^{(i\theta)} = \frac{Z_t - Z_0}{Z_t + Z_0} \qquad 3.31$$

Where Z_t is the tip-sample complex impedance and Z_0 is the circuit refence impedance.

The reflection coefficient is usually called S_{11} and, as introduced before, is the response of the instrument. Since the impedance is a complex parameter, the S_{11} is also a complex number. Considering the general formula of the impedance, where the reactance is solely capacitive:

$$Z = R + \frac{1}{i\omega C} \qquad 3.32$$

The S_{11} parameter can be visualized, in both complex notation and polar one:

$$S_{11} = Re(S_{11}) + i \cdot Im(S_{11}) \qquad 3.33$$

$$S_{11} = |S_{11}| e^{i\varphi_{S11}} \qquad 3.34$$

The S_{11} parameter depends on the impedance of the tip-sample system and is turn modulated by the electrical properties of the sample, resistance R and capacitance C.

The S_{11} scanning mode is the main SMM measurement mode. A radio frequency generator produces a microwave, with a frequency in the range of 1-6 GHz. The radio wave travels through the transmission line up to the AFM metallic tip, where it interacts with the sample in the near-field regime, and it's partly reflected and absorbed proportionally to its electrical properties. The transmission line is the entire assembly of the electrical components necessary to direct the microwave to the tip and it includes the RF generation and detection circuitry (a vector network analyser, VNA, placed outside of the AFM assembly), a microwave low loss coaxial cable, a 25 Ω mismatch cable, connected to the cantilever through its holder stage. The microwave is reflected at the tip-sample interface and travels back through the same transmission line and is detected by the analyser through the same port as the input one, hence the name S_{11} where the first number stands for the input port and the second for the output port. The tip is scanned on the sample's surface and the S_{11}value is recorder for each pixel.

Since the impedance of the tip-sample system is much higher than the 50 Ω impedance of the transmission line, an impedance matching circuit modifies the power of the microwave in order to nearly match the two impedances, to obtain the best sensitivity for the variation of the signal. Experimentally the best matching condition is obtained by doing a frequency sweep with the tip in contact with the sample. Several matching conditions are identified through the observation of maxima and minima in the sweep spectrum, arising from the internal reflections at the terminals of the instrument and the transmission line components that behave as resonator cavities. The best matching condition is found at the lowest minimum, where the maximum energy is transferred into the sample and the reflection is at its lowest, in this condition the instrument is the most sensitive to small changes in the S_{11} parameter.

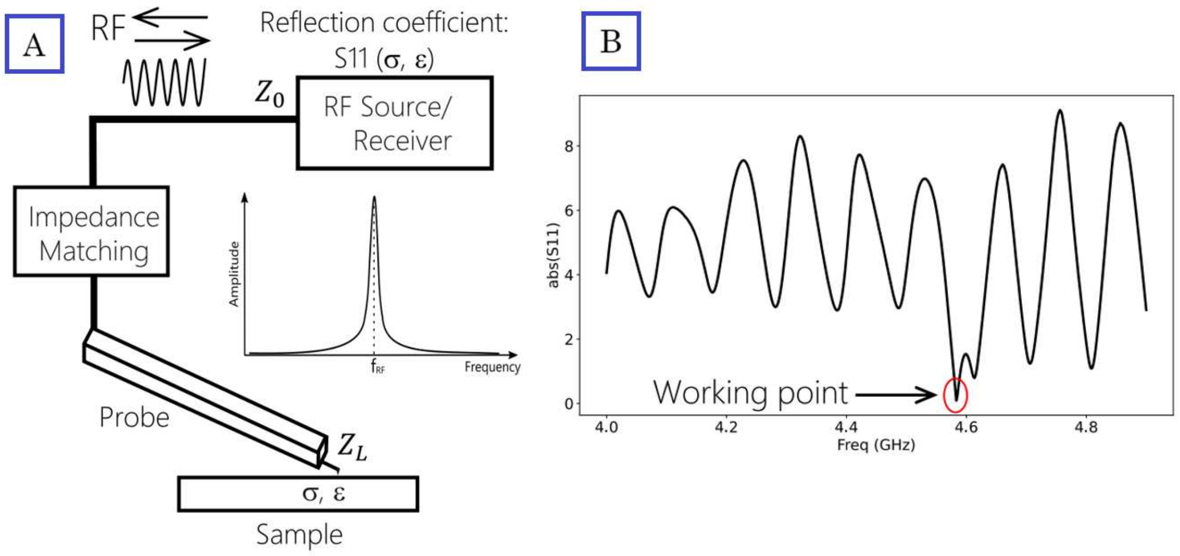

Figure 3.7: Representation of an S_{11} mode experiment, (A). Resonance of the S_{11} parameter in a frequency sweep, (B). Images provided by Nanosurf

In order to extract the tip-sample impedance form the S_{11} measurement a calibration procedure is required. The calibration necessity stems from the fact that the reflection produced at the tip-sample interface is not the only reflection that occurs inside the transmission line, wherever a physical interface is introduced between physical components a reflection point is generated. This observation explains why the S_{11}, the reflection parameter, has to be corrected to account for these variations. A calibration technique derived from VNA black-box calibration procedure has been proposed[61] This calibration workflow allows for the correction of the main sources of reflection inside the transmission line by obtaining three experimental values of the S_{11} values on three points of known electrical properties before performing an SMM measurement on an unknown sample. The three experimental S_{11} parameters obtained can be input into an algorithm, together with their respective theoretical tip impedances, to find to solve a system of equations and find the error parameters to correct the internal reflections. The algorithm consists in a system of equations:

$$S_{11m} = e_{00} + \frac{e_{01}S_{11}}{1 - e_{11}S_{11}} \tag{3.35}$$

$$\begin{pmatrix} 1 & S_{11}^1 & S_{11}^1 S_{11m}^1 \\ 1 & S_{11}^2 & S_{11}^2 S_{11m}^2 \\ 1 & S_{11}^3 & S_{11}^3 S_{11m}^3 \end{pmatrix} \begin{pmatrix} e_{00} \\ e_{01}^* \\ e_{00} \end{pmatrix} = \begin{pmatrix} S_{11m}^1 \\ S_{11m}^2 \\ S_{11m}^3 \end{pmatrix} \tag{3.36}$$

$$e_{01} = e_{01}^* + e_{00}e_{11} \tag{3.37}$$

Where S_{11m} is the measured, uncalibrated, value for each point. The error parameters e_{00}, e_{01} and e_{11} are given by solving the system of equations. And the $S_{11}$are calculated by the specific model that describes the sample properties.

When a semiconductor material is probed with an SMM technique the contact between the metallic tip and the sample can be considered as a metal-oxide-semiconductor (MOS) junction, considering the presence of the natural oxide between tip and sample. The tip-sample lumped impedance can be described as two capacitors in series, one made up by tip and oxide layer, and the other made by the depletion capacitance of the semiconductor material.

The tip-oxide capacitance can be expressed as:

$$C_i = 2\pi\varepsilon_0 R ln\left[1 + \frac{R(1 - sin\theta)}{z + h/\varepsilon_i}\right] \quad 3.38$$

Where R is the tip apex radius, θ is the tip curvature angle, z is between the tip and the sample and h the oxide thickness. ε_i is the dielectric constant of the oxide.

The capacitance of the semiconductor sample can be calculated by using the theory from the MOS junction, the junction induces the formation of a depletion region in the semiconductor characterized by its depletion capacitance:

$$C_{dep} = \pi R^2 \sqrt{\frac{\varepsilon_0 \varepsilon_r n e^2}{k_B T}} \quad 3.39$$

The lumped tip-sample impedance is given by:

$$C_{tip} = \frac{C_{dep} C_i}{C_{dep} + C_i} \quad 3.40$$

And the impedance can be calculated from equation 3.10 by putting the resistance part equal to zero (a safe approximation for doped samples with low resistivity).

$$Z_{tip} = \frac{1}{i\omega C_{tip}} \quad 3.41$$

After the impedance of the tip is calculated, the theoretical S_{11} values can be input into the algorithm to obtain the three error parameters.

The reverse of the first formula from the algorithm can be used to obtain the calibrated S_{11} values for an unknown sample, and subsequently calculate the tip-sample impedance:

$$S_{11} = \frac{S_{11m} - e_{00}}{e_{01} + e_{11}(S_{11m} - e_{00})} \quad 3.42$$

$$Z_{tip} = Z_0 \frac{1 + S_{11}}{1 - S_{11}} \quad 3.43$$

This calibration procedure can be used only if the characteristics of the tip and the thickness of the oxide are known, in order to calculate their theoretical impedance[62].

From the lumped tip-sample impedance, the capacitance of the sample can be extracted by reversing formula 3.40 and the carrier concentration can be calculated by using the inverse of formula 3.39.

The SMM measurements were conducted in contact mode with a 25PtIr300G tip, with a nominal tip size < 20 nm, specifically designed by Rocky Mountain Nanotechnologies for SMM measurements.

Chapter 4

Experimental results and discussion

In this chapter the experimental results, are presented. The objective of the thesis was to study the behaviour of phosphorous dopant activation in Germanium thanks to Pulsed Laser Melting. The laser anneal processes are able to activate the dopant to higher concentrations in comparison to standard equilibrium processes, even surpassing the solid solubility limits, at the cost of a higher thermal instability, given the extreme out of equilibrium conditions of the samples after the laser process. Considering the collaboration with L-NESS at Politecnico di Milano for the possible applications of the samples, the quality of the surface and thermal stability (of prime importance for a successive growth stage) and the high activation (necessary for effective IR reflectivity) were the most important characteristics to control. For this reason, a thermal stability study has been conducted in order to evaluate the deactivation of the dopant produced by an increase in temperature, while Raman, AFM and SIMS experiments have been performed to characterize the morphological and chemical properties of the samples. The electrical properties of the samples were estimated by the means of Van der Pauw-Hall characterization and compared to IR reflectivity results obtained by the research group at L-NESS.

4.1 Laser processes and samples overview

Several samples have been produced starting from the wafers provided by PoliMi.

The first laser processes were performed on two of the four total wafers, to study the effect of the laser energy density on both activation of the samples and their structural properties. This allowed us to identify the best process condition for further investigations.

The next step of the thesis was to add samples from the other two wafers in order to investigate the effects of the laser process on samples of different composition and growth conditions.

Samples from the four wafers, processed at the optimal energy, have been subsequently subjected to a thermal stability study to identify the maximum working temperatures for the successive growth step at PoliMi.

The four wafers used during the thesis are characterized by different chemical and structural properties as well as different growth temperatures.
The main characteristics of the samples are reported in the following table.

Wafer number	Composition	Layer thickness (μm)	Growth temperature (°C)	P chemical concentration (cm^{-3})	Active concentration (cm^{-3})
11239	$Si_{0.15}Ge_{0.85}$:P	1.6	550	1.1E20	1E19
11238	Ge:P	1.8	500	1.3E20	2E19
9547	Ge:P	0.6	460	1.1E20	2E19
10258	Ge:P	0.5	350	3.5E20	4E18

Table 4.1: Summary of the sample's properties. Chemical concentration and layer thickness are calculated by SIMS measurements, active concentration is obtained by VdP-Hall measurement.

During the first laser process two pieces from the 11238 and 11239 wafers were selected, in order to obtain a first set of samples for both germanium and silicon-germanium alloy.

The first step was the cleaning procedure reported in chapter 3.2. A series of baths in acetone, water and iso-propyl alcohol were used to remove any dust or organic matter that could be deposited on the samples. The wafers were covered by a protective polymer layer that was removed following the same procedure, since the polymer was soluble in acetone. Moreover, the natural oxide layers were removed thanks to HF baths for the samples just before the laser processes, in order to avoid any variation of laser energy absorption produced by the presence of the oxide, and reduce the in-diffusion of oxygen during the PLM processes.

The clean wafer pieces were then laser processed thanks to single pulses irradiation on different spots with varying laser energy densities. For both the wafer pieces 8 samples were studied, 7 processed with energy increasing form 300 mJ/cm^2 up to 900 with a 100 mJ increment, and one non-processed sample (as grown) to use as reference.

A second process run was performed on pieces of wafers from the remaining two wafers, 10258 and 9547, both of Ge:P on Si, with energy densities from 500 to 900 mJ/cm^2, in order to study the effects of the laser on Ge:P with different properties and chemical concentrations.

The third process run was performed on pieces coming from the three Ge:P wafers and the SiGe:P waver, selecting the best PLM conditions selected by the above process runs. The thermal stability of these samples was evaluated. In this case the Ge:P samples coming from wafers 11238, 10258 and 9547 were processed at 900 mJ/cm^2. The SiGe:P sample processed at 500 mJ/cm^2, in the first run, was also used for the stability test. For all the samples, reference, non-processed samples have also been subjected to stability tests.

A resume of the three process runs is reported in the following table

Process run	Wafer	Composition	ED (mJ/cm^2)
First	11239	$Si_{0.15}Ge_{0.85}$:P	300-900
First	11238	Ge:P	300-900
Second	10258	Ge:P	500-900
Second	9547	Ge:P	500-900
Third	11238	Ge:P	900
Third	10258	Ge:P	900
Third	9547	Ge:P	900

Table 4.2: Main samples produced during the thesis, divided by process run and specifying the energy range for the laser process

The reference as grown samples, were obtained during the electrical separation of the lasered spots, as introduced in chapter 3.3.3, thanks a dicing machine that allows to separate the single spots.

4.2 SIMS measurements

The SIMS measurements were performed in order to acquire chemical, quantitative information from the samples. The main properties that were looked for in the samples were the chemical concentration of the dopants, their distribution profile throughout the depth of the grown layer and how the laser process affected these properties depending on the energy density of the laser pulse.

As introduced in the previous chapter, samples from the four wafers have been produced and investigated thanks to the first two process runs. The SIMS measurements were performed first on the samples from the 11238 Ge:P wafer and 11239 SiGe:P wafer. For the Ge:P samples, depth vs. chemical concentration profiles of the P dopant have been acquired. For SiGe:P the three main elements (Ge, Si and P) have been characterized in order to get a clear idea of the alloy composition. The profiles for each energy density and the as grown material are shown, in order to visualize the effect of the laser process on the redistribution of chemical species and its dependence on the ED of the impinging laser pulse, Fig. 4.1.

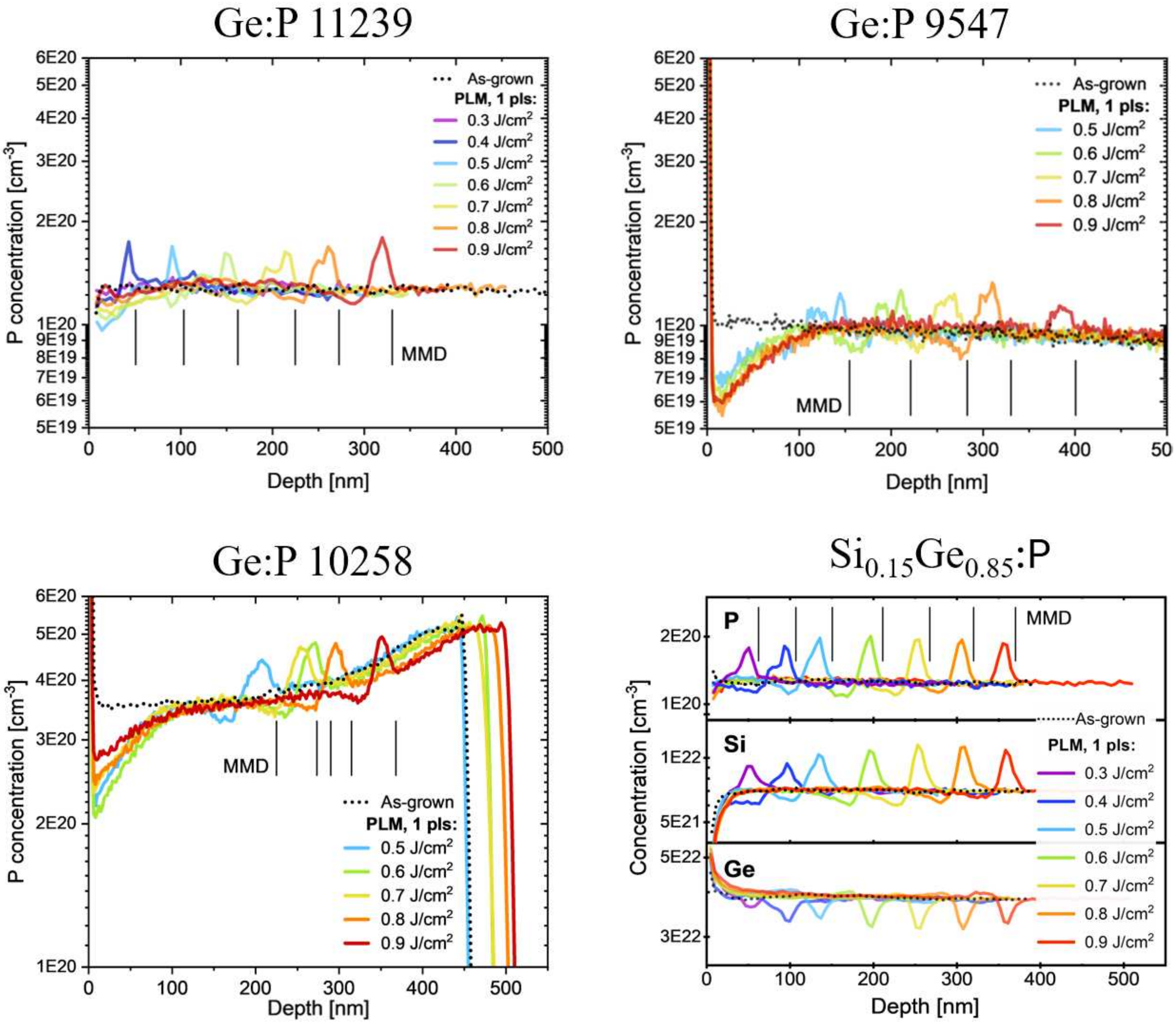

Figure 4.1: The SIMS profiles extracted for each energy density on the four wafers are shown, up to the highest MMD.

The first nanometres of the profiles show an incorrect behaviour of the dopant's concentrations, this phenomenon is explained by the so-called transient effect of the SIMS measurements. An error in the estimation of chemical concentrations is produced at the start of the sputtering process, since it's still not at equilibrium, and the intensity of secondary ion beam produced from the atom's extraction is unstable.

The SIMS measurements allowed us to identify the maximum melt depths for all the samples with varying energy density. This possibility is given by the fact that the fast recrystallization, subsequent to the melting that occurs during the PLM process, is characterized by dopant pile up observed in the SIMS profiles[26]. Since the solubility of the dopants, and their diffusivity, is much higher in the liquid phase, they find themselves trapped at the interface with the solid phase when the melting stops at the maximum melt depth, before starting to recrystallize. The 11238 wafer lasered at 300 mJ/cm^{-2} shows no accumulation peaks, and the MMD cannot be calculated. At this energy only a partial localized melting occurs, as also supported by AFM characterization as will be shown later. For the SiGe:P wafer the melting starts at or below 300 mJ/cm^{-2} since the pile-up is observed for all energies.

As already demonstrated form literature and previous experience with the PLM process[63][31], the maximum melt depths show a linear dependence with the laser energy density, Fig 4.2. The estimated MMD was calculated at the end of the accumulation peaks. Considering that the recrystallization starts from the bulk of the material to the surface, using these values gives the best estimation of the depth at which the molten layer stops traveling toward the inner part of the material.

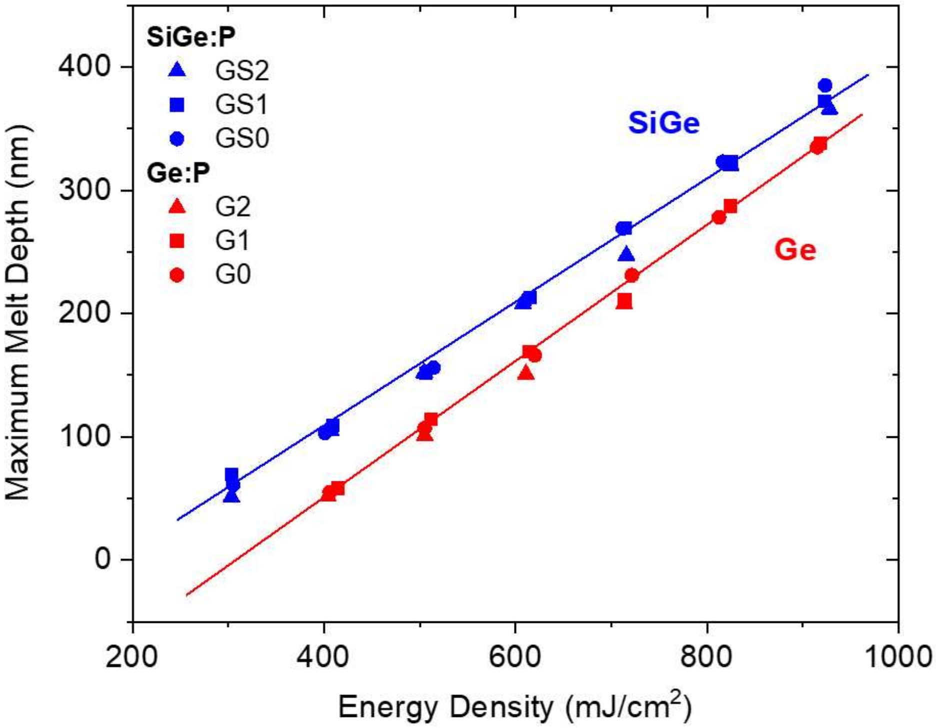

Figure 4.2: A plot of the maximum melt depth vs. energy density shows a good linearity for both Ge:P samples and SiGe:P samples, with little variations between different samples processed for each same energy density.

The SIMS measurement also allows to visualize the depth profile of the dopant. For all the samples we see that the dopant distribution at varying energy densities doesn't show severe variations form the unprocessed samples, apart from the accumulation peak, and a P out diffusion with 100 nm close to the surface. The profiles are quite flat, as expected for CVD grown samples, showing good homogeneity of atom incorporation during the growth.

SIMS measurements have also been conducted to estimate the total layer thickness for the wafers, necessary for electrical properties interpretation.

In figure 4.3, on the right, the thickness of the Ge:P wafers 10258 and 9547 were estimated thanks to the sudden drop of dopant concentration at the interface between the grown layer and the silicon substrate.

For wafers 11238 and 11239, profiles of the three main species have been produced to also evaluate the relative concentration of silicon and germanium.

The Ge:P layers contain a low concentration of silicon, circa 1%. The alloy has been calculated to be composed of 85 % germanium and 15 % silicon. An interesting characteristic of the SiGe:P samples, visible in both fig. 4.1 and 4.3 is that the accumulation peaks after the laser process are also visible for the silicon profile, with a depletion of the main matrix atom, germanium, at the MMD.

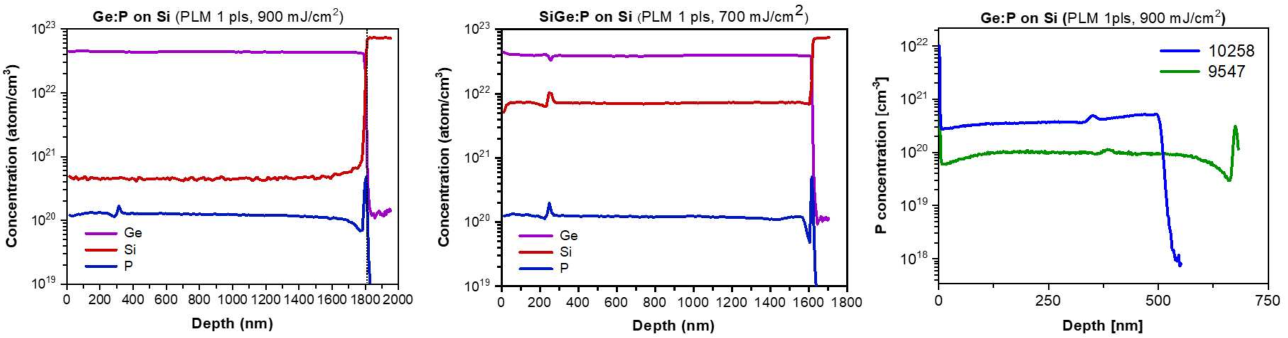

Figure 4.3: SIMS profiles to extract grown layer thickness of the four wafers: on the left and centre samples 11238 and 11239, respectively are shown. On the right the two reaming samples' profiles are placed in the same graph.

The chemical concentration of the dopant and the layers thickness in the four wafers has already been reported in table 4.1. As already introduced in chapter 3.1, the chemical concentration of the dopant has been calculated thanks to the use of a standard sample that allows for the calculation of the relative sensitivity factor (RSF) for the species under study in the Ge:P samples.

For the SiGe:P analysis, the calculted chemical concentrations may be affected by an error, since a doped reference sample of the same composition was not available.

Wafer	300	400	500	600	700	800	900
Ge:P 11238	No melt	58	114	169	211	287	338
Ge:P 10258	No melt	/	217	280	268	304	359
Ge:P 9547	No melt	/	150	214	278	319	398
SiGe:P 11239	61	103	156	210	269	323	385

Table 4.3: Maximum Melt Depth for each ED, for the four wafers. The 10258 and 9547 were processed in the 500-900 mJ/cm^2 range.

4.3 Raman characterization

Raman spectroscopy has been performed on both the processed and unprocessed samples, to identify structural variations induced by the laser process.

The main focus of the Raman spectroscopy for our samples has been placed in the study of the main Ge-Ge Raman active mode that falls at Raman shift ~300 cm^{-1}. This peak is produced by the excitation of Ge-Ge Transversal Optical (TO) mode. Being this the most intense signal for crystalline germanium, the variation of its shape and position can be used to infer information on the lattice strain state or alloying conditions.

As already introduced in chapter 3.3.2, the Raman characterization probes the first 60 nm, at most, of the doped germanium layers, making this technique useful to analyse the surface properties for the samples.

Raman spectra have been acquired for samples belonging to the four wafers and for each laser energy density, along with the unprocessed reference samples.

A subset of the spectra will be shown.

The most significant spectra obtained for the samples coming from wafer 10258 are shown (fig. 4.4), considering that samples from this wafer have shown the largest variations in comparison to bulk pure germanium.

For the SiGe:P wafer some significative spectra are also reported. To have a complete image of the full Raman characterizations, for each energy density and wafer, a summary of the TO peak position is shown on a graph and the strain is evaluated. The error is set to the instrumental resolution of ±0.25 cm^{-1} with the 638 nm source and 1800 gr/mm diffraction grating combination.

The Raman analysis on Ge:P samples belonging to wafers 11238 and 9547 show a slight blueshift of less than 1 cm^{-1} for Ge-Ge peak in comparison to the bulk reference sample and no strong correlation to the varying energy density is observed. This blue shift is attributed to a slight tensile strain produced by the thermal expansion mismatch between silicon and germanium that comes into play during the cool down after the laser process[54]. This effect seems to be slightly enhanced by the fast laser process, in comparison to the cool down after the LEPECVD growth, where a slight shift is already present, as can be seen in the unprocessed samples, fig.4.4.

The samples belonging to the 10258 wafer, grown at lower temperature and showing a higher chemical concentration of dopants, show a different behaviour. The unprocessed sample shows an evident red-shift of the Ge-Ge phonon mode, showing that, due to the lower temperature growth, the layer is still affected by the compressive strain produced by the growth on the silicon substrate, also supported by the observation that this wafer exhibits the thinnest grown layer. After the laser process, the strain turns into a tensile one like the other wafers, but to a higher degree, which can be explained by an enhancement of the strain relaxation due to residual defect after low temperature. The higher concentration of phosphorous atoms in the matrix of this wafer might also contribute to the higher strain.

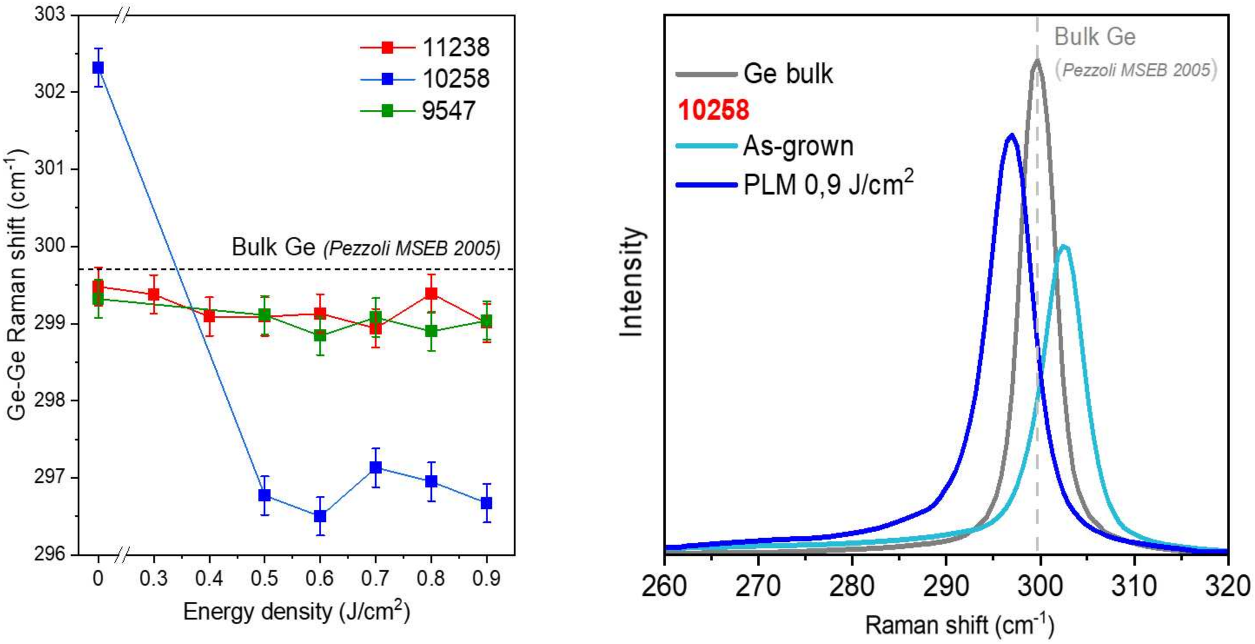

Figure 4.4: Summary of the Ge-Ge TO peak position vs. ED for the three Ge:P wafers, on the right. On the left, the 10258 Raman peak of the unprocessed sample is compared with a bulk reference germanium and a lasered one, showing a noticeable difference between the unprocessed and processed samples.

The SiGe:P sample shows a slight redshift on the as grown samples and up to 600 mJ/cm^2, after this energy a blueshift indicating tensile strain is observed like in the processed samples from the other wafers.

The compressive strain observed on the as grown sample, and at lower energies, is probably induced by the relatively high concentration of silicon in the matrix which reduces the strain relaxation.

At higher energies, when the molten layer grows thicker, the thermal expansion mismatch contribution is visible, and the tensile strain is produced during the cooling.

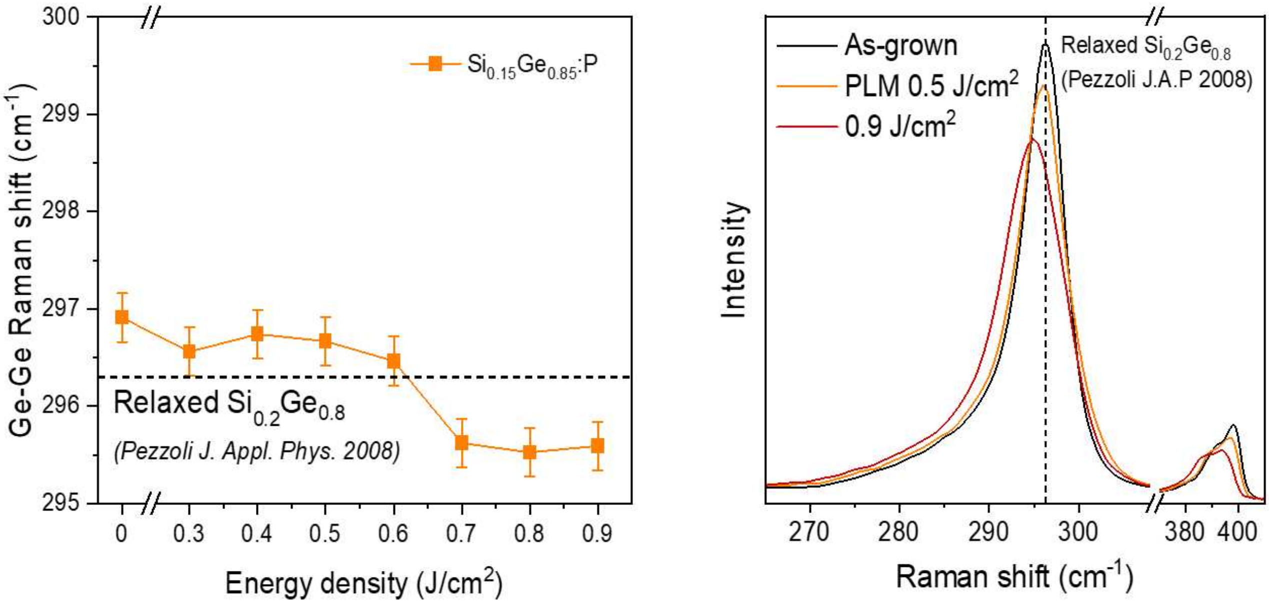

Figure 4.5: Summary of the Ge-Ge TO peak position vs. ED for the SiGe:P wafer, on the right. On the left, the Raman peak of the unprocessed sample is compared with a bulk reference germanium and a lasered one

The correlation between the TO Raman mode shift and the strain is done by using the so-called phonon strain shift coefficients, K (cm^{-1}), that allows to calculate the biaxial strain present on the investigated region thanks to the following formula:

$$\varepsilon_{\parallel} = \frac{\Delta\omega}{K} \qquad 4.1$$

Which states that the biaxial strain can be calculated from the ratio between the phonon shift, in cm^{-1}, and the phonon strain shift coefficient. A positive shift indicates a compressive strain while a negative one a tensile one.

The reference value for the relaxed bulk germanium TO Raman mode has been sourced from Pezzoli et al., 2005[64], while the phonon strain shift coefficients, along the reference value for the TO Raman shift position of the SiGe alloy come from [65]. The values calculated for a $Si_{0.18}Ge_{0.82}$ alloy have been used, as it was the closest composition to our $Si_{0.15}Ge_{0.85}$ alloy.

The highest tensile strain is observed for the 10258 wafer at 0.7%, a summary of the calculated strain is reported in the table below, where the strain is reported for each wafer and energy density.

Wafer	As grown	300 mJ/cm^2	400 mJ/cm^2	500 mJ/cm^2	600 mJ/cm^2	700 mJ/cm^2	800 mJ/cm^2	900 mJ/cm^2
Ge:P 11238	+0.05%	+0.07%	+0.14%	+0.15%	+0.13%	+0.17%	+0.07%	+0.16%
Ge:P 10258	-0.60%	/	/	+0.67%	+0.73%	+0.58%	+0.62%	+0.69%
Ge:P 9547	+0.09%	/	/	+0.13%	+0.19%	+0.14%	+0.18%	+0.15%
SiGe:P 11239	-0.13%	-0.06%	-0.1% C	-0.08%	-0.03%	+0.15%	+0.17%	+0.15%

Table 4.4: Summary of the stresses calculated through Raman spectroscopy for all the samples, shown in percentage (positive values identify a tensile strain while negative a compressive one).

4.4 AFM measurements

To further investigate the surface of the samples, both un-processed and processed, AFM images for each energy density and wafer have been acquired.

The first images have been acquired for the samples coming from Ge:P 11238 wafer and the SiGe:P wafer. After the first evaluations on the surface quality, the best conditions for the subsequent laser processes were identified.

Samples from the other two Ge:P wafers were processed, and their surface was characterized after processing in the identified energy range.

The following images have been acquired in semi-contact mode, which has a high sensitivity to surface features variation without the need of working with the tip in contact with the sample for the entire scan, reducing surface and tip damage.

The surface of an unprocessed 11238 Ge:P sample is reported in figure 4.6, in order to identify the starting conditions of the surface after the LEPECVD growth.

The AFM characterization of the as grown samples shows a good surface quality, characterized by 2~3 μm deep ripples and with a 0.5 μm period. Some hills are also present with a height of ~ 20 nm and 2~3 μm diameter.

The ripples are also reproduced on the hills and with the same characteristics as the ripples on the surface. These ripples are usually produced by strain relaxation and the island formation is a competitive mechanism for the process[66]

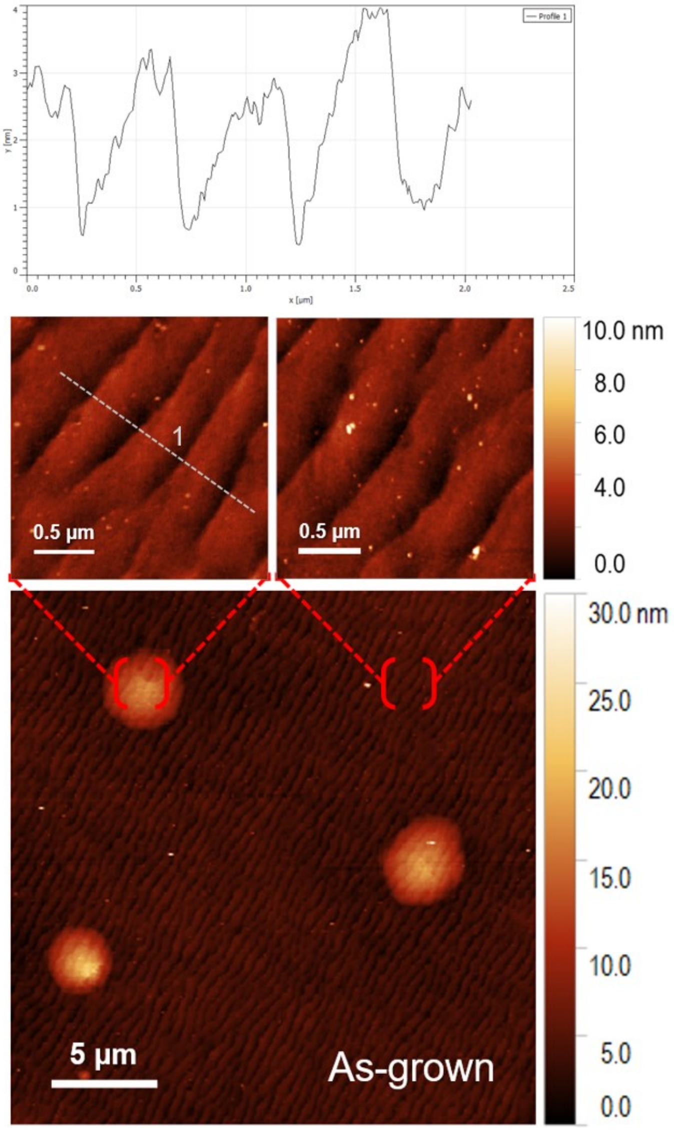

Figure 4.6: AFM image of the 11238 non processed samples. Zooms on the surface and hills are shown. The profile of the surface ripples is extracted in the uppermost part.

Figure 4.7 allows to visualize the effect of the laser energy on the surface quality, for wafer 11238. At 300 mJ/cm^2 we observe the formation of pyramidal structures, correlated to a localized surface melting at the melting threshold [31], meaning that this laser energy is not enough to produce a complete melted layer. This observation is also supported by the SIMS profiles that don't show any dopant pile-up at this energy, as discussed in chapter 4.2.

Moreover, in the 300-400 mJ/cm^2 we see a spike of the average roughness, correlated to the incomplete melting.

With increasing energy density, the hills increase in number and decrease in size up to 600 mJ/cm^2, after this energy they start to decrease in number and increase in size. At 900 mJ/cm^2 the surface quality is again quite good; the hills are flattened, and the ripples are similar the unprocessed sample. The average roughness of the sample is also reduced with increasing ED.

The AFM investigation has also underlined an interesting characteristic of the PLM process, which is the ability to preserve the morphological features of the material even after a melting phase, as demonstrated by the recovery of the surface feature at the higher laser energies.

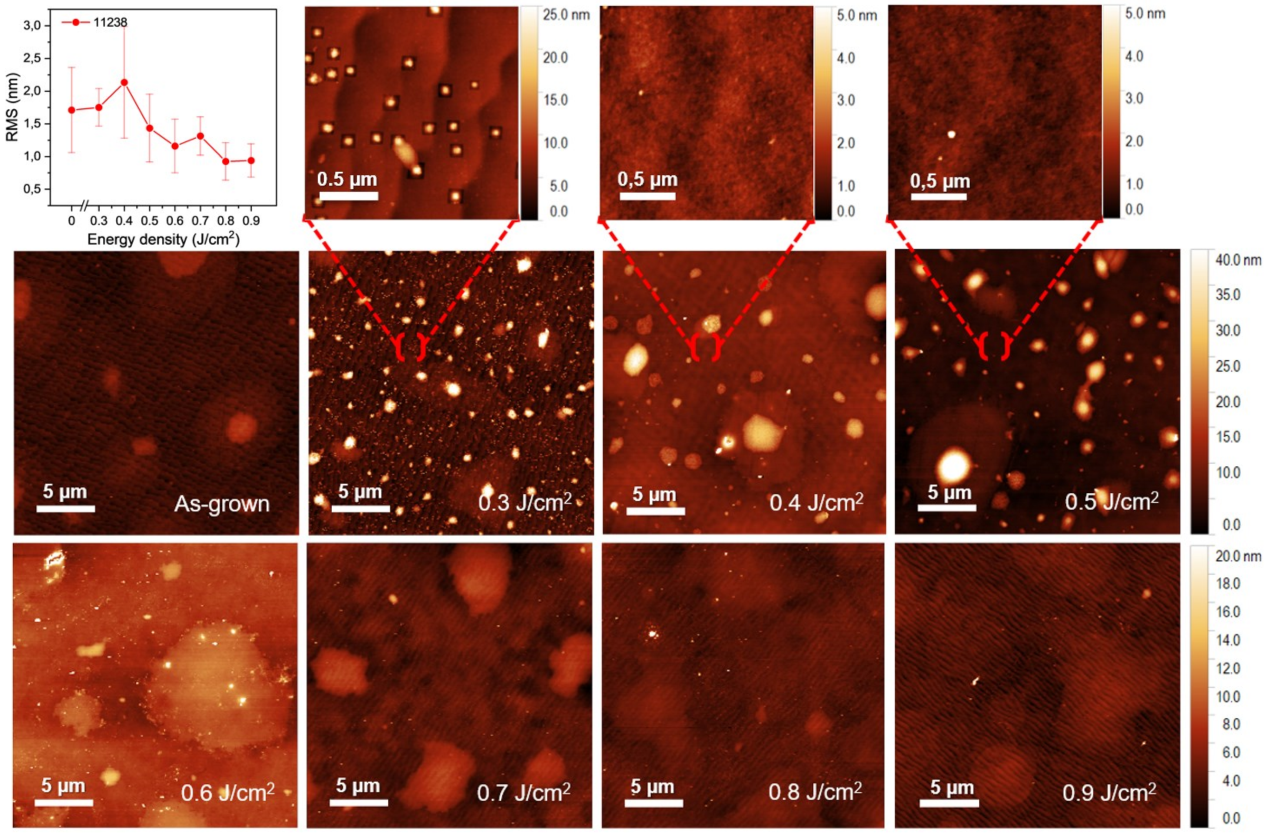

Figure 4.7: AFM images of the 11238 samples for each energy density acquired on 20x20 µm^2 area. The zooms on the images for the samples at low energy density show a variation of average surface roughness and features' shape. An inset above the as grown sample image, shows an average roughness vs. ED plot

The Ge:P samples of the second process run, namely those belonging to the 10258 and 9547 wafer, have also been subjected to a complete AFM investigation for each energy density, in this case in the range of 500-900 mJ/cm^2, since the melting at lower energies might be incomplete.

The surface of the 9547 samples shows a different morphology in comparison to the 11238 samples. In the middle of the energy range, a strong undulation can be noticed, that is then reduced at the highest energies, figure 4.8. Though morphologically different, the strain calculated on the 9547 wafer and shown in figure 4.4 in chapter 4.3, closely follows the behaviour of the wafer 11238.
2x2 µm zooms, on the lower part of the image, show a flat surface on the small scale, between the surface features present on a larger scale, this suggest that the 9547 samples relax in a different way in comparison to the 11238 samples but reach a similar strain level.

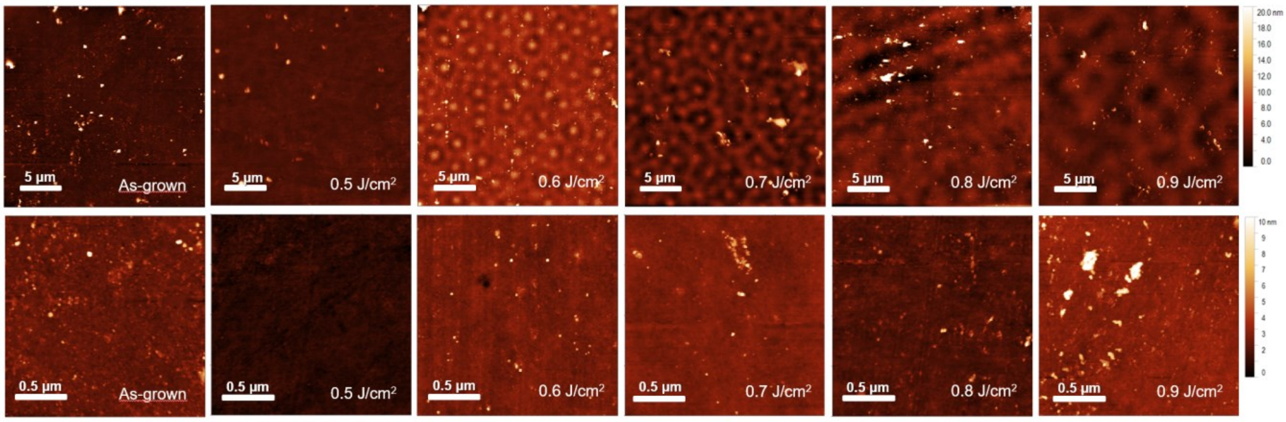

Figure 4.8: AFM images of the 9547 samples, the as grown sample's surface is shown on the left side and moving to the right the sample at increasing ED are reported. Beneath the images of a 20x20 µm^2 area, a zoom on a 2x2 µm^2 area is shown.

On the other hand, the surface of the samples form wafer 10258 exhibits an undulation on both the larger scale and the smaller one, as shown in figure 4.9. As also demonstrated with the Raman analysis, this samples shows an enhanced lattice modification produced by the laser processes in comparison to the other two. The roughness on the samples with energies over 600 mJ/cm^2 is higher in comparison to the other samples, and as already deduced in chapter 4.3 the lower thickness of the sample and the higher chemical concentration of the dopant might be responsible for the different regrowth after the laser process, affecting both strain and morphology. It's interesting to note that the as grown sample exhibits a lower quality surface in comparison to the other two wafers, as also supported by the Raman characterization, where a compressive stain is identified as opposed to the negligible tensile strain observed on the other two wafers. A summary of the average roughness of the Ge:P wafers is reported in figure 4.10 with respect to the energy density of the processes.

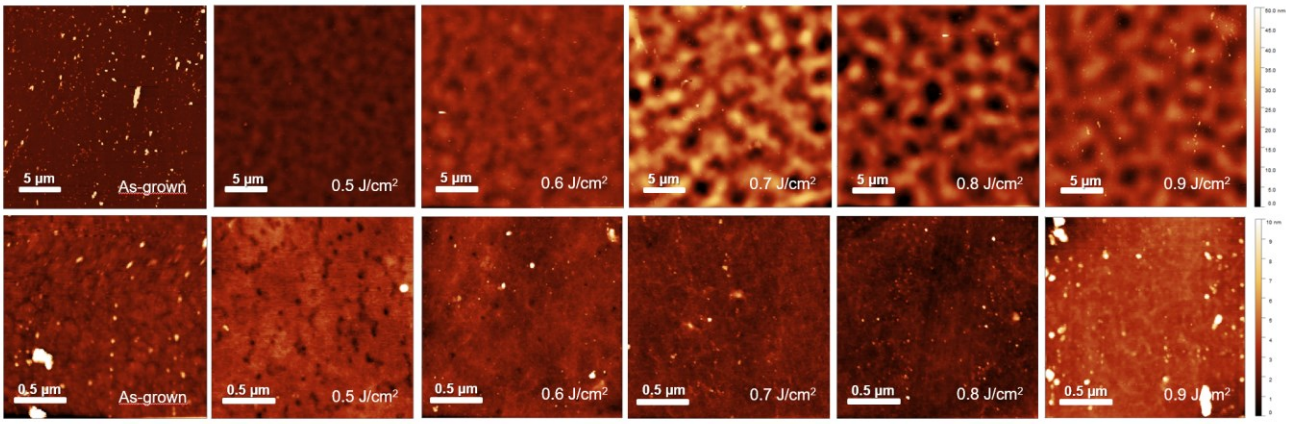

Figure 4.9: AFM images of the 10258 samples, the as grown sample's surface is shown on the left side and moving to the right the sample at increasing ED are reported. Beneath the images of a 20x20 µm^2 area, a zoom on a 2x2 µm^2 area is shown.

A summary of the surface roughness, in terms of root mean squares (RMS), measured for the three Ge:P on Si wafers is reported below for each energy density

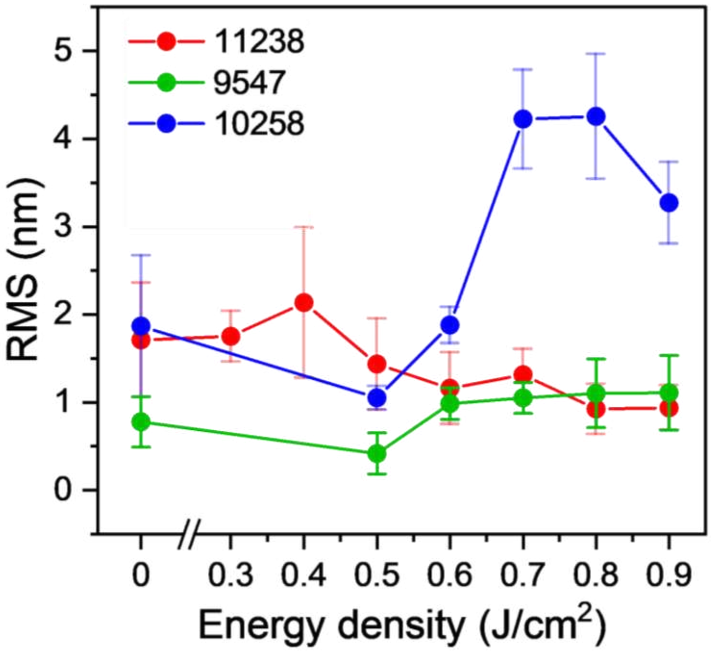

Figure 4.10: Summary of the roughness vs ED for the three Ge:P wafers

The samples from the SiGe:P wafer also show some surface ripples, but they are less pronounced and more disordered in comparison to the Ge:P 11238 wafer. By increasing the energy densities, the quality of the surface worsens, and after the 600 mJ/cm^2 threshold the roughness increases almost linearly with respect to the ED, figure 4.11.

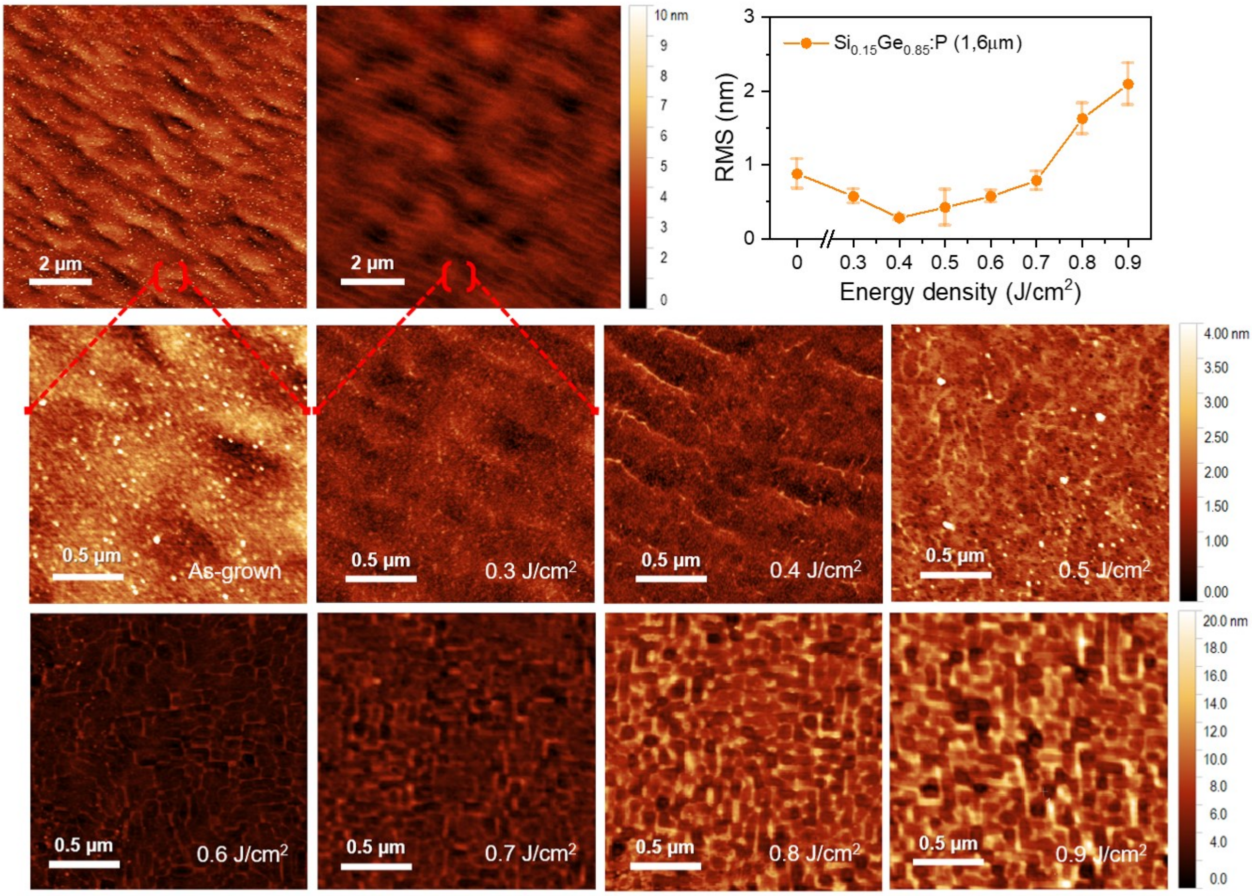

Figure 4.11: AFM images of the 11239 SiGe:P samples for each energy density. The two upper images show a large area scan (20x20 µm^2) for the as grown and 300 mJ/cm^2. Zooms on 2x2 µm^2 areas for all the energy densities are reported, to better highlight the surface modification by varying the ED.

The evidence that the most meaningful modifications happen after 600 mJ/cm^2 is also supported by the visual inspection done with an optical microscope that shows the formation of cracks on the surface at this energy, and their increase in number and size at higher energies, fig. 4.12. The formation of this cracks with increasing energy densities can be explained by the fact that with increasing ED the maximum melt depth increases and the effect of the mismatch of thermal expansion coefficient between silicon and germanium in the alloy is enough to produce a significant strain in the sample that is relaxed close to the surface through dislocations. The observation of the cracks beyond 600 mJ/cm^2, together with the inversion of the strain observed by Raman spectroscopy after this energy, from compressive to tensile, supports the idea that the compressive strain present in the grown sample is relaxed at high temperature during PLM, and then, upon cooling and related lattice contraction, a tensile parallel strain is produced.

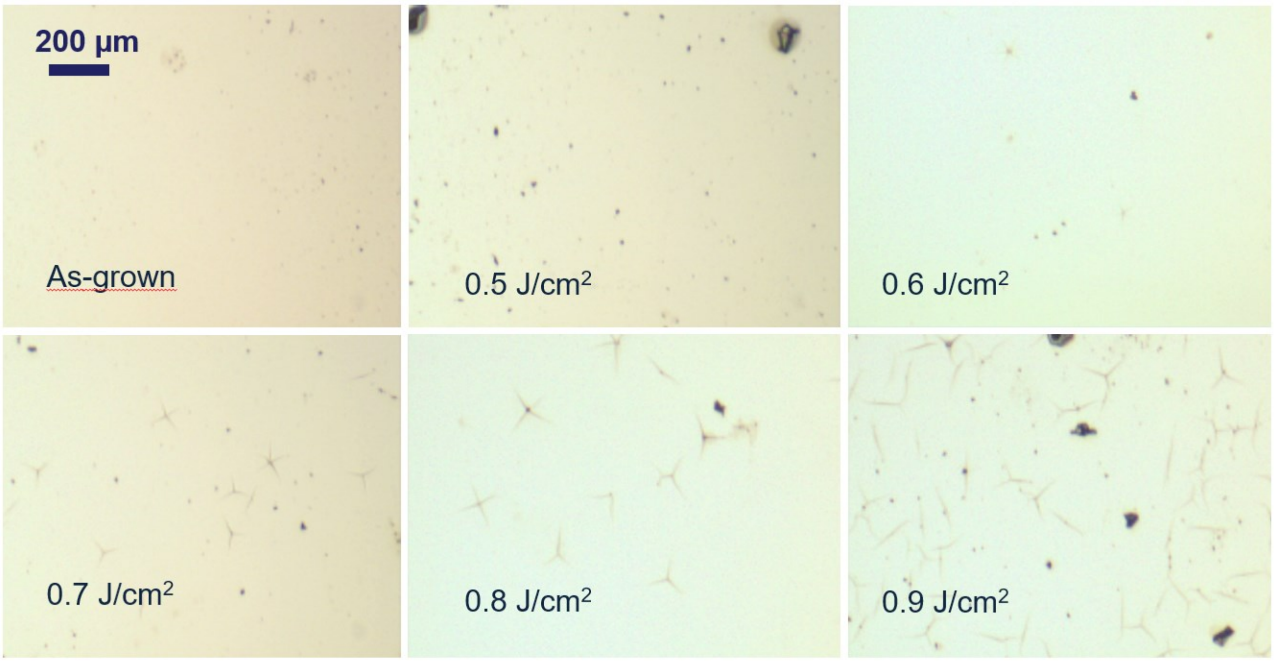

Figure 4.12: Optical microscope images of the SiGe:P samples' surface at each energy density. The surface is affected by cracks after 600 mJ/cm^2.

The morphological investigations on the Ge:P samples have led to the identification of the 900 mJ/cm^2 as the best energy density for the subsequent investigations. The samples processed at this energy are characterized by a good surface quality, and show the deepest MMD with high dopant activation, as will be shown in the electrical characterization section. These conditions have been selected by keeping in mind the possible application for the samples at PoliMi. The good surface quality is necessary for an epitaxial growth of the quantum well structures, while achieving a thicker activated layer is useful to increase the active region that can effectively reflect the IR radiation.

For the SiGe:P sample the best energy density was selected at 500 mJ/cm^2, where the cracks are still not produced and the MMD is the highest possible without surface damage.

The good crystallinity of the Ge:P samples has also been verified by the research group at PoliMi through XRD measurements on the 11238 wafer, that showed no visible variations for the un-processed and processed samples, bigger variations would probably be seen for wafer 10258 but no XRD measurements for this samples have been conducted as of the time of the thesis. For the SiGe:P wafer the effect of the laser, observed through the AFM images is also confirmed by the XRD measurement, where a loss of crystallinity is observed.

4.5 Electrical Characterization

Along the structural and morphological characterization, electrical information of the samples have been obtained through Van der Pauw-Hall measurements by applying the double layer model described in chapter 3.3.4.

The first characterizations were carried out on samples from the first process run (Ge:P 11238 and SiGe:P 11239), to evaluate the effect of the laser process, and the variation of laser energy density, on the effective incorporation of the phosphorus dopant into substitutional position in the matrix lattice. Electrical characterization indeed, give access to the electrically active portion of the total dopant concentration.
Continuing the investigations, samples from the other two wafers were also processed, and their electrical properties have been also studied with respect to the ED.

After the full set of data was obtained for the samples, the relation between the carrier mobility and the active carrier concentrations was studied, by applying an empirical fitting procedure.

The final step of the characterization was aimed at evaluating the thermal stability of the samples. Keeping in mind the possible applications as a reflective substrate for IR radiation in plasmonic devices, it was a necessity to study the deactivation of the samples after a thermal process, in order to evaluate the feasibility of a growth step on the samples while maintaining a good IR reflectivity (i.e. avoiding a strong deactivation).

4.5.1 Electrical properties vs. Laser energy density

The electrical measurements results are shown by plotting the electrical property vs. ED.

After the first characterization we saw an enhancement of the activation, thanks to laser processing, and samples from wafers 10258 and 9547 were also investigated, in the 500-900 mJ/cm^2 range.

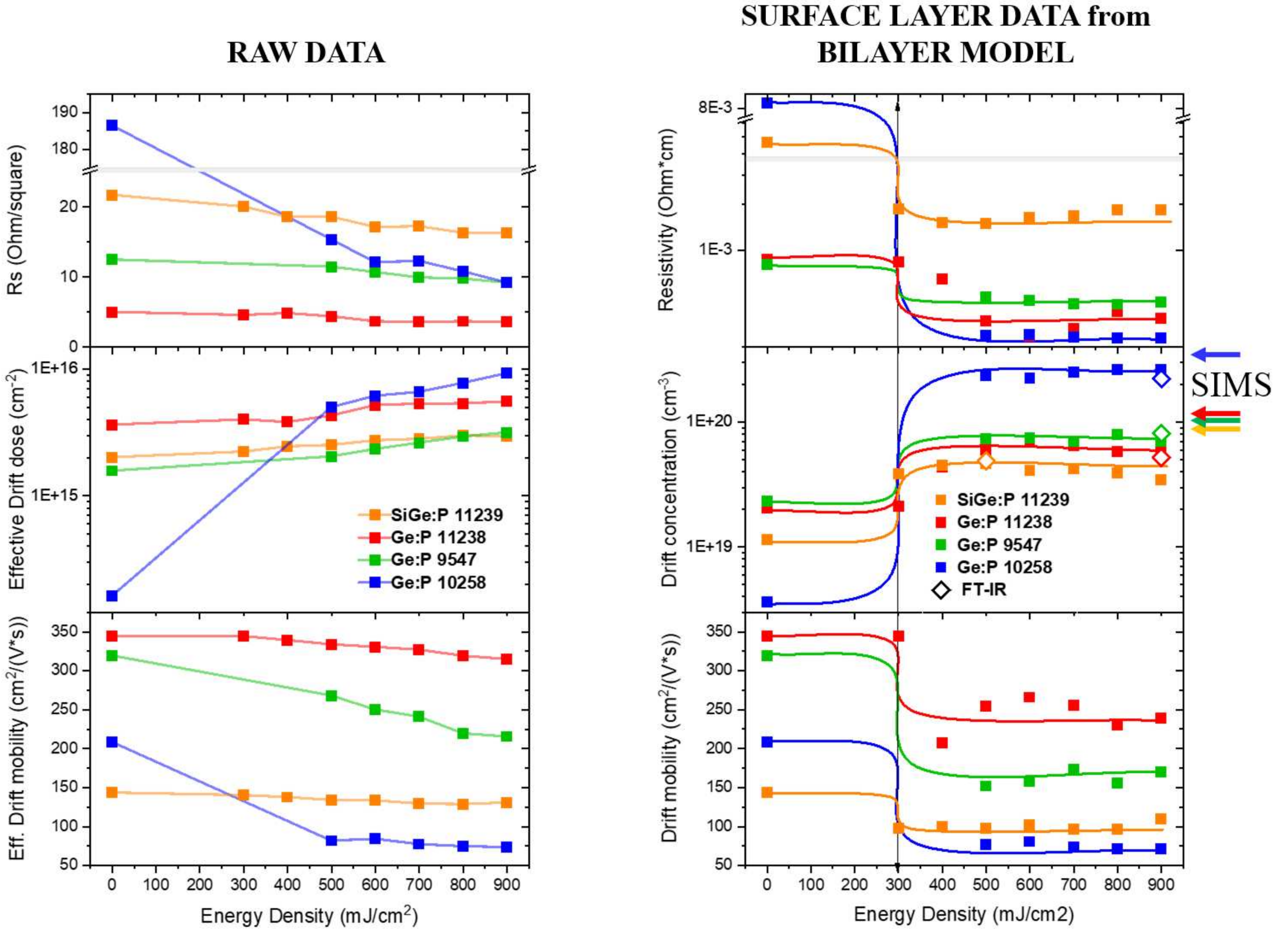

Figure 4.13: Electrical properties extracted from VdP-Hall measurements, on the left the raw data from the measurements are reported. On the right the bilayer model is applied, and the electrical properties of the processed layer are extracted, the results of FT-IR measurements performed at PoliMi are reported for comparison. The arrows on the right represent the SIMS chemical concentration for each sample.

In figure 4.13 a summary of the electrical properties for the samples is provided. Both the raw data, and the values calculated for the processed layer are reported.

In the raw data graph (left graphs in fig. 4.13) the sheet resistance R_S is directly measured via the VdP-Hall instrument, while the drift dose, n_S, and the drift mobility, μ,are calculated by using formulas 3.19 and 3.20, accounting for the Hall scattering factor ($r_H = 0.87$ in this study, as explained in chapter 3.3.4). The raw values are calculated by considering the entire grown layer thickness as the active layer, without distinguishing between the regrown region after the laser process and the region unaffected by the laser effect. While these values don't give specific information on the melted region, they represent the total properties of the samples and are not affected by some error that can be introduced by the bilayer model, mainly an incorrect estimation of the thickness of the region modified by the laser process.

The raw data show a slight overall activation of the samples, denoted by a decrease in the sheet resistance and an increase in the effective drift dose. As the drift dose increases the drift mobility decreases as expected by the inverse relationship between carrier concentration and carrier mobility.

The samples from the 10258 wafer show the most notable variations. This wafer exhibits the highest chemical concentration of the dopant, allowed by the growth at lower temperature in comparison to the other wafers. The high concentration of dopant is probably responsible for the different structural characteristics of the sample, already discussed in the previous sections, and also for the high sheet resistance observed in the as grown sample.

Looking at the properties of the as grown sample, we see that the high chemical concentration of dopants comes with an increased defectivity and worse surface, these two characteristics produce a lower active concentration of dopant identified at the contact between the metal tips and the surface, due to recombination of carriers.

The defectivity of the as grown sample is also highlighted by the fact that, while the drift dose is lower in comparison to the other wafers, the mobility of the carrier is not the highest, as we would expect from the lower dose.

At the same time this wafer is also the one that benefits the most from the PLM process: after processing the sheet resistance is in the range of all the other samples and the active concentration reaches the highest values for all the samples, while the mobility becomes the lowest.

The SiGe:P samples, while exhibiting a drift dose comparable to the 11238 and 9547 wafers, show a higher sheet resistance and lower mobility. The worse quality of the surface can explain the higher sheet resistance, and the high content of silicon lowers the mobilities of the carriers. The alloy mobility is influenced by the presence of silicon, that is characterized by a lower intrinsic mobility in comparison to germanium, so that the mobility of the carriers in the alloy is reduced in comparison to the mobility in pure germanium depending on the silicon concentration, following Vegard's law.

The graph on the right plots the electrical properties of the first layer, calculated by using the double layer model introduced in chapter 3.3.4. These values give an estimate of the properties of the region that has been affected by melting and subsequent recrystallization out of thermodynamic equilibrium. In this case the resistivity of the 1st layer is provided, along with drift concentration and drift mobility.

By separating the electrical contribution of the two layers, the effect of the laser process on the activation of the samples is more easily verified and its effect can be quantitatively evaluated.

By applying the double layer model, we calculate a maximum active concentration for the 10258 samples that reach a value of $n = 2.6 \times 10^{20}\ cm^{-3}$, effectively showing significant hyperdoping. The high activation is followed by the lowest resistivity and the lowest mobility.

The samples for the 11238 wafer, characterized by the thickest grown layer, show a lower activation for the 300 and 400 mJ/cm^2 samples, also supporting the previous observations that in this energy range the melting is not complete and so is the out-of-equilibrium incorporation of dopants.

The observation on the SiGe:P samples, done by analysing the raw data, hold true after applying the double layer model. The samples exhibit the highest resistivity and a low mobility. We can also observe the lowest activation of the dopant for all the wafers, while still being quite close to the 11238 and 9547.

Both the raw data and the double layer model don't show a strong correlation between the activation level of the samples and the laser energy density, as such the main effect produced by increasing the laser energy density is to increase the MMD.

The active concentration calculated for the Ge:P samples at 900 mJ/cm^2 and for the SiGe:P sample at 500 mJ/cm^2 with the VdP-Hall double layer model have been compared with Fourier Transform Infrared (FT-IR) spectroscopy carried out by the research group at PoliMi.
IR reflectivity spectra are acquired and, by using a double layer fitting model derived by Drude theory, the plasma frequency is extracted, and the active concentration is calculated by:

$$n_e = \frac{\omega_p^2 m^*}{\varepsilon_0 e^2} \tag{4.2}$$

A detailed description of the model is provided in [67]

The results obtained by FT-IR measurements are represented as the diamonds in the drift concentration graph for the 1st layer in figure 4.13. The results are in good agreement with the values obtained by VdP-Hall characterization, albeit a slight divergence in concentration is often calculated by the two methodologies, probably due to the difference in electron scattering introduced by the measurement procedures. While the VdP-Hall measurements are affected by carrier scattering, both induced by drift and the magnetoresistance (scattering with ionized impurities and acoustic phonons), the FT-IR measurements are affected by scattering with optical phonons when the plasma is put into oscillation by the electromagnetic wave penetrating the samples [68].

The FT-IR characterizations confirm that the highest activation is reached for the 900 mJ/cm^2 sample from wafer 10258, with a screen plasma wavelength of $\lambda^* \approx 3\mu m$, which demonstrates the ability of PLM to produce a uniform hyperdoping profile over a thickness of a few electromagnetic skin depths, approximately 300-500 nm, making it effective as an IR reflector.

A summary of the properties of the wafers and the electric properties of the 1st layer, calculated by the VdP-Hall bilayer model are reported in the table below. The properties of the samples processed at 900 mJ/cm^2 are shown for the Ge:P on Si wafers, while for the SiGe:P on Si wafer the sample processed at 500 mJ/cm^2 is selected.
The % activations with respect to the chemical dopant concentrations are also reported. Even by using strong out of equilibrium conditions the maximum activation achieved is 74% on the wafer with the highest chemical concentration of dopant. The main reason for the incomplete activation of the dopants still lies in the formation of dopant-vacancy clusters, as will be also suggested in the thermal stability study.

Wafer	Layer thickness (μm)	P chemical concentration (cm^{-3})	Drift concentration (cm^{-3})	Resistivity (Ω/cm)	Drift mobility cm^2/(V*s)	% activation
Ge:P 11238	1.8	1.3E20	6.1E19	4.3E-4	238.9	47.0%
Ge:P 10258	0.5	3.5E20	2.6E20	3.3E-4	71.3	74.3%
Ge:P 9547	0.6	1.1E20	7.0E19	5.2E-4	170.3	63.6%
SiGe:P 11239	1.6	1.1E20	4.6E19	1.39E-3	97.2	42.0%

Table 4.5: Electrical properties calculated for Ge:P samples processed at 900 mJ/cm^{2}and the SiGe:P sample processed at 500 mJ/cm^2. Thickness of the layer and chemical concentration of the dopant, obtained by SIMS measurements, are also reported.

4.5.2 Mobility vs active concentration

The relationship between the doping level of the samples and the mobility of the carrier has also been investigated for all the samples belonging to the Ge:P on Si wafers

In the less activated samples, the doping dependence of the mobilities agrees well with the *μ(n)* empirical fit recently proposed by Menéndez et al.[69]:

$$\mu = \frac{\mu_0}{1+\left(1-\frac{\alpha_0}{\alpha_1}\right)\left(\frac{1}{A}\right)^{\alpha_1}+\left(\frac{\alpha_0}{\alpha_1}\right)\left(\frac{1}{A}\right)^{\alpha_0-\alpha_1}\left(\frac{n}{A\times 10^{17}cm^{-3}}\right)^{\alpha_1}} \qquad 4.3$$

The model has been developed to analyse experimental values available in literature so far, where the active concentration didn't exceed the values of $n = 10^{20}\ cm^{-3}$. Some of our experimental data exceeded this value, and we see a dicsrepancy between the experimental data and the Menéndez fit extrapolation at high active concentrations, as shown in figure 4.14.

Indeed, at higher concentrations, we observed an enhanced inverse dependence between mobility and concentration of the carriers.

An additive term was added to the fit function, inspired by the work of Masetti et al.[70]

$$\mu = \frac{\mu_0}{1+\left(1-\frac{\alpha_0}{\alpha_1}\right)\left(\frac{1}{A}\right)^{\alpha_1}+\left(\frac{\alpha_0}{\alpha_1}\right)\left(\frac{1}{A}\right)^{\alpha_0-\alpha_1}\left(\frac{n}{A\times 10^{17}cm^{-3}}\right)^{\alpha_1}} - \frac{\mu_1}{1+\left(\frac{B}{n}\right)^{\beta}} \qquad 4.4$$

The data for the three Ge:P wafers, along the data from Menéndez [69] and Shayesteh et al. [71] have been plotted and fit with the formula 4.4.

By adding the correction from Masetti, the best-fit is able to describe the experimental data quite well, although the data form the sample 11238 lie between the two fits.

It's possible that different samples, characterized by varying defectivities, follow different regimes of scattering interactions between carriers and defects/ionized impurities and the weight of this interaction might be modulated by the doping level.

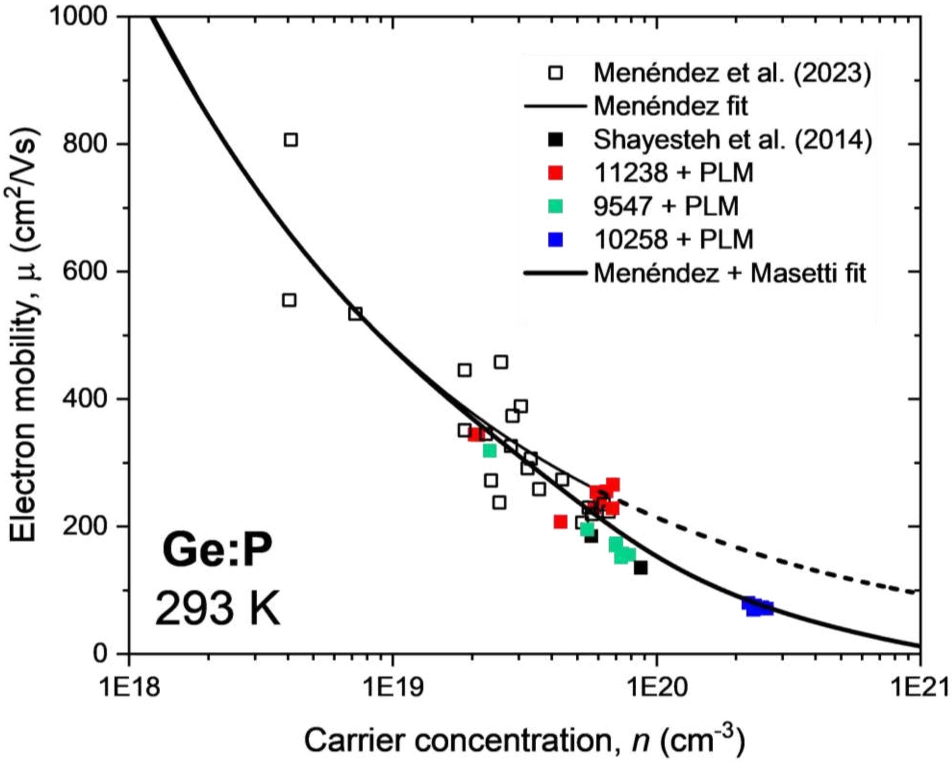

Figure 4.14: Graph of drift mobility, μ, in function of the carrier concentration, n, for the samples: 11238, 10258, 9547 along the experimental data of Menéndez et al.[69] and Shayesteh et al.[71]. The fits for both the Menéndez et al. model and the correction with the additional term from Masetti et al.[70] are shown

The best-fit has been obtained with the parameters shown in table 4.6. The parameters labelled with the * are fixed parameters obtained by Menedez et al., while the $\boldsymbol{B}$, β and μ_1 parameters are obtained by fitting in this work.

The μ_0^* parameter is the intrinsic mobility of pure germanium at 20 °C. The other parameters for the Menéndez fit are kept as fixed values and are sourced directly from [69].

μ_0^* ($cm^2/V*s$)	A^* (adim.)	α_0^* (adim.)	α_1^* (adim.)	μ_1 ($cm^2/V*s$)	$\boldsymbol{B}$ (adim.)	β (adim.)
3933.709	1.393	0.695	0.357	99.631	9E19	1.133

Table 4.6: Parameters for the Menéndez fit corrected with the Masetti term.

This demonstrates the ability of the empirical model to describe the mobility of the carriers in highly doped germanium, even in the hyper-doping regime, by adjusting the intrinsic mobility and fitting the Masetti term parameters.

4.5.3 Thermal stability study

For the evaluation of the thermal stability of the samples produced by PLM processing, the last process run was performed and samples from wafer 11238, 10258 and 9547 were subjected to a single laser pulse at 900 mJ/cm^2 energy density. The SiGe:P sample processed at 500 mJ/cm^2 during the first process run was also investigated, as it was determined to be the sample with the thickest MMD that still possessed good structural properties and surface quality. Their respective as grown samples have also been investigated in the same way.

The thermal stability study aims at assessing the sample resistance to deactivation when thermal energy is provided. The samples obtained by PLM processing, exhibit a high activation level, superior to the equilibrium concentration of active dopant (not to be confused with the solid solubility limit, which is related to the total chemical concentration). While a certain chemical concentration of phosphorus is allowed into the crystal matrix for germanium (solid solubility limit for P $\approx 1x10^{20}$), the active concentration is systematically lower. The deactivation of the samples occurs because an equilibrium between the active dopant atoms and other inactive species is established, the main reaction that leads to the deactivation of n-type dopants in germanium is the formation of active clusters, as explained in chapter 2.2.2 clustering with charged vacancies, that sets the thermal equilibrium for the active dopant concentration. The PLM samples are intrinsically unstable, considering the speed of recrystallization process, and the introduction of thermal energy is expected to promote the process of deactivation of the dopant by clustering with vacancies, already present in the sample, and possibly introduced by the PLM process itself.

To assess the thermal deactivation of the samples, an isochronal heating process has been performed thanks to the use of a Rapid Thermal Process (RTP) furnace (Jipelec JetFirst 150), that allows for a fast and controlled heating of the sample while also avoiding contamination and subsequent drive-in of unwanted species of the surface. The heating is provided by halogen lamps and the process is performed by purging the chamber from its atmosphere. The lamps are air cooled while the walls of the chamber are cooled down by water a cooling system. The samples sit on a silicon wafer and the temperature is constantly checked thanks to a thermocouple in the low temperature range (where its most sensitive), and a pyroelectric sensor for high temperatures, the power output of the lamp is dynamically adjusted in order to maintain a set temperature for the duration of the process, as well as to set a specific heating ramp (up to 15 °C/s).

As already anticipated, the thermal stability tests have been conducted by isochronal heating of the samples. The samples were subjected to thermal study in the range of 250-500 °C with a 25 °C step.

For the most doped sample the investigation started at 150 °C. The fast heating provided by the lamp allows us to neglect the heating time and consider the deactivation process to only occur during the constant temperature process.

The four samples are placed in the RTP furnace and are heated for 600 seconds at constant temperature, after each heating step the samples are retrieved and their electrical properties are assessed by VdP-Hall measurements.

The VdP-Hall experiments were used to calculate the carrier concentration after each heating step, and these values were studied by applying a phenomenological model developed by Nobili et al[72], from a mass action dynamic. The model starts from the assumption, widely demonstrated, that some dopants, at high chemical concentration, are activated in only a small percentage of the total concentration because of clustering with vacancies. For phosphorus in germanium, it has been demonstrated that the most stable cluster is made up of four dopant atoms and a vacancy[37]. An equilibrium between the active dopant and the clustered fraction is established, and as temperature is increased, the equilibrium is moved towards the formation of the clusters.

The phenomenological model introduced by Nobili explains the deactivation of the dopant thanks to the mass action equilibrium with a single cluster type, namely the most stable one, and while some clusters of different size might contribute to the total deactivation, the most stable cluster is considered as the major actor in the deactivation.

The model identifies a zero-order rate equation for the deactivation of the dopant that has the following mathematical form:

$$-\frac{dn}{dt} = A \cdot \exp\left(-\frac{E - \alpha n}{kT}\right) \qquad 4.5$$

Where n is the active carrier concentration, T is the temperature in Kelvin and k the Boltzmann constant. A and α are phenomenological parameters that exhibit a dependence on the total chemical concentration of the dopant and are independent of temperature. The term “$E - \alpha n$” is explained as an effective activation energy of the clustering process and has an inverse dependency on the active concentration of the dopant.

The model was developed for isothermal studies, while our thermal stability tests have been conducted by isochronal heating, meaning the active concentration of the dopant must be modified for each temperature step, to account for the variation of the effective activation energy. This term is able to describe the main driving force for the deactivation: as the active concentration of the dopant decreases, by clustering, the driving force that pushes the further deactivation of the dopant decreases and the effective activation energy of the clustering increases.

Equation 4.5 is integrated and a numerically solvable equation for the active carrier concentration is found:

$$n = n_0 - \frac{\mathrm{kT}}{\alpha} \ln{(Bt + 1)} \qquad 4.6$$

Where n_0 is the initial active concentration of the dopant before the heating, and t is the duration of the isochronal thermal treatment (600 s in our case).
The term B has the following form:

$$B = \frac{\alpha}{\mathrm{kT}} A \cdot \exp\left(-\frac{E - \alpha n_0}{kT}\right) \qquad 4.7$$

Equation 4.6 was numerically calculated by updating the initial active carrier concentration for each thermal treatment step in order to simulate the experimental data.

The experimental data and the simulation curve obtained by applying the Nobili model have been reported in an active carrier concentration vs. temperature graphs, for the four samples. In the same graphs the experimental FT-IR results obtained by PoliMi research group have also been reported for comparison, and the same simulation has been executed on their data. For each sample, an as grown reference sample has also been subjected to same thermal process, since the double layer model for the active carrier concentrations requires the knowledge of the unprocessed layer characteristics in order to separate the contribution of the two layers. Only by characterizing the properties of the non-processed samples at the same temperature as the processed ones we could have a valid reference for the second layer. The simulation has not been applied to the as-grown samples as they are expected to be more stable, having been grown at thermal equilibrium conditions, moreover the samples are less activated and thus less prone to deactivation.

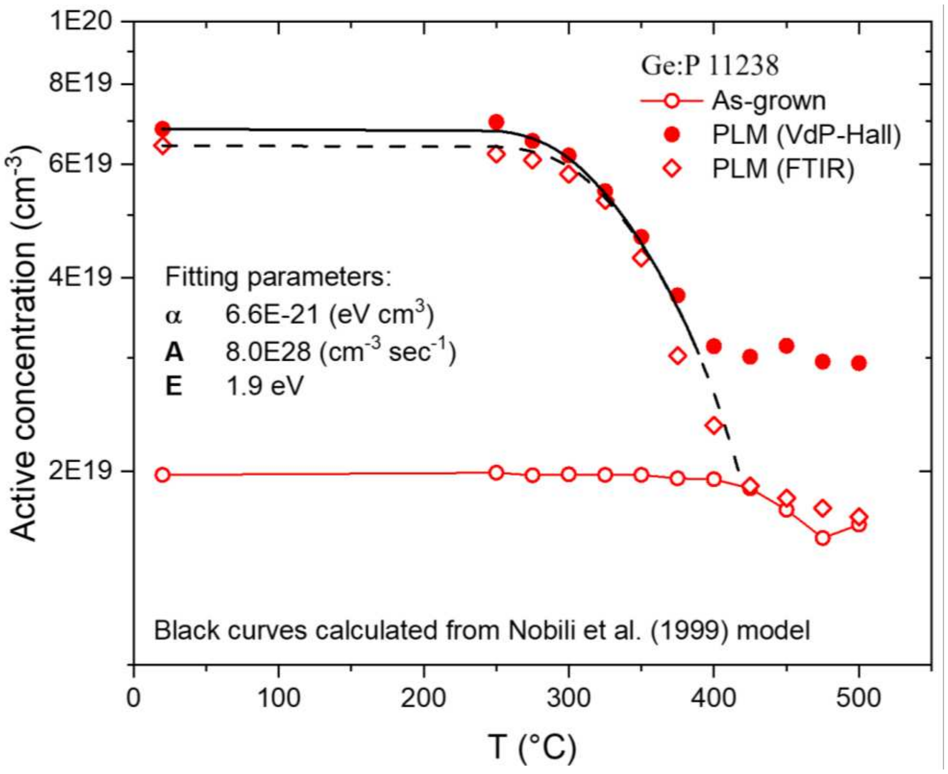

Figure 4.15: Thermal stability curves showing the experimental data obtained from Van der Pauw-Hall experiments and the simulation with the Nobili et al. model for both our data set and for the experimental data obtained from FTIR measurements, along with the as-grown data for reference. Sample Ge:P 11238

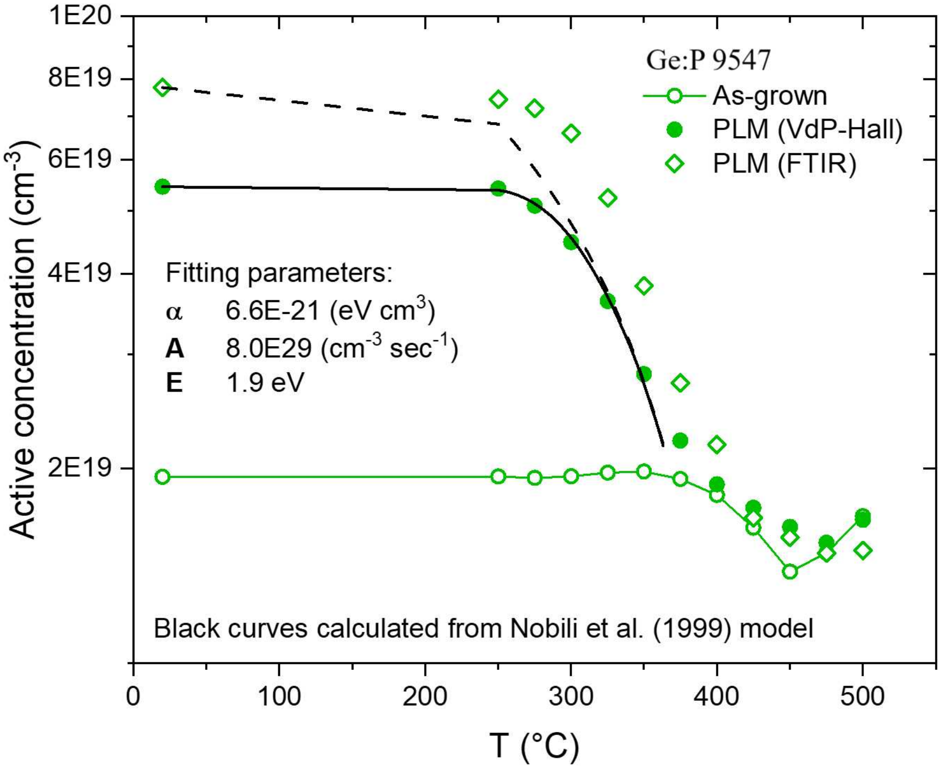

Figure 4.16: Thermal stability curves showing the experimental data obtained from Van der Pauw-Hall experiments and the simulation with the Nobili et al. model for both our data set and for the experimental data obtained from FTIR measurements, along with the as-grown data for reference. Sample Ge:P 9547

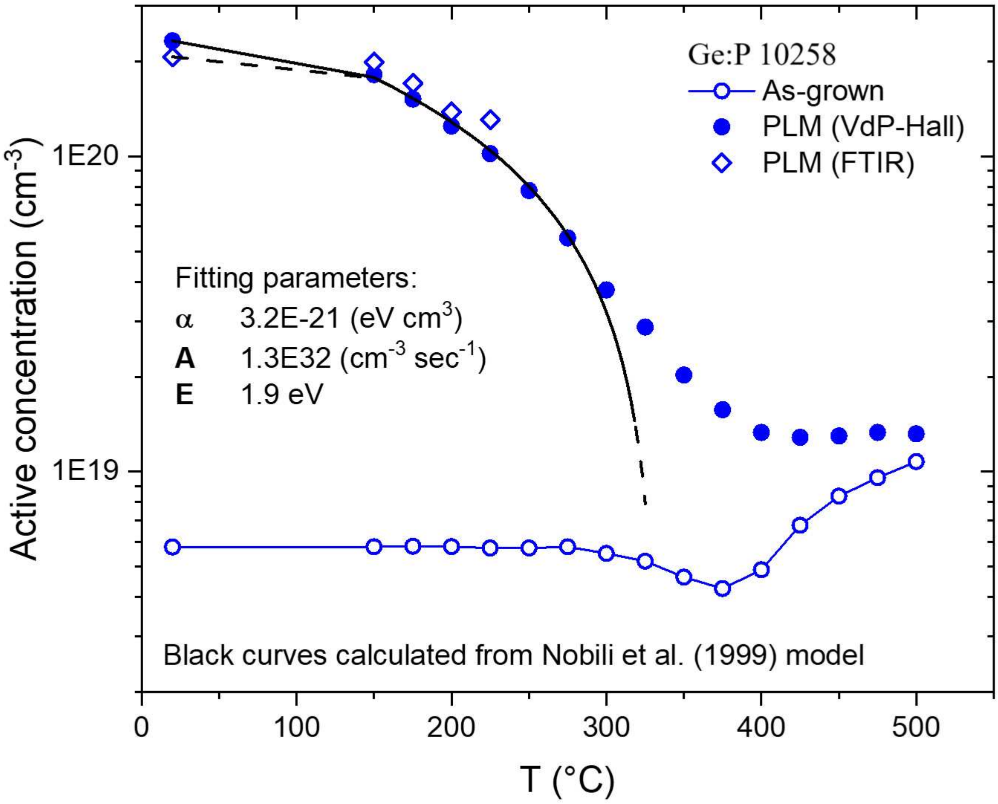

Figure 4.17: Thermal stability curves showing the experimental data obtained from Van der Pauw-Hall experiments and the simulation with the Nobili et al. model for both our data set and for the experimental data obtained from FTIR measurements, along with the as-grown data for reference. Sample Ge:P 10258

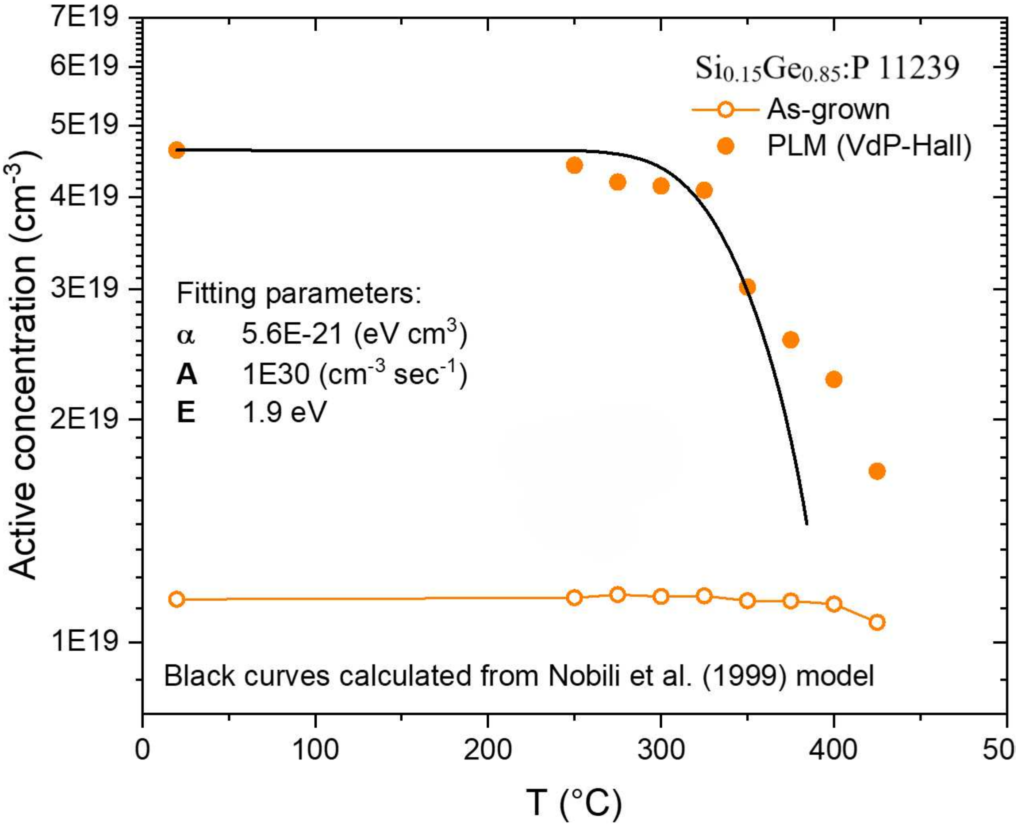

Figure 4.18: Thermal stability curves showing the experimental data obtained from Van der Pauw-Hall experiments and the simulation with the Nobili et al. model, along with the as-grown data for reference. Sample SiGe:P 11239

By looking at the graphs it possible to see that the fit with the model allows us to describe the deactivation process up to a certain temperature, that varies by samples, after which the model foresees a deactivation that is not observed by experimental results. This discrepancy is expected, since the model only considers the deactivation produced by the clustering process. But once a certain temperature is reached the inverse phenomenon is also triggered and the dissolution of the clusters is activated by the thermal energy. The rate of the deactivation is indeed slowed down by the competitive process of de-clustering and the curves become more sigmoidal, where the flexus identifies the temperature at which the de-clustering process starts to inhibit the deactivation in an observable way. At the higher temperatures in the curves for the samples 11238 and 10258 (fig. 4.15 and 4.17 respectively) a plateau is visible, suggesting that the equilibrium between the two mechanisms is being reached. For the sample 9547 (fig. 4.16) we don't see the plateau, but the flexus indicates that the equilibrium will be reached at higher temperatures outside the investigated range. For the SiGe:P sample both the flexus and the plateau are out of the investigated range, and further processes are needed to complete the investigation.

A clear difference in the temperature at which the deactivation starts is seen between the 10258 Ge:P sample and the other ones. The deactivation for this sample is triggered at 150 °C, while the other samples show a noticeable deactivation at the 300°C threshold. The clustering model explains this observation quite well: the 10258 sample exhibits both the highest active concentration among the investigated samples, thus the effective energy of the clustering activation is much lower in comparison to the other samples and as such the thermal energy provided at 150 °C is enough to start the clustering process. Moreover, it's also possible that the laser process on such a highly doped sample introduced more defects in comparison to the other samples, providing more vehicles for the dopant-vacancy interaction. As also foreseen by the model, at even higher active concentration the effective energy should eventually decreases so much that the sample would not be stable even at room temperature.

In the as grown samples' curves, we see a small deactivation at higher temperatures, and for the Ge:P samples we also see a slight reactivation, produced by the dissolution of small clusters that were formed during the growth phase.

Comparing the as-grown curves and the processed samples curves for the sample 9547 and 10258, we also observe that the active concentrations reached after the heating at the higher temperatures converge to the same equilibrium value. This observation confirms that the active concentration at equilibrium is the same, for the same material, independently of the sample history, if a high enough temperature is reached to restore its properties.

For the 11238 sample we don't reach a convergence between the processed and as grown sample, that is on the other hand observed by looking at the FT-IR data.

The fits for the FT-IR data are not able to follow the data as well as the fits do for the VdP-Hall data. This observation is explained by the fact that the fit parameters used to on the FT-IR data are the same used for the fit of the VdP-Hall ones, with the exception of having changed the initial active concentration to match that calculated by FT-IR. An optimization of the fit parameters for these measurements would certainly improve the fit.

Finally, it must be noted that, while the model was able to describe the VdP-Hall experimental data with a good agreement, the model was developed through an isothermal study on the samples. As such, the next step of the thermal stability investigation will consist in doing an isothermal study with new samples, while also taking into account the de-clustering effect.
Indeed, for the fit of the VdP-Hall data the activation energy for the clustering process was set as 1.9 eV for all the samples, referring to the value obtained by Nobili et al.[72] The α and A parameters for the fits were optimized by following the same empirical relation with the dopant chemical concentrations from the same study by Nobili, which are obtained on doped silicon. An isothermal characterization might allow to extract better empirical relationships for germanium-based samples.

Chapter 5

Conclusions

The aim of the thesis was to study the effect of the UV nanosecond laser anneal technique to induce a high activation of phosphorous dopant in germanium, thanks to the strong out-of-equilibrium conditions that are allowed by the laser processing. The samples that were investigated were provided by a collaboration with the L-NESS research group that aims at the obtainment of suitable substrates for the subsequent regrowth of multi-well quantum structures for the production of IR photonic devices. For this application, a high activation of the dopant in germanium is necessary to shift the plasma wavelength into the mid-IR range, where the organic molecules fingerprint region lies. At the same time a good thermal stability for the samples and a good surface quality is required for the subsequent LEPECVD growth.

Germanium is known to offer better electrical and optical properties in comparison to silicon; most notably a higher carrier mobility and a shorted band-gap that allows its utilization in optical devices like lasers and IR sensors.
However, the achievement of germanium n-type doping at high concentrations is not an easy task, and the difficulty in controlling the diffusion of the dopant inside the matrix is one of the biggest challenges to the integration of germanium into mainstream devices production. The main cause of the low active dopant concentration usually obtained under equilibrium conditions, as well as the increased mobility of n-type dopants in germanium in comparison to the p-type ones, is found in the interaction n-type dopants with a specific type of point defect, the vacancies. Vacancies are always present to a certain degree in a crystal lattice, but germanium exhibits higher concentration of vacancies in comparison to silicon in the same conditions.

During the thesis, several samples of phosphorous-doped germanium, and phosphorous doped silicon germanium alloy have been subjected to PLM processes with the objective of investigating the activation of the dopant outside of the equilibrium condition and evaluate the processes of deactivation that brings the material back to the equilibrium conditions.

The thesis work started with an initial investigation of the effects of the energy density on the overall activation of the samples, and how the energy density affects the electrical and structural properties of the samples. The samples were processed with single laser pulses in the 300-900 mJ/cm^2 range. No strong correlation was found between the laser energy density and the electrical activation of the samples, as long as the melting is fully induced on the surface layer.

It has been demonstrated the PLM process is able to activate the samples well over the equilibrium activation. The highest activation was achieved on a sample that exhibits a high chemical concentration of the dopant, reaching the hyper-doping regime, with a level of incorporation of $2.6x10^{20}$ atoms/cm^3, with a 74% activation. This has also shown that 100% activation is still inhibited by samples defectivity even with a fast recrystallization that occurs in the timespan of hundreds of nanoseconds.

The morphological and structural study on the samples have shown that the maximum melt depth has a linear dependency with the energy density and by tuning it is possible to control the thickness of the activated layer. The Ge:P samples have shown a good surface regrowth after the laser induced melting, even maintaining the surface features present before the laser process. The highly doped samples are an exception, where the excess of dopant, and the layer thinness produce a higher strain on the activated layer and a worse surface quality. The strain produced on the surface layer has been evaluated and low values of tensile strain have been identified for the laser processed samples.

The SiGe:P alloy is characterized by the formation of surface cracks after 600 mJ/cm^2, underlining the effect of the thermal coefficient mismatch between silicon and germanium in the processes of strain relaxation during the cooling of the surface.

The relationship between the mobility of the carrier and the active doping level has been investigated thanks to the use of an empirical interpretation models and a correction factor for the high doping regime has been applied to describe the experimental data. It has been shown that as the doping level reaches the 1×10^{20} cm^{-3} regime, an enhanced decrease in mobility is observed. The SiGe:P alloy shows a lower mobility, as expected considering the high concentration of silicon that mediates the average mobility in the lattice, by modifying the band structure with Vegard-like dependence.

Finally, the thermal stability of the samples has been investigated. The samples have shown a good stability up to 300 °C, with the exception of the highest activated samples that is stable up to 150 °C. The deactivation of the samples is explained by the formation of an equilibrium between the active fraction of the dopants and inactive clusters with charged vacancies. The driving force of the clustering is the modulated by both the total chemical concentration of the dopant, and the active concentration. The more activated beyond the equilibrium the sample is, the faster and at lower temperatures the deactivation will occur. In order to fully describe the experimental data obtained for the thermal stability test, the effect of the clusters dissolution at higher temperature has to be accounted for. This will be the next step for the investigations.

The results obtained during the thesis are quite promising both in terms of electrical properties and structural and morphological ones. Certainly, the high doping regime induces stronger modifications on the lattice that can affect its thermal stability and be a hindrance for the integration of germanium into the large-scale device production.

The interaction of the n-type dopants with the vacancies remains the main issue to be overcome.

The inhibition of this interaction by many forms of co-doping is being investigated in recent years, and the production of highly pure germanium layers, with a low vacancy concentration, might help to reduce the deactivation of the dopants, if the doping and activation techniques don’t induce a higher vacancy concentration, nullifying the benefit.

References

[1] E. E. Haller, “Germanium: From its discovery to SiGe devices,” *Mater Sci Semicond Process*, vol. 9, no. 4–5, pp. 408–422, Aug. 2006, doi: 10.1016/j.mssp.2006.08.063.

[2] W. Chung, H. Wu, and P. D. Ye, “Integration of Germanium into Modern CMOS: Challenges and Breakthroughs,” in *Advanced Nanoelectronics*, Wiley, 2018, pp. 91–117. doi: 10.1002/9783527811861.ch4.

[3] W.C. Pat Shanks III, Bryn E. Kimball, Amy C. Tolcin, and David E. Guberman, “Critical Mineral Resources of the United States—Economic and Environmental Geology and Prospects for Future Supply,” 2017. doi: 10.3133/pp1802I.

[4] C. EL Latunussa *et al.*, “Study on the EU’s list of critical raw materials (2020) – Critical raw materials factsheets”, doi: 10.2873/631546.

[5] G. Pellegrini *et al.*, “Benchmarking the Use of Heavily Doped Ge for Plasmonics and Sensing in the Mid-Infrared,” *ACS Photonics*, vol. 5, no. 9, pp. 3601–3607, Sep. 2018, doi: 10.1021/acsphotonics.8b00438.

[6] R. E. Camacho-Aguilera *et al.*, “An electrically pumped germanium laser,” *Opt Express*, vol. 20, no. 10, p. 11316, May 2012, doi: 10.1364/OE.20.011316.

[7] T. Okumura, K. Oda, J. Kasai, M. Sagawa, and Y. Suwa, “Optical net gain measurement in n-type doped germanium waveguides under optical pumping for silicon monolithic laser,” *Opt Express*, vol. 24, no. 9, p. 9132, May 2016, doi: 10.1364/oe.24.009132.

[8] N. Takahashi, S. Itoi, Y. Nakashima, W. Zhao, H. Onoda, and S. Sakai, “High temperature ion implanter for SiC and Si devices,” in *2015 15th International Workshop on Junction Technology (IWJT)*, IEEE, Jun. 2015, pp. 6–7. doi: 10.1109/IWJT.2015.7467062.

[9] F. Adeni Khaja, B. Colombeau, T. Thanigaivelan, D. Ramappa, and T. Henry, “Physical understanding of cryogenic implant benefits for electrical junction stability,” *Appl Phys Lett*, vol. 100, no. 11, Mar. 2012, doi: 10.1063/1.3694275.

[10] M. I. Current, “Ion implantation of advanced silicon devices: Past, present and future,” May 01, 2017, *Elsevier Ltd*. doi: 10.1016/j.mssp.2016.10.045.

[11] E. Napolitani *et al.*, “Role of ion mass on damage accumulation during ion implantation in Ge,” *Physica Status Solidi (A) Applications and Materials Science*, vol. 211, no. 1, pp. 118–121, Jan. 2014, doi: 10.1002/pssa.201300324.

[12] E. Napolitani and G. Impellizzeri, “Ion Implantation Defects and Shallow Junctions in Si and Ge,” in *Semiconductors and Semimetals*, vol. 91, Academic Press Inc., 2015, pp. 93–122. doi: 10.1016/bs.semsem.2015.01.001.

[13] M. J. Süess *et al.*, “Analysis of enhanced light emission from highly strained germanium microbridges,” *Nat Photonics*, vol. 7, no. 6, pp. 466–472, Jun. 2013, doi: 10.1038/nphoton.2013.67.

[14] M. Myronov, P. Jahandar, S. Rossi, K. Sewell, F. Murphy-Armando, and F. Pezzoli, “Efficient In Situ Doping of Strained Germanium Tin Epilayers at Unusually Low Temperature,” *Adv Electron Mater*, 2024, doi: 10.1002/aelm.202300811.

[15] S. Fischler, “Correlation between Maximum Solid Solubility and Distribution Coefficient for Impurities in Ge and Si,” *J Appl Phys*, vol. 33, no. 4, pp. 1615–1615, Apr. 1962, doi: 10.1063/1.1728792.

[16] R. W. Olesinski and G. J. Abbaschian, “The Ga−Ge (Gallium-Germanium) system,” *Bulletin of Alloy Phase Diagrams*, vol. 6, no. 3, pp. 258–262, Jun. 1985, doi: 10.1007/BF02880411.

[17] R. W. Olesinski and G. J. Abbaschian, “The Ge−Sb (Germanium-Antimony) system,” *Bulletin of Alloy Phase Diagrams*, vol. 7, no. 3, pp. 219–222, Jun. 1986, doi: 10.1007/BF02868990.

[18] R. W. Olesinski and G. J. Abbaschian, “The B−Ge (Boron-Germanium) system,” *Bulletin of Alloy Phase Diagrams*, vol. 5, no. 5, pp. 476–478, Oct. 1984, doi: 10.1007/BF02872899.

[19] F. A. Trumbore, “Solid Solubilities of Impurity Elements in Germanium and Silicon".”

[20] G. Impellizzeri *et al.*, “Aluminium Implantation in Germanium: Uphill Diffusion, Electrical Activation, and Trapping,” *Applied Physics Express*, vol. 5, no. 2, p. 021301, Jan. 2012, doi: 10.1143/APEX.5.021301.

[21] G. Impellizzeri, S. Mirabella, A. Irrera, M. G. Grimaldi, and E. Napolitani, “Ga-implantation in Ge: Electrical activation and clustering,” *J Appl Phys*, vol. 106, no. 1, Jul. 2009, doi: 10.1063/1.3159031.

[22] G. Impellizzeri, S. Mirabella, E. Bruno, A. M. Piro, and M. G. Grimaldi, “B activation and clustering in ion-implanted Ge,” *J Appl Phys*, vol. 105, no. 6, Mar. 2009, doi: 10.1063/1.3091289.

[23] M. Posselt *et al.*, “P implantation into preamorphized germanium and subsequent annealing: Solid phase epitaxial regrowth, P diffusion, and activation,” *Journal of Vacuum Science & Technology B: Microelectronics and Nanometer Structures Processing, Measurement, and Phenomena*, vol. 26, no. 1, pp. 430–434, Jan. 2008, doi: 10.1116/1.2805249.

[24] S. Prucnal *et al.*, “Ultra-doped n-type germanium thin films for sensing in the mid-infrared,” *Sci Rep*, vol. 6, Jun. 2016, doi: 10.1038/srep27643.

[25] S. Prucnal *et al.*, “Superconductivity in single-crystalline aluminum- and gallium-hyperdoped germanium,” *Phys Rev Mater*, vol. 3, no. 5, p. 054802, May 2019, doi: 10.1103/PhysRevMaterials.3.054802.

[26] G. Impellizzeri *et al.*, “B-doping in Ge by excimer laser annealing,” *J Appl Phys*, vol. 113, no. 11, Mar. 2013, doi: 10.1063/1.4795268.

[27] V. Mazzocchi *et al.*, “Boron and Phosphorus dopant activation in Germanium using laser annealing with and without preamorphization implant,” in *2009 17th International Conference on Advanced Thermal Processing of Semiconductors*, IEEE, Sep. 2009, pp. 1–5. doi: 10.1109/RTP.2009.5373447.

[28] R. Milazzo *et al.*, “N-type doping of Ge by As implantation and excimer laser annealing,” *J Appl Phys*, vol. 115, no. 5, Feb. 2014, doi: 10.1063/1.4863779.

[29] R. Milazzo *et al.*, “p-type doping of Ge by Al ion implantation and pulsed laser melting,” *Appl Surf Sci*, vol. 509, p. 145230, Apr. 2020, doi: 10.1016/j.apsusc.2019.145230.

[30] C. Carraro *et al.*, “N-type heavy doping with ultralow resistivity in Ge by Sb deposition and pulsed laser melting,” *Appl Surf Sci*, vol. 509, p. 145229, Apr. 2020, doi: 10.1016/j.apsusc.2019.145229.

[31] F. Cristiano and A. La Magna, *Laser Annealing Processes in Semiconductor Technology*. Elsevier, 2021. doi: 10.1016/C2019-0-01254-X.

[32] R. Milazzo *et al.*, “Impurity and defect interactions during laser thermal annealing in Ge,” *J Appl Phys*, vol. 119, no. 4, Jan. 2016, doi: 10.1063/1.4940737.

[33] H. Mehrer, *Diffusion in Solids*, vol. 155. in Springer Series in Solid-State Sciences, vol. 155. Berlin, Heidelberg: Springer Berlin Heidelberg, 2007. doi: 10.1007/978-3-540-71488-0.

[34] M. Werner, H. Mehrer, and H. D. Hochheimer, “Effect of hydrostatic pressure, temperature, and doping on self-diffusion in germanium,” *Phys Rev B*, vol. 32, no. 6, pp. 3930–3937, Sep. 1985, doi: 10.1103/PhysRevB.32.3930.

[35] J. Vanhellemont, P. Śpiewak, and K. Sueoka, “On the solubility and diffusivity of the intrinsic point defects in germanium,” *J Appl Phys*, vol. 101, no. 3, Feb. 2007, doi: 10.1063/1.2429718.

[36] E. Hüger *et al.*, “Self-diffusion in germanium isotope multilayers at low temperatures,” *Appl Phys Lett*, vol. 93, no. 16, Oct. 2008, doi: 10.1063/1.3002294.

[37] A. Chroneos and H. Bracht, “Diffusion of n -type dopants in germanium,” *Appl Phys Rev*, vol. 1, no. 1, 2014, doi: 10.1063/1.4838215.

[38] S. Brotzmann and H. Bracht, “Intrinsic and extrinsic diffusion of phosphorus, arsenic, and antimony in germanium,” *J Appl Phys*, vol. 103, no. 3, 2008, doi: 10.1063/1.2837103.

[39] S. Brotzmann *et al.*, “Diffusion and defect reactions between donors, C, and vacancies in Ge. I. Experimental results,” *Phys Rev B*, vol. 77, no. 23, p. 235207, Jun. 2008, doi: 10.1103/PhysRevB.77.235207.

[40] A. Chroneos, R. W. Grimes, B. P. Uberuaga, and H. Bracht, “Diffusion and defect reactions between donors, C, and vacancies in Ge. II. Atomistic calculations of related complexes,” *Phys Rev B*, vol. 77, no. 23, p. 235208, Jun. 2008, doi: 10.1103/PhysRevB.77.235208.

[41] A. Vohra *et al.*, “Heavily phosphorus doped germanium: Strong interaction of phosphorus with vacancies and impact of tin alloying on doping activation,” *J Appl Phys*, vol. 125, no. 22, Jun. 2019, doi: 10.1063/1.5107503.

[42] A. Chroneos, R. W. Grimes, H. Bracht, and B. P. Uberuaga, “Engineering the free vacancy and active donor concentrations in phosphorus and arsenic double donor-doped germanium,” *J Appl Phys*, vol. 104, no. 11, 2008, doi: 10.1063/1.3035847.

[43] P. Tsouroutas, D. Tsoukalas, and H. Bracht, “Experiments and simulation on diffusion and activation of codoped with arsenic and phosphorous germanium,” *J Appl Phys*, vol. 108, no. 2, Jul. 2010, doi: 10.1063/1.3456998.

[44] S. Stathopoulos, L. Tsetseris, N. Pradhan, B. Colombeau, and D. Tsoukalas, “Millisecond non-melt laser annealing of phosphorus implanted germanium: Influence of nitrogen co-doping,” *J Appl Phys*, vol. 118, no. 13, Oct. 2015, doi: 10.1063/1.4932600.

[45] P. Baeri, S. U. Campisano, G. Foti, and E. Rimini, “A melting model for pulsing-laser annealing of implanted semiconductors,” *J Appl Phys*, vol. 50, no. 2, pp. 788–797, Feb. 1979, doi: 10.1063/1.326046.

[46] C. M. Surko, A. L. Simons, D. H. Auston, J. A. Golovchenko, R. E. Slusher, and T. N. C. Venkatesan, “Calculation of the dynamics of surface melting during laser annealing,” *Appl Phys Lett*, vol. 34, no. 10, pp. 635–637, May 1979, doi: 10.1063/1.90619.

[47] R. F. Wood, J. R. Kirkpatrick, and G. E. Giles, “Macroscopic theory of pulsed-laser annealing. II. Dopant diffusion and segregation,” *Phys Rev B*, vol. 23, no. 10, pp. 5555–5569, May 1981, doi: 10.1103/PhysRevB.23.5555.

[48] D. Chrastina *et al.*, “LEPECVD — A Production Technique for SiGe MOSFETs and MODFETs,” 2005, pp. 17–29. doi: 10.1007/1-84628-235-7_2.

[49] Y. Gao, “A new secondary ion mass spectrometry technique for III-V semiconductor compounds using the molecular ions CsM+,” *J Appl Phys*, vol. 64, no. 7, pp. 3760–3762, Oct. 1988, doi: 10.1063/1.341381.

[50] T. Beechem, A. Christensen, S. Graham, and D. Green, “Micro-Raman thermometry in the presence of complex stresses in GaN devices,” *J Appl Phys*, vol. 103, no. 12, Jun. 2008, doi: 10.1063/1.2940131.

[51] U. Monteverde, M. A. Migliorato, J. Pal, and D. Powell, “Elastic and vibrational properties of group IV semiconductors in empirical potential modelling,” *Journal of Physics: Condensed Matter*, vol. 25, no. 42, p. 425801, Oct. 2013, doi: 10.1088/0953-8984/25/42/425801.

[52] F. Pezzoli *et al.*, “Strain-induced shift of phonon modes in Si1 - x Gex alloys,” *Mater Sci Semicond Process*, vol. 9, no. 4-5 SPEC. ISS., pp. 541–545, Aug. 2006, doi: 10.1016/j.mssp.2006.08.046.

[53] D. E. Aspnes and A. A. Studna, “Dielectric functions and optical parameters of Si, Ge, GaP, GaAs, GaSb, InP, InAs, and InSb from 1.5 to 6.0 eV,” *Phys Rev B*, vol. 27, no. 2, pp. 985–1009, Jan. 1983, doi: 10.1103/PhysRevB.27.985.

[54] J. Frigerio *et al.*, “Optical properties of highly n-doped germanium obtained by in situ doping and laser annealing,” *J Phys D Appl Phys*, vol. 50, no. 46, Oct. 2017, doi: 10.1088/1361-6463/aa8eca.

[55] Van der Pauw L.J., “A method of measuring specific resistivity and Hall effect of discs of arbitrary shape,” *Philips Res. Repts*, vol. 13, no. 1, pp. 1–9, Feb. 1958.

[56] C. Xu, C. L. Senaratne, P. Sims, J. Kouvetakis, and J. Menéndez, “Ultralow Resistivity Ge:Sb heterostructures on Si Using Hydride Epitaxy of Deuterated Stibine and Trigermane,” *ACS Appl Mater Interfaces*, vol. 8, no. 36, pp. 23810–23819, Sep. 2016, doi: 10.1021/acsami.6b06161.

[57] R. L. Petritz, “Theory of an Experiment for Measuring the Mobility and Density of Carriers in the Space-Charge Region of a Semiconductor Surface,” *Physical Review*, vol. 110, no. 6, pp. 1254–1262, Jun. 1958, doi: 10.1103/PhysRev.110.1254.

[58] R. Baron, G. A. Shifrin, O. J. Marsh, and J. W. Mayer, “Electrical Behavior of Group III and V Implanted Dopants in Silicon,” *J Appl Phys*, vol. 40, no. 9, pp. 3702–3719, Aug. 1969, doi: 10.1063/1.1658260.

[59] J. D. Weiss, “Generalization of the van der Pauw relationship derived from electrostatics,” *Solid State Electron*, vol. 62, no. 1, pp. 123–127, Aug. 2011, doi: 10.1016/j.sse.2011.04.006.

[60] S. M. Anlage, V. V. Talanov, and A. R. Schwartz, “Principles of Near-Field Microwave Microscopy,” in *Scanning Probe Microscopy*, New York, NY: Springer New York, pp. 215–253. doi: 10.1007/978-0-387-28668-6_8.

[61] J. Hoffmann, M. Wollensack, M. Zeier, J. Niegemann, H.-P. Huber, and F. Kienberger, “A calibration algorithm for nearfield scanning microwave microscopes,” in *2012 12th IEEE International Conference on Nanotechnology (IEEE-NANO)*, IEEE, Aug. 2012, pp. 1–4. doi: 10.1109/NANO.2012.6322116.

[62] G. Gomila, J. Toset, and L. Fumagalli, “Nanoscale capacitance microscopy of thin dielectric films,” *J Appl Phys*, vol. 104, no. 2, 2008, doi: 10.1063/1.2957069.

[63] D. Fontana *et al.*, “Ex-situ n-type heavy doping of Ge1-xSnx epilayers by surface Sb deposition and pulsed laser melting,” *Appl Surf Sci*, vol. 600, Oct. 2022, doi: 10.1016/j.apsusc.2022.154112.

[64] F. Pezzoli *et al.*, “Raman spectroscopy of Si1−xGex epilayers,” *Materials Science and Engineering: B*, vol. 124–125, no. SUPPL., pp. 127–131, Dec. 2005, doi: 10.1016/j.mseb.2005.08.057.

[65] F. Pezzoli *et al.*, “Phonon strain shift coefficients in Si1-x Gex alloys,” *J Appl Phys*, vol. 103, no. 9, 2008, doi: 10.1063/1.2913052.

[66] W. Dorsch, B. Steiner, M. Albrecht, H. P. Strunk, H. Wawra, and G. Wagner, “The transition from ripples to islands in strained heteroepitaxial growth under low driving forces,” *J Cryst Growth*, vol. 183, no. 3, pp. 305–310, Jan. 1998, doi: 10.1016/S0022-0248(97)00430-2.

[67] J. Frigerio *et al.*, “Tunability of the dielectric function of heavily doped germanium thin films for mid-infrared plasmonics,” *Phys Rev B*, vol. 94, no. 8, p. 085202, Aug. 2016, doi: 10.1103/PhysRevB.94.085202.

[68] J. Frigerio *et al.*, “Ge-on-Si based mid-infrared plasmonics,” SPIE-Intl Soc Optical Eng, Mar. 2021, p. 19. doi: 10.1117/12.2576175.

[69] J. Menéndez, C. Xu, and J. Kouvetakis, “Consistent optical and electrical determination of carrier concentrations for the accurate modeling of the transport properties of n-type Ge,” *Mater Sci Semicond Process*, vol. 164, Sep. 2023, doi: 10.1016/j.mssp.2023.107596.

[70] G. Masetti, ’ M.-, R. Severi, and S. Solmi, “Modeling of Carrier Mobility Against Carrier Concentration in Arsenic-, Phosphorus-, and Boron-lhped Silicon,” 1983.

[71] M. Shayesteh *et al.*, “Optimized Laser Thermal Annealing on Germanium for High Dopant Activation and Low Leakage Current,” *IEEE Trans Electron Devices*, vol. 61, no. 12, pp. 4047–4055, Dec. 2014, doi: 10.1109/TED.2014.2364957.

[72] D. Nobili, S. Solmi, M. Merli, and J. Shao, “Deactivation Kinetics in Heavily Arsenic-Doped Silicon,” *J Electrochem Soc*, vol. 146, no. 11, pp. 4246–4252, Nov. 1999, doi: 10.1149/1.1392622.

[73] A. Sanson *et al.*, “Non-Conventional Characterization of Electrically Active Dopant Profiles in Al-Implanted Ge by Depth-Resolved Micro-Raman Spectroscopy,” *Applied Physics Express*, vol. 6, no. 4, p. 042404, Apr. 2013, doi: 10.7567/APEX.6.042404.

Appendix

SMM trials

As introduced before, the result of the first SMM investigations are placed inside the appendix, as no samples for the thesis work has been yet analysed with the technique.

The work with the SMM configuration for the instrument started with a series of trials on known samples, in order to understand the working of the technique and its response to the variation of electrical properties of the samples. The technique works in contact mode, as such all the samples require a flat morphology in order to preserve the tip conditions. The tip used for the characterizations is a 25PtIr300G SMM tip. The tip substrate is provided with a gold strip that allows for the electrical connection between the PtIr tip and the transmission line. An image of the tip and substrate are reported in figure A.1

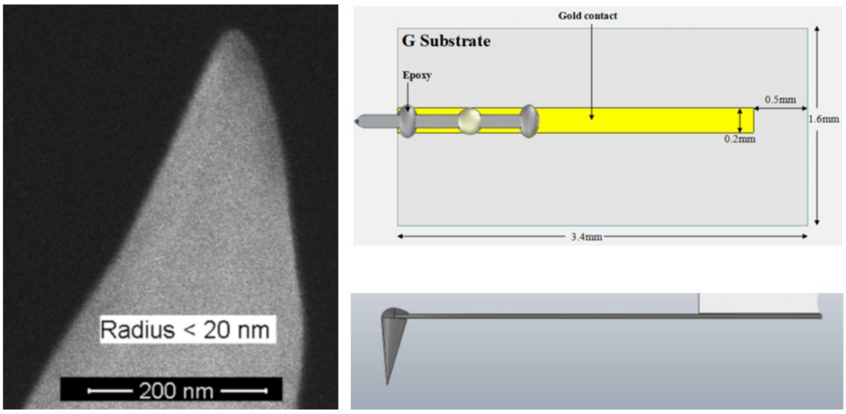

Figure A.1: On the left, a SEM image of the tip is provided, the apex size is around 20 nm. The tip shank is quite long, around 80 µm, in order to avoid the electrical interaction between the cantilever holder and the samples and the cantilever length is 300 µm. A schematic representation of the substrate and cantilever-tip system are shown on the right.

The first measurements have been conducted on a standard calibration sample from Infineon. The sample is made up of a lightly p-doped silicon substrate where several implanted strips of increasing doping level (both n- and p- type) can be used to evaluate the response of the SMM measurements with the respect to the doping level of the material.

The sample is divided in different regions, depending on the width of the implanted stripes, stripes of 2, 1 or 0.5 µm width are provided. The pitch between the stripes is always 2.5 µm, so that the entire region occupied by the 20 stripes can be scanned in 50x50 µm^2 area. Another region is present where crossed n and p stripes are present.

A scheme of the doped stripes is provided in figure A.2 to visualize the sample's characteristics

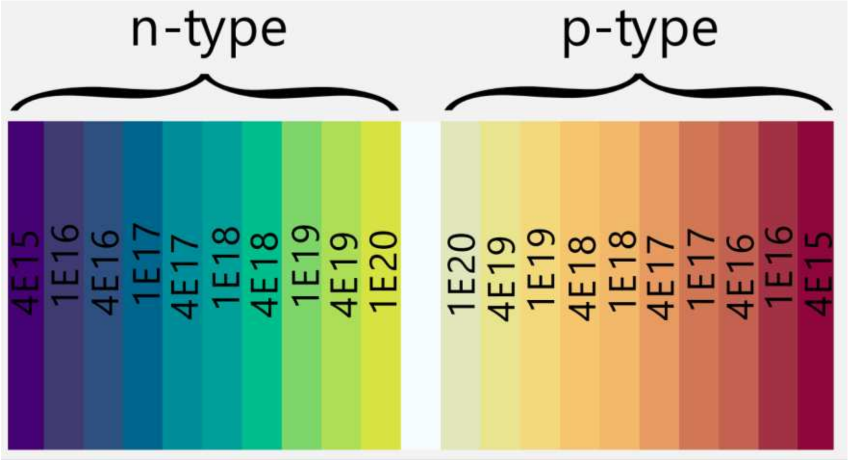

Figure A.2: scheme of the implanted regions on the calibration sample. The doping level for each stripe is also specified.

The first characterizations were performed on the region with 2 µm wide strips.

Images in both "Amplitude-Phase" and "Real-Imaginary components" were acquired for the S_{11} signal. It must be noted that the two images contain the same type of information. The "Amplitude-Phase" notation is more useful to visualize the variation of the signal in the vectorial space and to correlate the signal itself to the variation of the amplitude and phase of the microwave sent to the tip, caused by the interaction with the sample. Real and Imaginary images once calibrated are more useful to visualize the variations of electrical properties across the investigated area.

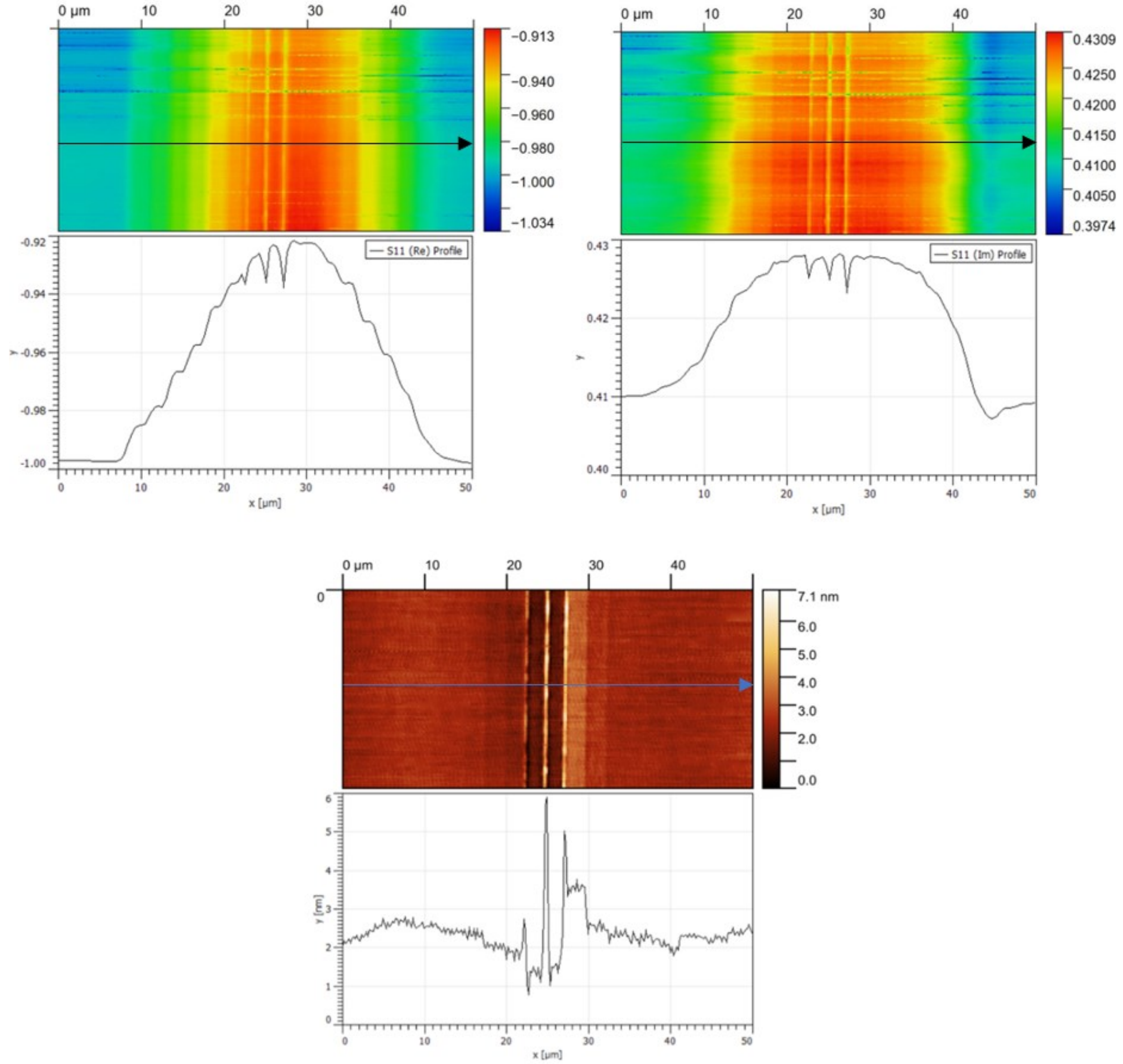

Figure A.3: SMM images of 2 µm wide strips, both the n and p-type region are scanned over a 50 µm wide region. The S_{11} real component image is reported on the left, while the imaginary component image is on the right. The topography image, reported below, is acquired during the SMM measurement. Line profiles are extracted and shown, below the images. The arrows in the images identify the profiled line.

The real and imaginary part of the S_{11} signal is reported in figure A.3. The images are acquired by scanning the sample in 50x5 µm^2 area, with 256 pixel per line in the x direction and 128 pixel per lines in the y direction, in order to optimize the scanning times. The doped stripes are visible thanks to the modulation of the reflected microwave. The real part of the S_{11} signal is related to the resistive component of the sample impedance, and the profile shows a monotonous modulation with respect to the doping. As the doping level increases the resistivity of the sample is reduced. In the centre of the image, where the stripes are highly doped, the three downward spikes that we see in the signal are produced by the topography of the sample.

Looking at the topography image we see three features in this region, probably an accumulation of natural oxide. The resistivity signal is affected by the oxide and the impedance of the sample is masked by the oxide.

The doped stripes seem to be visible also in the topographic image, towards the centre of the image. It's possible that the high doping in these regions, produced by a higher implantation dose, induce a modification on these regions that is observed in the surface morphology.

The same behaviour can be observed in the imaginary component image. The imaginary part of the signal is related to the capacitance of the sample. The depletion capacitance in the stripes is modulated by the doping level and the signal is monotonous with respect to the doping increase form stripe to stripe.

The dynamic range obtained for the two components of the S_{11} signal is hardly ever the same, both the characteristics of the system and the specific measurement parameters can enhance the sensitivity to resistivity or capacitance. The best range, and sensitivity, for the measurement needs to be identified by modifying several parameters, like contact force and electronics gains for the input and output port for the signal. Indeed, the instrument allows to modify two parameters, called RX1 and RX2, that allow to modify the gains on the reference signal and output one respectively. Finding the right gain combination is necessary to obtain good images.

For both the real and imaginary component we see a loss of sensitivity in the centre region, where the stripes are doped in the range between $1x10^{19}$ and $1x10^{20}$ cm^{-3}.

Some line-by-line variations in the electric response is always present in the measurements, these variations are produced by a slight modification in the environment between the tip and sample, for instance a variation of the relative humidity around the tip or the tip contact force on the sample.

A calibration curve has been obtained by focusing the scan on a smaller region of 50x1 μm^2 region. The nominal doping level of the stripes has been associated to each region of the sample, by making an educated guess on the position of the stripes. In figure A.4 the lines used to extract the average S_{11} signal for each stripe is shown. While the dynamic range for this new image is similar to the previous one, the signal this time lies in the positive numbers, this is produced by different gains used for the measurements. The best gain conditions are checked at the start of each measurement day.

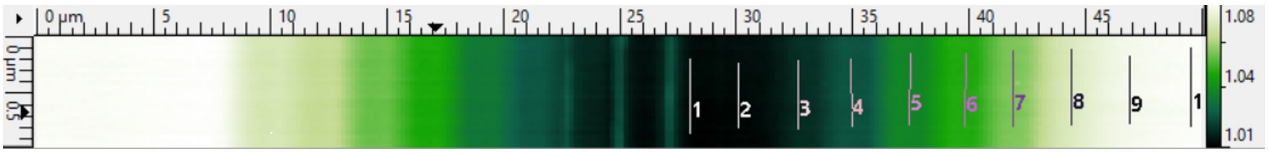

Figure A.4: Image of the real part of the S_{11} signal used to obtain a calibration curve. The right region has been used, in order to avoid the region on the left, where the presence of the higher oxide spikes mask the doping of the sample perceived by the instrument.

The calibration curve confirms what visually observed in the previous images. The S_{11} signal is log linear with respect to the doping of the sample, as also known from literature, in the medium doping range. The S_{11} signal is observed to be linear in the in the range of 10^{16}-10^{19} cm^{-3}. In the lower doing regime and in the higher doping one we see a flattening of the signal sensitivity.

While literature shows a linearity range between 10^{15} to 10^{20} cm^{-3}, the same results have not been obtained during this thesis period.

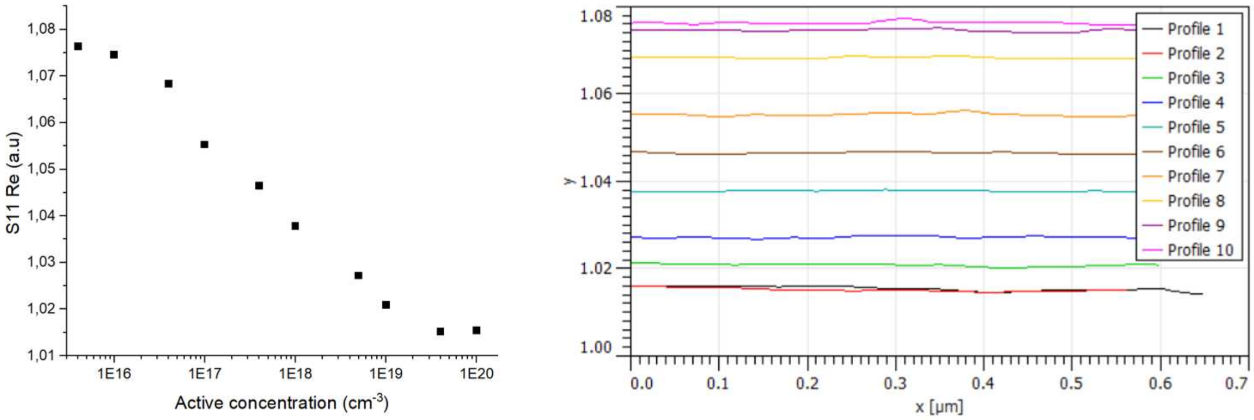

Figure A.5: On the left the calibration curve is showed, the real part of the S_{11} signal is plotted against the doping level in a log scale. On the right, the S_{11} values are showed along each line.

Moving on to the other regions of the calibration samples, the effect of the lateral stray fields can be evaluated.

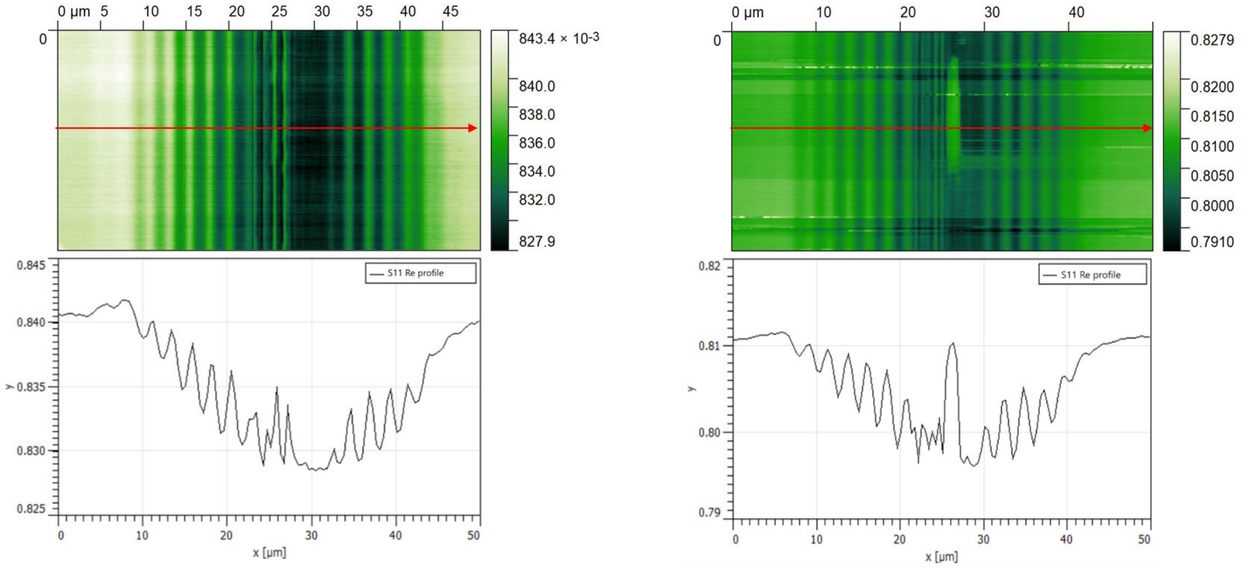

Figure A.7: Image of the real part of the S_{11} signal acquired the region with 1 µm wide stripes, on the left. On the right, the same image is acquired in the region with 0.5 µm wide stripes. Line profiles are extracted and shown, below the images. The arrows in the images identify the profiled line.

Images in the regions with 1 µm wide stripes and 0.5 µm wide stripes have been acquired, in order to identify the effect of the electrical interaction between the tip and the regions at the sides of the tip apex. As already introduced in chapter 3.3.5, the stray fields around the tip introduce another contribution to the tip-sample impedance. While most of the microwave radiation is effectively delivered on the sample by the tip apex, a certain amount of the signal is also irradiated by the sides of the tip, and the same happens after the microwave is reflected. The real shape of the tip is what ultimately determines the resolution of the final image, at the same time the stray field also influence the signal-to-noise ratio (SNR). In order to reach the best possible sensitivity and increase the doping range that can be investigated.

By looking at the images in fig. A.7 we see that by moving to narrower doped stripes, where the distance between them is larger we can see the separation between the doped region thanks to the wider undoped region that are able to decrease the electrical contribution form the doped regions at the sides of the tip.

In the images acquired for the 1 µm wide stripes the undoped region between two adjacent stripes is 1.5 µm wide and a better separation between the signals for the single doped stripes is indeed observed in comparison to the images acquired in the region with 2 µm doped stripes. The undoped silicon signal doesn’t reach the value of the undoped silicon at the extreme sides of the image, showing that the electrical contribution from the adjacent doped region is still present. The effect of the stray field on the right and left side of the tip is obviously not the same, as the regions on the two side have a different doping, and the reflection they produce is different. The effect is symmetrical for the left and right side of an image as it's expected considering that the doping decreases on the sides of the images and increases going towards the centre region.

In the image acquired for the 0.5 µm wide doped stripes the effect of the stray fields decreases again and the signal for the undoped region between the stripes is quite close to the signal observed at the extreme side of the image. Nonetheless, it must be noted that the separation between two doped regions in this case is 2 µm, and at even at this distance the interaction between the doped regions and the sides of the tip are still visible.

The use of a shielded tip might reduce this effect and improve both spatial electrical resolution and reduce the SNR.

Finally, a sample of Aluminium-doped Germanium, used for a previous study [20], was investigated. This sample served as a testing ground for the feasibility of the bevelling procedure for the analysis of the laser processed samples with the SMM technique.

The sample has been produced by Aluminium implantation on a lightly n-doped <100> Germanium wafer. A subsequent thermal anneal process at 400 °C has been performed to activate the dopant and reduce implantation damage, an active concentration of up to $1x10^{20}$ cm^{-3} has been calculated, thanks to a Spreading Resistance Profiling (SRP) characterization, performed by bevelling the sample at a low angle (0.34°).

The bevelling allows to extract a doping profile with respect to the implantation depth, by uncovering regions of the sample that correspond to different depth form the surface. While the sample is implanted in a projected range of ~25 nm, the bevelling allows for a line scan on the surface that can span tens of µm thanks to the relation: $d = x \cdot \tan(\alpha)$.

The following images have been acquired in Real-Imaginary mode by scanning an area of 40x2.5 µm and placing the tip on the unbevelled region, the bevel is met at the centre of the image and the decrease in height is observed in the topography image by following the bevelled region.

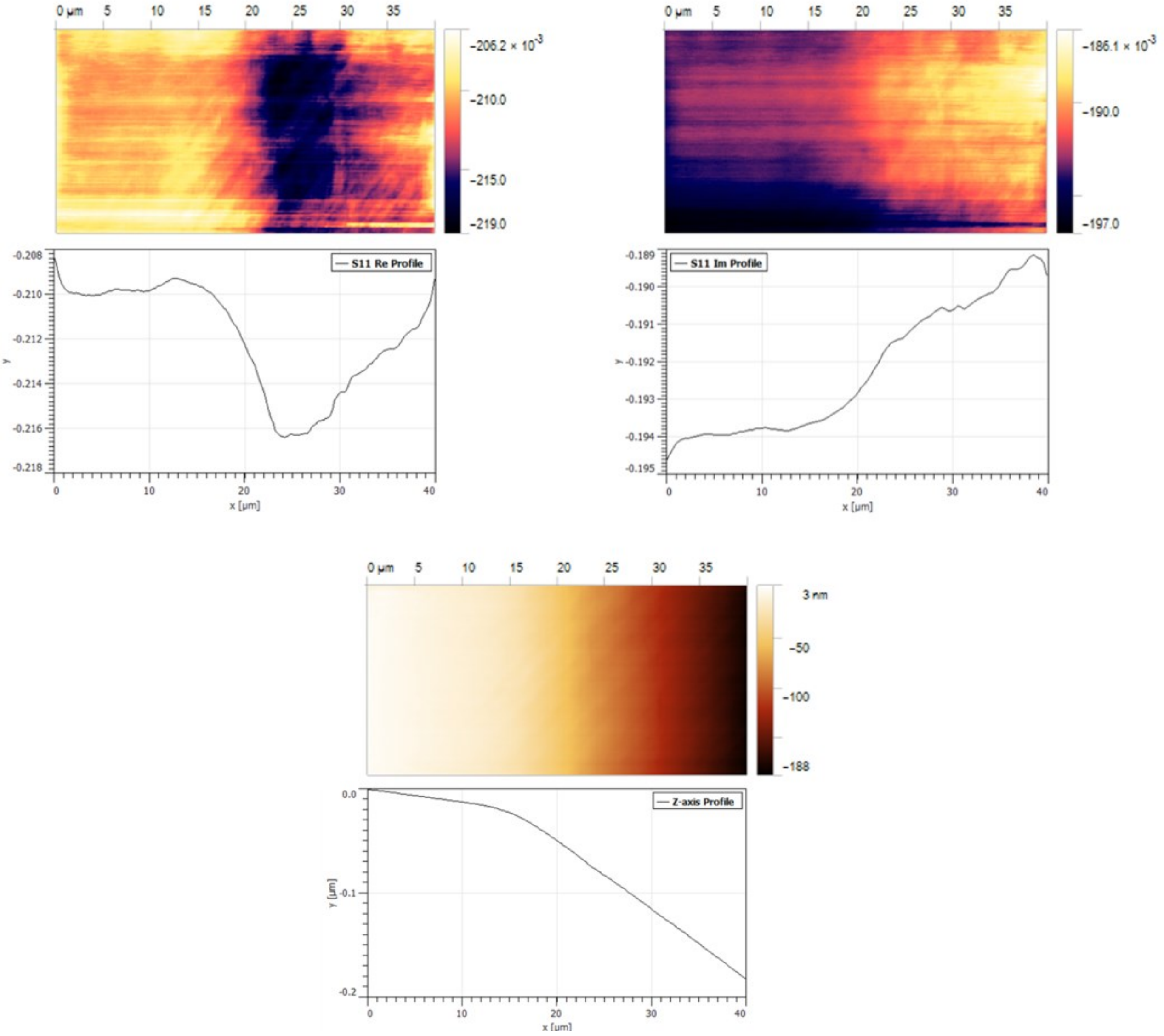

Figure A.8: SMM images of the bevelled sample in a 45x2.5 µm^2 area. The S_{11} real component image is reported on the left, while the imaginary component image is on the right. The topography image, reported below, is acquired during the SMM measurement. Line profiles are extracted and shown, below the respective image.

As shown in figure A.7, a modulation of the S_{11} signal is observed in both its real and imaginary components. The profiles are thus extracted, and thanks to the topography image, the profiles in length can be converted in depth profiles by identifying the starting position of the bevel.

The topography image is corrected, and a fit on the flat and bevelled region is done, in order to find their intersection, point that is considered the 0-depth point. A slight offset may be present, considering that the bevel angle in not completely sharp.

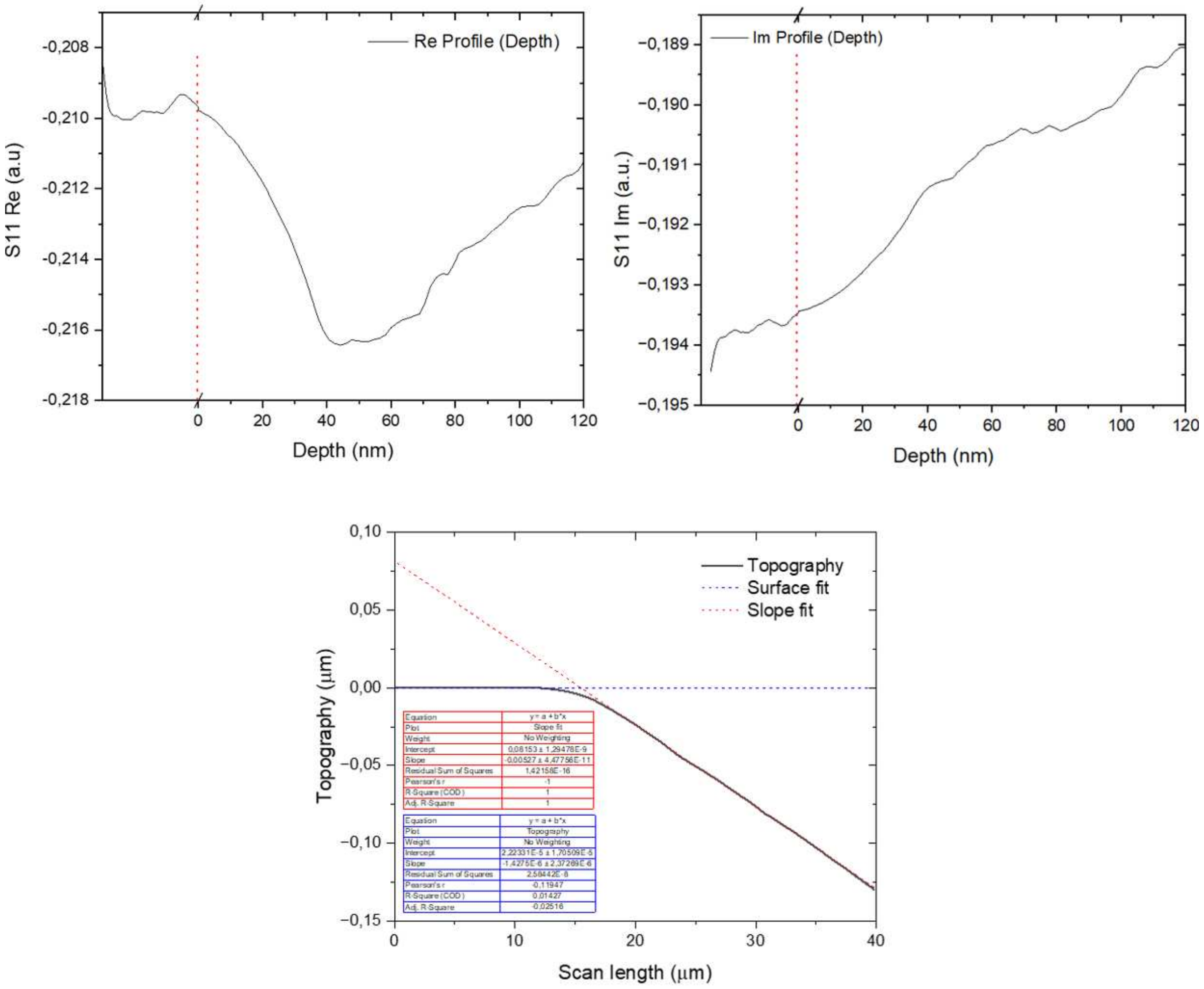

Equation	y = a + b*x
Plot	Slope fit
Weight	No Weighting
Intercept	0,08153 ± 1,29478E-9
Slope	-0,00527 ± 4,47758E-11
Residual Sum of Squares	1,42158E-16
Pearson's r	-1
R-Square (COD)	1
Adj. R-Square	1

Equation	y = a + b*x
Plot	Topography
Weight	No Weighting
Intercept	2,22331E-5 ± 1,70509E-5
Slope	-1,4275E-6 ± 2,37289E-6
Residual Sum of Squares	2,58442E-8
Pearson's r	-0,11947
R-Square (COD)	0,01427
Adj. R-Square	-0,02516

Figure A.9: Real and imaginary surface profiles converted in depth profiles, the data on the left of the red line are not converted to depth, as they belong to the unbevelled region. The conversion is done by identifying the start of the bevelled region thanks to two fits obtained for the surface and slope. The relation $d = x \cdot tan\ (\alpha)$ *is used.*

The Real part of the S_{11} signal shows a non-monotonous behaviour as shown in fig. A.9.

At the start of the bevel the signal is at it's highest, in this region the highly doped layer is just at the surface and the resistivity is at its lowest. Moving towards deeper regions we are observing less activated regions, and the resistivity increases.

At the 50 nm threshold the signal starts to increase again, suggesting a reduction of the resistivity, it's possible that the microwave is penetrating the sample, and the resistivity of the sample holder, a metal plate, is being probed. The penetration depth of the microwaves in a lightly doped sample can indeed reach the millimetre length and probe the sample holder. It must be noted that the sample also gets thinner as the tip moves towards the bevelled edge. A combination of the two might be responsible for the behaviour of the Real S_{11} signal.

A comparison with a spreading resistance measurement performed on the sample is provided in the next image.

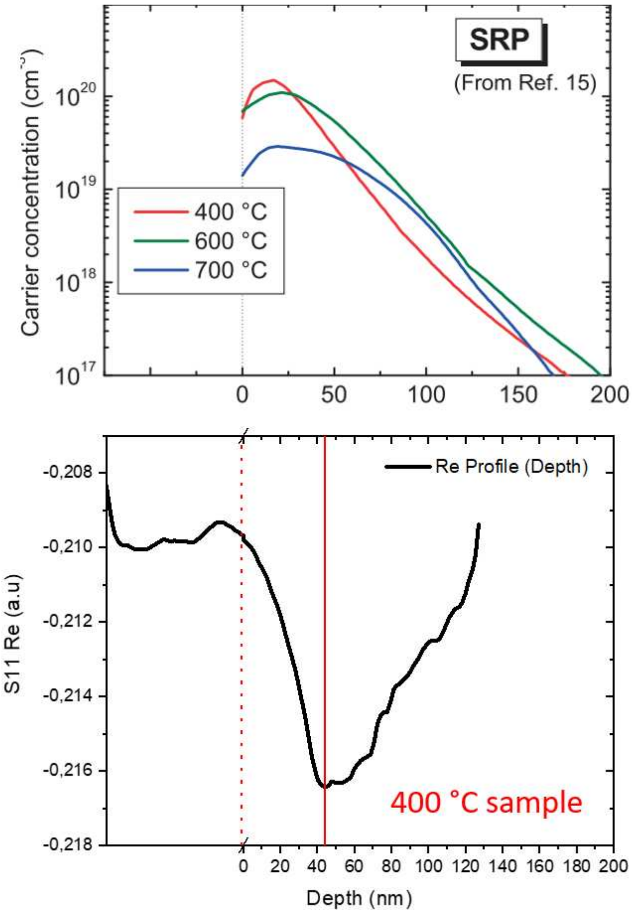

Figure A.10: Comparison between the doping profile extracted by the SRP performed by Sanson et al[73]and the Real S_{11} signal profile obtained by SMM. The SRP profile of interest is the 400°C one, which is the same sample investigated through SMM

The Spreading resistance profile shows a decrease of the doping level with respect to the bevel that is quite linear in a range between 50 and 200 nm in depth. The highest active region is seen at a 25 nm depth, coinciding with the implantation projected range. It is in this region that the thermal anneal produces the highest incorporation of dopant. In the same region we see decrease in the SMM signal, as already explained it’s possible that the effect of the metal plate masks the sample’s signal.

Looking at the Imaginary part of the S_{11} signal, we see a monotonous increase in the profile. This signal is correlated with the capacitance of the sample, the previous observation might also justify this behaviour. As the probed region of the metal plate increases and the thickness of the sample decreases, effectively shrinking the thickness of the capacitor, the detected capacity at the tip-sample interface increases.

The above characterization has shown a promising path for the obtainment of doping profiles thanks the sample bevelling. Placing a thicker dielectric layer under the sample might remove the effect of the metal stage allowing for a better measurement of the microwave reflection produced at the sample's surface.

The achievement of a sensitive and stable signal in the high doping regime is still difficult to obtain and more experiments must be performed in order to optimize the SMM measurements.